

AFFDL-TR-76-68

# **EFFECTS OF COMBINED ACOUSTIC AND FLIGHT LOADS ON CRACK GROWTH**

*LOCKHEED-CALIFORNIA COMPANY  
BURBANK, CALIFORNIA*

JULY 1976

TECHNICAL REPORT AFFDL-TR-76-68

Approved for public release; distribution unlimited

AIR FORCE FLIGHT DYNAMICS LABORATORY  
AIR FORCE WRIGHT AERONAUTICAL LABORATORIES  
AIR FORCE SYSTEMS COMMAND  
WRIGHT-PATTERSON AIR FORCE BASE, OHIO 45433

NOTICE

When Government drawings, specifications, or other data are used for any purpose other than in connection with a definitely related Government procurement operation, the United States Government thereby incurs no responsibility nor any obligation whatsoever; and the fact that the government may have formulated, furnished, or in any way supplied the said drawings, specifications, or other data, is not to be regarded by implication or otherwise as in any manner licensing the holder or any other person or corporation, or conveying any rights or permission to manufacture, use, or sell any patented invention that may in any way be related thereto.

This report has been reviewed by the Information Office (IO) and is releasable to the National Technical Information Service (NTIS). At NTIS, it will be available to the general public, including foreign nations.

This technical report has been reviewed and is approved for publication.

James L. Rudd

JAMES L. RUDD  
Project Engineer

R.M. Bader

ROBERT M. BADER, Chief  
Structural Integrity Branch  
Structural Mechanics Division

FOR THE COMMANDER

Howard L. Farmer

HOWARD L. FARMER, Colonel, USAF  
Chief, Structural Mechanics Division

Copies of this report should not be returned unless return is required by security considerations, contractual obligations, or notice on a specific document.

Unclassified

SECURITY CLASSIFICATION OF THIS PAGE (When Data Entered)

REPORT DOCUMENTATION PAGE		READ INSTRUCTIONS BEFORE COMPLETING FORM
1. REPORT NUMBER AFFDL-TR-76-68	2. GOVT ACCESSION NO.	3. RECIPIENT'S CATALOG NUMBER
4. TITLE (and Subtitle) EFFECTS OF COMBINED ACOUSTIC AND FLIGHT LOADS ON CRACK GROWTH		5. TYPE OF REPORT & PERIOD COVERED Final - June 75 to July 76
		6. PERFORMING ORG. REPORT NUMBER LR 27697
7. AUTHOR(s) J. SOOVERE S.T. CHIU		8. CONTRACT OR GRANT NUMBER(s) F33615-75-C-3087
9. PERFORMING ORGANIZATION NAME AND ADDRESS Lockheed-California Company Burbank, California 91520		10. PROGRAM ELEMENT, PROJECT, TASK AREA & WORK UNIT NUMBERS Project F145-75-574/486U Task 486U02 WU 486U0214
11. CONTROLLING OFFICE NAME AND ADDRESS Air Force Flight Dynamics Laboratory (FBE) Wright-Patterson Air Force Base, Ohio 45433		12. REPORT DATE July 1976
		13. NUMBER OF PAGES 142
14. MONITORING AGENCY NAME & ADDRESS(if different from Controlling Office)		15. SECURITY CLASS. (of this report) Unclassified
		15a. DECLASSIFICATION/DOWNGRADING SCHEDULE
16. DISTRIBUTION STATEMENT (of this Report) Approved for Public Release; Distribution Unlimited		
17. DISTRIBUTION STATEMENT (of the abstract entered in Block 20, if different from Report) Approved for Public Release; Distribution Unlimited		
18. SUPPLEMENTARY NOTES		
19. KEY WORDS (Continue on reverse side if necessary and identify by block number) Crack Growth; Combined Loads; Flight Loads; Simulated Acoustic Loads		
20. ABSTRACT (Continue on reverse side if necessary and identify by block number) A method for simulating the random acoustic excitation on a stiffened panel with an electromagnetic shaker is developed. The shaker simulation of the acoustic loading is verified both experimentally and theoretically over a wide range of axially applied tension and compression loads. Two flight-by-flight load spectra, corresponding to the upper and lower wing surface loads for typical Advanced Medium Transport Aircraft are developed and used in the test program. Real time takeoff and accelerated flight durations are used. The		

Unclassified

SECURITY CLASSIFICATION OF THIS PAGE(When Data Entered)

shaker simulated acoustic and axial flight-by-flight loads are applied both separately and simultaneously to a total of twelve stiffened panels. One flight load fastener hole precrack, normal to the axial flight loads, is used on all test panels and an additional acoustic type fastener hole crack, parallel to the rivet line, is used on two test panels. The measured crack growth data is compared with current analysis methods. Crack propagation paths, and magnified photographs and fractographs of the crack surfaces are presented. No significant effects on the crack growth rate are obtained by the simultaneous application of the acoustic and flight loads. The observed crack branching is, however, attributed to the acoustic loading.

SECURITY CLASSIFICATION OF THIS PAGE(When Data Entered)

## PREFACE

This report was prepared by the Lockheed-California Company, Burbank, California for the Structural Integrity Branch, Structures Division, Air Force Flight Dynamics Laboratory, Wright-Patterson Air Force Base, Ohio, under Contract F33615-75-C-3087. The work described herein is a continuing part of the Air Force Systems Command's exploratory development program to investigate all practical load combinations affecting crack growth, to meet the damage tolerance requirements for safety of flight aircraft structures. The work was directed under Project F1456-75-574/486U and task 486U02. Mr. D. Simpkins of the Structural Integrity Branch was the task engineer.

This report concludes the work on Contract F33615-75-C-3087, which covered a period from June, 1975 to July 1976.

The development of the flight-by-flight load spectra and the analysis of the flight load crack growth was performed by Dr. S.T. Chiu, the acoustic testing and data reduction by Mr. J. L. Hayward and the crack propagation testing and data reduction by Mr. C.J. Looper. Mr. J. Soovere was the project leader.

The manuscript was released by the authors for publication on 29th July 1976.

TABLE OF CONTENTS

<u>Section</u>	<u>Title</u>	<u>Page</u>
I	INTRODUCTION	1
II	DESIGN CONSIDERATIONS	3
	1. Introduction	3
	2. Panel Frequency	3
	2.1 Effect of Inplane Load	3
	2.2 Effect of Panel Edge Flexibility	6
	2.3 Effect of Added Panel Center Mass	7
	2.4 Panel Frequency Design Equation	7
	3. Panel Stress	7
	3.1 Panel Stress from Acoustic Excitation	9
	3.2 Effect of Added Mass on Panel Stress	11
	3.3 Combined Acoustic and Flight Load Panel Stresses	12
	3.4 Panel Stress Distribution	13
	4. Simulation of Acoustic Loading	14
	4.1 Acoustic Excitation	14
	4.2 Shaker Excitation	15
	4.3 Ratio of Shaker to Acoustic Force	15
	4.4 Shaker Damping	16
	4.5 Band Limited and Forced Excitation	16
	5. Detailed Design of Test Specimen	19
	5.1 Test Specimen Material and Thickness	19
	5.2 Selection of Panel Size	19
	5.3 Design Detail	21
	5.4 End Grip Design	25
	5.5 Fatigue Crack Initiation	25
III	LOAD HISTORIES AND SPECTRA	29
	1. Introduction	29

TABLE OF CONTENTS (Continued)

<u>Section</u>	<u>Title</u>	<u>Page</u>
	2. Flight-by-Flight Loads	29
	2.1 Basic Mission and Spectral Data	30
	2.2 Lower Wing Surface Load History	38
	2.3 Upper Wing Surface Load History	41
	3. Acoustic Loads	42
	4. Load Tapes	44
	4.1 Flight-by-Flight	44
	4.2 Acoustic	44
IV	CRACK GROWTH THEORY	47
	1. Introduction	47
	2. Flight-by-Flight Load Analysis	47
	2.1 Crack Growth Laws	47
	2.2 Crack Growth Retardation Models	48
	2.3 Stress Intensity Factor for Open Hole	51
	2.4 Crack Growth Calculation	52
	3. Acoustic Load Analysis	52
	3.1 Discussion of Analysis Method	56
	3.2 Simplified Analysis Procedure	57
	3.3 Crack Growth Calculation	57
V	TEST PROGRAM	59
	1. Introduction	59
	2. Calibration Tests	59
	2.1 Instrumentation	59
	2.2 Test Set-Up	61
	2.3 Test Procedure, Data Analysis and Results	61
	2.3.1 Progressive Wave Tunnel Calibration	61
	2.3.2 Panel Damping and Frequency	63
	2.3.3 Panel Response to Shaker Excitation	63
	2.3.4 Panel Response to Acoustic Excitation	67
	2.4 Calibration of Shaker and Acoustic Excitation	74
	2.5 Discussion of the Test Results	74
	2.5.1 Progressive Wave Tunnel Calibration	74
	2.5.2 Panel Damping and Frequency	74

TABLE OF CONTENTS (Continued)

<u>Section</u>	<u>Title</u>	<u>Page</u>
	2.5.3 Shaker and Acoustically Excited Panel Response	78
	2.5.4 Calibration Curve	80
	3. Combined Loads Tests	80
	3.1 Instrumentation	81
	3.2 Test Set-Up	85
	3.3 Test Procedure	88
	3.3.1 Baseline Tests	88
	3.3.2 Flight-by-Flight Loads and Combined Loads	89
	3.3.3 Shaker Loading	90
	3.4 Data Analysis	90
	3.5 Test Results	91
	3.5.1 Baseline Tests	91
	3.5.2 Flight-by-Flight and Combined Loads	91
	3.5.3 Simulated Acoustic Loads	105
	3.6 Discussion of Test Results	118
	3.6.1 Baseline Tests	118
	3.6.2 Flight-by-Flight and Combined Loads	121
	3.6.3 Simulated Acoustic Loads	130
VI	CORRELATION AND EVALUATION	132
	1. Introduction	132
	2. Panel Response	132
	3. Crack Growth Prediction	133
VII	CONCLUSIONS	139
	REFERENCES	140

LIST OF ILLUSTRATIONS

<u>Figure</u>	<u>Title</u>	<u>Page</u>
1	Panel Coordinates	5
2	Frequency Correction Factor for Higher Order Axial Panel Modes	8
3	Normalized Single Degree of Freedom Frequency Response Function	17
4	Effect of Band Limited Random Excitation on the Mean Square Response of a Single-Degree-of-Freedom System	18
5	Test Panel Details	20
6	Iterative Panel Design Procedure	22
7	Effect of Axial Inplane Stress on Panel Frequency	23
8	Effect of Aspect Ratio on Frequency of Panel Subjected to Compression Stress of 7500 PSI	24
9	Force Gage	26
10	Panel End Grip Assembly	27
11	Precrack for Combined Loads	28
12	Precrack for Shaker Simulated Acoustic Loading	28
13	PABST Aircraft Utilization (Simplified)	32
14	Truncation of Load Spectra	39
15	Typical Section of Upper Wing Load Time History	45
16	Typical Section of Lower Wing Load Time History	46
17	Calibration Panel Strain Gage Locations	60
18	Shaker and Specimen Mounting on Progressive Wave Tunnel	62
19	Shaker/Panel Driving Rod and Force Gage Detail	62
20	Typical Tunnel Sound Pressure Levels from 1/3 Octave Measurements	64

LIST OF ILLUSTRATIONS (Continued)

<u>Figure</u>	<u>Title</u>	<u>Page</u>
21	Panel Free Decay with Shaker Power On	65
22	Panel Free Decay with Shaker Power Off	65
23	Panel Edge Strain as a Function of Shaker Force	66
24	Typical Narrow Band Analysis of Shaker Force	68
25	Typical Narrow Band Analysis of Shaker Excited Panel Edge Strain	69
26	Probability Density Distribution of Strain Peaks and Valleys for Strain Gages A1 and A2, Shaker Excitation	70
27	Panel Edge Strain as a Function of Reference OASPL and Noise Bandwidth	71
28	Force Gage Output as a Function of Reference OASPL and Noise Bandwidth	71
29	Narrow Band Analysis of Acoustic Excitation	72
30	Typical Narrow Band Analysis of Acoustically Excited Panel Strain, Strain Gage A1	73
31	Probability Density Distribution of Strain Peaks and Valleys for Strain Gages A1 and A2, Acoustic Excitation	75
32	Panel Strain Distribution Relative to Crack Growth Area	76
33	Calibration Curves for Shaker Force and Noise Excitation	77
34	Reduced Bandwidth Analysis of Acoustically Excited Panel Edge Strain	79
35	Baseline Test Panel CF3 Strain Gage Locations	83
36	Combined Loads and Acoustic Loads Panel Strain Gage Locations	84
37	Test Set-up for Baseline and Flight Load Tests	86
38	Test Set-up for Combined Acoustic and Flight Load Tests	86

LIST OF ILLUSTRATIONS (Continued)

<u>Figure</u>	<u>Title</u>	<u>Page</u>
39	Close-up of Test Specimen and Shaker Drive Arrangement	87
40	Typical Arrangement for Measuring Crack Growth	87
41	Baseline Test Specimen Compression Load Strain Curves	92
42	Typical Load History During Cycling	93
43	Typical Strain Load Plot During Cycling	94
44	Variation of Peak Axial Compression and Tensile Strain with Crack Growth Length, Panel CF3	95
45	Crack Propagation in Test Specimen CF3	96
46	Baseline Crack Growth Data, Test Specimen CF3	97
47	Variation in Panel Peak Stress Between Test Specimens During Pretest Cycling	98
48	Panel Fundamental Frequency as a Function of Axial Inplane Load	99
49	Panel Damping Coefficient as a Function of Axial Inplane Load	100
50	Panel Edge RMS Strain Due to Shaker Excitation as a Function of Axial Inplane Load	101
51	Typical Strain History Without Acoustic Loading; Strain Gage F1, Test Specimen CF7	102
52	Typical Strain History with Acoustic Loading; Strain Gage F1, Test Specimen CF9-2	103
53	Typical Strain History with Acoustic Loading; Strain Gage F3, Test Specimen CF9-2	104
54	Narrow Band Spectral Analysis of Strain Gage F1, Test Specimen CF5	106
55	Narrow Band Spectral Analysis of Strain Gage F3, Test Specimen CF5	107
56	Narrow Band Spectral Analysis of Strain Gage F1, Test Specimen CF6	108

LIST OF ILLUSTRATIONS (Continued)

<u>Figure</u>	<u>Title</u>	<u>Page</u>
57	Typical Crack from Upper Wing Surface Flight Loads, Test Specimen CF7	110
58	Typical Crack from Combined Upper Wing Surface Flight Loads and Simulated Acoustic Loads, Test Specimen CF11	110
59	Typical Crack from Combined Lower Wing Surface Flight Loads and Simulated Acoustic Loads, Test Specimen CF12	111
60	Typical Crack from Combined Upper Wing Spectral, Tension and Simulated Acoustic Loads, Test Specimen CF5	111
61	Typical Crack from Combined Lower Wing Spectral, Tension and Simulated Acoustic Loads, Test Specimen CF6	112
62	Crack from Shaker Drive Rod Hole, Test Specimen CF11	112
63	Measured Crack Growth Rate Data, Test Specimen CF5	113
64	Measured Crack Growth Rate Data, Upper Wing Surface Loads	114
65	Measured Crack Growth Rate Data, Test Specimen CF6	115
66	Measured Crack Growth Rate Data, Lower Wing Surface Loads	116
67	Frame Cracks Adjacent to Panel Precracks	117
68	Acoustic Panel Edge Crack, Test Specimen CF2	119
69	Panel Center Crack, Test Specimen CF2	119
70	Measured Crack Growth Rate, Simulated Acoustic Excitation	120
71	Crack Surface and Fractographic Detail, Test Specimen CF7	124
72	Crack Surface and Fractographic Detail, Test Specimen CF9-2	125
73	Crack Surface and Fractographic Detail, Test Specimen CF5	127
74	Crack Surface and Fractographic Detail, Test Specimen CF12	128

LIST OF ILLUSTRATIONS (Continued)

<u>Figure</u>	<u>Title</u>	<u>Page</u>
75	Comparison of Measured and Calculated Crack Growth, Test Specimen CF5	134
76	Comparison of Measured and Calculated Crack Growth, Upper Wing Surface Loads	135
77	Comparison of Measured and Calculated Crack Growth, Test Specimen CF6	136
78	Comparison of Measured and Calculated Crack Growth, Lower Wing Surface Loads	137

LIST OF TABLES

<u>Table</u>	<u>Title</u>	<u>Page</u>
1	PABST Aircraft Utilization (Modified Spectrum)	31
2	Taxi, Takeoff, and Landing Roll Spectrum (Prepared and Semi-prepared Runways)	33
3(a)	Maneuver Load Spectra for Transport Aircraft	34
3(b)	Turbulence Parameter	35
4	Low Level Re-supply Mission Gust Plus Maneuver Load Spectrum	36
5	Landing Impact Incremental Load Spectrum	37
6	The Truncated Low Level Re-supply Mission Spectrum for 18 Missions	40
7	The Truncated Typical Mission Spectrum for 56 Missions	40
8	The Truncated Taxi, Takeoff, and Landing Spectrum for 72 Missions	42
9	Stress Levels for the Lower Wing Surface Spectrum	53
10	Stress Levels for the Upper Wing Surface Spectrum	54
11	Lower Wing Test Load and Panel Stress Data	55
12	Upper Wing Test Load and Panel Stress Data	55
13	Phase 2 Test Program Matrix	82
14	Summary of Flight-by-flight and Combined Loads Crack Propagation Data	109

LIST OF SYMBOLS

A	area
a	panel length; flight load crack length; half acoustic crack length
B	ratio of acoustic crack length to panel length
b	panel width measured between rivet lines
$b_1, b_2$	maneuver load spectrum constants
$C, C_w$	crack growth material constants
$C_p$	retardation parameter, equation 46
c	speed of sound in air
D	flexural rigidity of a panel
E	Young's modulus of elasticity
F	force spectrum
$F_o( )$	defined by equation 65
f	frequency
$f_r, f_s$	resonant frequency of flexibly and simply supported panels respectively
$f( )$	function
G	generalized acoustic spectrum
GF	generalized white noise load spectrum
$G_0, G_{01}, G_{02}$	constant acoustic spectrum levels
g	incremental load factor
$g( )$	threshold stress intensity function
H	normalized single degree-of-freedom response spectrum
h	panel thickness

K	modal frequency constant; stress intensity factor
$K_c$	fracture toughness
L	turbulence length; crack growth lifetime in number of periods
M	panel center mass
$M_r$	generalized panel mass
m	axial mode number; material crack growth constant
N	number of cycles
$N_{ol}, N_{o2}$	maneuver load spectrum constants
$N_x$	axial inplane load per unit width
n	lateral mode number; material crack growth constant
$P_1, P_2$	turbulence parameters
q	inertia load per unit area
R	stress range ratio
r	radial distance; radius of fastener hole
$r_{ep}$	distance from crack tip to the elastic-plastic interface
$r_p$	radius of the plastic zone
S	material related crack growth parameter
t	time
W	panel deflection
w	mode shape
x	axial coordinate axis
y	lateral coordinate axis
Z	complex impedance
z	vertical coordinate axis

$\beta$	material crack growth constant
$\Delta$	increment
$\delta$	viscous damping coefficient
$\epsilon_x, \epsilon_y$	axial and lateral strains respectively
$\epsilon_{xe}, \epsilon_{ye}$	maximum axial and lateral panel edge bending strains respectively
$\epsilon_{xF}$	instantaneous axial flight load produced strain
$\eta$	geometric crack parameter, equation 64
$\nu$	Poisson's ratio
$\xi(t)$	time dependant generalized coordinate
$\bar{\xi}$	generalized coordinate
$\xi_1, \xi_2$	axial and lateral separation distances respectively
$\rho$	mass density
$\sigma_{red}$	stress reduction
$\sigma_x, \sigma_y$	axial and lateral stresses respectively
$\sigma_{xAF}, \sigma_{yAF}$	axial and lateral combined acoustic and flight load instantaneous stresses respectively
$\sigma_{xF}$	axial instantaneous flight load stress
$\sigma_{yA}$	lateral instantaneous acoustic load stress
$\sigma_{xe}, \sigma_{ye}$	maximum axial and lateral panel edge bending stresses respectively
$\sigma_{yeM}$	maximum lateral panel edge bending stress for mass attached panel
$\sigma_{ys}$	tensile yield stress
$\omega$	circular frequency
$\omega_r$	flexibly supported panel circular resonant frequency

### Notation

- over-bar denotes the root mean square value or constants associated with the root mean square stress except in the above list of symbols
- |<sub>x= ,y=</sub> evaluated at given constants of x and y or any other variable so defined

### Subscripts

- A denotes acoustic
- eff denotes effective
- j denotes cycle number
- M denotes mass attached
- max denotes maximum value of
- min denotes minimum value of
- OL denotes overload
- S denotes shaker

## I. INTRODUCTION

Crack propagation studies are employed in the aircraft industry to formulate inspection and maintenance schedules for "in-service" monitoring to meet the damage tolerance requirements (Reference 1) for safety of flight structures. Interest is, therefore, centered on all practical loading combinations, such as the combination of flight-by-flight loads with acoustic loads, which are not accounted for in current crack propagation analysis and which may have a significant effect on the crack growth behavior. The potential effect of the combined loading has assumed a greater significance with the advent of the Advanced Medium Transport Aircraft. In these aircraft, due to the close proximity of the jet engine exhaust to the aircraft structure, a significant level of acoustic excitation of a long duration will be encountered during flight in addition to the high level take-off and landing noise levels which normally impose the sonic fatigue design requirement for critical structures.

Crack propagation in aircraft structures due to either flight loads or acoustic loads has been studied extensively, but independently, over the past two decades. The separated development is due in part to the analysis methods which lean heavily on their respective fatigue analysis procedures. The flight loads can introduce significant stress levels in both heavy and light load carrying structures whereas significant stress levels can only be produced in relatively light panel type structures by acoustic loading. The loading action is also different for the acoustic and the flight loads. The flight loads introduce predominantly inplane tension and compression stresses whereas the acoustic loading introduces predominantly bending stresses, in the local structure.

In the study of crack propagation due to flight loads, the representation of the flight loads has progressed from constant amplitude loading (Reference 2) to the more complex flight-by-flight loading (References 3 to 6). To improve the accuracy of the latter analyses, methods (References 7, 8 and 9) which include the effects of crack retardation due to infrequent high loads have been developed. The test specimen configurations have progressed from the simple center crack specimen to the more complex structural joint specimen with precracks in the fastener holes (References 10 and 11).

The study of crack propagation due to acoustic loading was initiated (Reference 12) in connection with turbulent boundary layer excitation of the fuselage panels in a supersonic transport aircraft at high dynamic pressures. The turbulent boundary layer was simulated by acoustic loading, with the constant fuselage pressurization stresses represented by simultaneously applied uniaxial (References 12 and 13) and later (Reference 14) by biaxially inplane loads. Again, test panels with a center crack normal to the principal acoustic and inplane hoop loading were employed.

Subsequent studies employing the more realistic panel edge cracks, indicated that significant crack growth can be obtained due to peak acoustic loading during takeoff in sequence with the ground-air-ground cycle (Reference 15) and indeed from the takeoff acoustics alone (Reference 16). The basic analysis procedure (Reference 16) is based on random response theory employing the Rayleigh distribution of stress peaks associated with a predominant single mode response. The test data indicates that loading frequency and crack closure affect the crack growth rate.

When flight loads and acoustic loads are applied simultaneously, interaction effects can occur which may affect the crack growth rate. This program represents a preliminary investigation into the study on the effect of combined acoustic and flight loads on crack growth.

The objectives of this program are to determine

- o if combined acoustic and flight loads have a significant effect on crack growth
- o whether any significant effects can be predicted by current crack propagation analysis methods

As no test facilities are available in which flight and acoustic loads can be simultaneously applied, electromagnetic shaker simulation of acoustic loading is employed in this program. Other requirements imposed on this program are the need for real time simulation of the duration of the acoustic excitation as far as practical and the application of significant compression loads and tension flight loads on the test specimen. Airplane skin bay type structures, which are subjected to significant compression loads, are generally loaded axially with the smallest panel dimension normal to the applied load to obtain maximum resistance to panel buckling. With the simultaneous application of acoustic and axial flight loading, a predominantly biaxial stress field is obtained at the center of the skin bay and at the center of the longest panel side. At these locations, the axial flight load stresses are normal to the predominant acoustic load stresses. A greater variability and higher stress levels are usually encountered with the flight-by-flight loading in comparison to the acoustic loading. Consequently, the programmed crack orientation used in the combined loads tests in this program, is selected on the premise that the flight loading is the more critical loading condition and, therefore, more likely to initiate the crack.

This report on the research program contains the specimen design considerations including panel response theory and the impact of electromagnetic shaker simulation of the acoustic loading on the panel design in Section II; the development of the loading time history based on truncated runway and gust spectra in Section III; a summary of current crack propagation prediction methods and crack growth calculations in Section IV; the test program in Section V; the correlation and evaluation of the test and analytical results in Section VI; and, finally, the conclusions in Section VII.

## II DESIGN CONSIDERATIONS

### 1. Introduction

The purpose of the program is to study crack growth behaviors in simulated aircraft structures due to combined acoustic and flight loads. The design of the test specimen must, therefore, be such that significant stresses can be achieved in the region of the programmed crack by both loading actions. The test specimen must, in addition, withstand compression loads without buckling.

These requirements can be satisfied by a single panel test specimen supported by stiffeners on both sides. Since an electromagnetic shaker is used to simulate the acoustic excitation, the shaker coil and the drive rod weight will significantly affect the panel response frequency and stresses and, consequently, the panel dimensions. The panel dimensions are equally affected by the compression loads. A theoretical study of the panel response is, therefore, necessary to define the dimensions of the test panel.

### 2. Panel Frequency

The dynamic response of stiffened panel type aircraft structures represents a complex analytical problem due to the flexibility of the panel edges. The fundamental frequency of the stiffened panels falls halfway between the fixed-fixed and the simply supported panel frequencies, tending towards the corresponding simply supported frequency for progressively higher panel modes. When typical stiffened aircraft panels are excited by jet noise, predominant single mode response is observed (References 17 and 18). In acoustic progressive wave tunnels, used to simulate jet noise excitation, the second axial panel mode can also be excited if the panel longest side is parallel to the tunnel axis. In general, the use of only the fundamental mode in panel response studies of random acoustic excitation is adequate.

The expression for the simply supported panel fundamental frequency, when modified by an empirical factor to account for the edge flexibility (Reference 19), can be used to predict the stiffened panel fundamental frequency. The advantages are its simplicity and accuracy. This method will now be extended to include the effects of an axial inplane load and the addition of a panel center mass, representing the weight of the shaker coil and drive rod, on the panel fundamental frequency. For maximum compression load carrying capability, the smallest panel dimension must be normal to the direction of the applied compression load.

#### 2.1 Effect of Inplane Load

The differential equation for the deflection,  $W$ , of a flat plate subject to axial inplane load,  $N_x$ , per unit width is given by (References 20 and 21, pp. 276)

$$\frac{\partial^4 W}{\partial x^4} + 2 \frac{\partial^4 W}{\partial x^2 \partial y^2} + \frac{\partial^4 W}{\partial y^4} = \frac{1}{D} \left( q + N_x \frac{\partial^2 W}{\partial x^2} \right) \quad 1$$

where

$$D = \frac{E h^3}{12(1-\nu^2)}$$

is the flexural rigidity of the panel,  $q$  is the external transverse surface force per unit area,  $h$  is the panel thickness,  $E$  is the Young's modulus and  $\nu$  is the Poisson's ratio. For dynamic response,  $q$  is replaced by the inertia force given by

$$q = -\rho h \frac{\partial^2 W}{\partial t^2} \quad 2$$

where  $\rho$  is the panel density. The panel coordinates are defined in Figure 1. The deflection in any one mode of a simply supported panel is

$$W = w(x,y) \cdot \xi(t) \quad 3$$

where

$$w(x,y) = \sin \left( \frac{m\pi x}{a} \right) \cdot \sin \left( \frac{n\pi y}{b} \right) \quad 4$$

is the simply supported panel mode shape,  $m$  and  $n$  are the axial and lateral mode number,  $a$  is the panel length, and  $b$  is the panel width. For simple harmonic motion,  $\xi(t)$ , is given in terms of the generalized coordinate,  $\bar{\xi}$ , by

$$\xi(t) = \bar{\xi} \sin \omega t \quad 5$$

Substitute equations 2 to 5 into equation 1. After the necessary algebraic manipulation, the following expression is obtained for the panel frequency

$$f = \frac{\pi}{2} \left( \frac{D}{\rho h} \right)^{1/2} \left\{ \left[ \left( \frac{m}{a} \right)^2 + \left( \frac{n}{b} \right)^2 \right]^2 + \frac{N_x}{\pi^2 D} \left( \frac{m}{a} \right)^2 \right\}^{1/2} \quad 6$$

With zero inplane load, equation 6 reduces to the expression for the frequency of a simply supported panel given by

$$f_s = \frac{\pi}{2} \left( \frac{D}{\rho h} \right)^{1/2} \left[ \left( \frac{m}{a} \right)^2 + \left( \frac{n}{b} \right)^2 \right]^{1/2} \quad 7$$

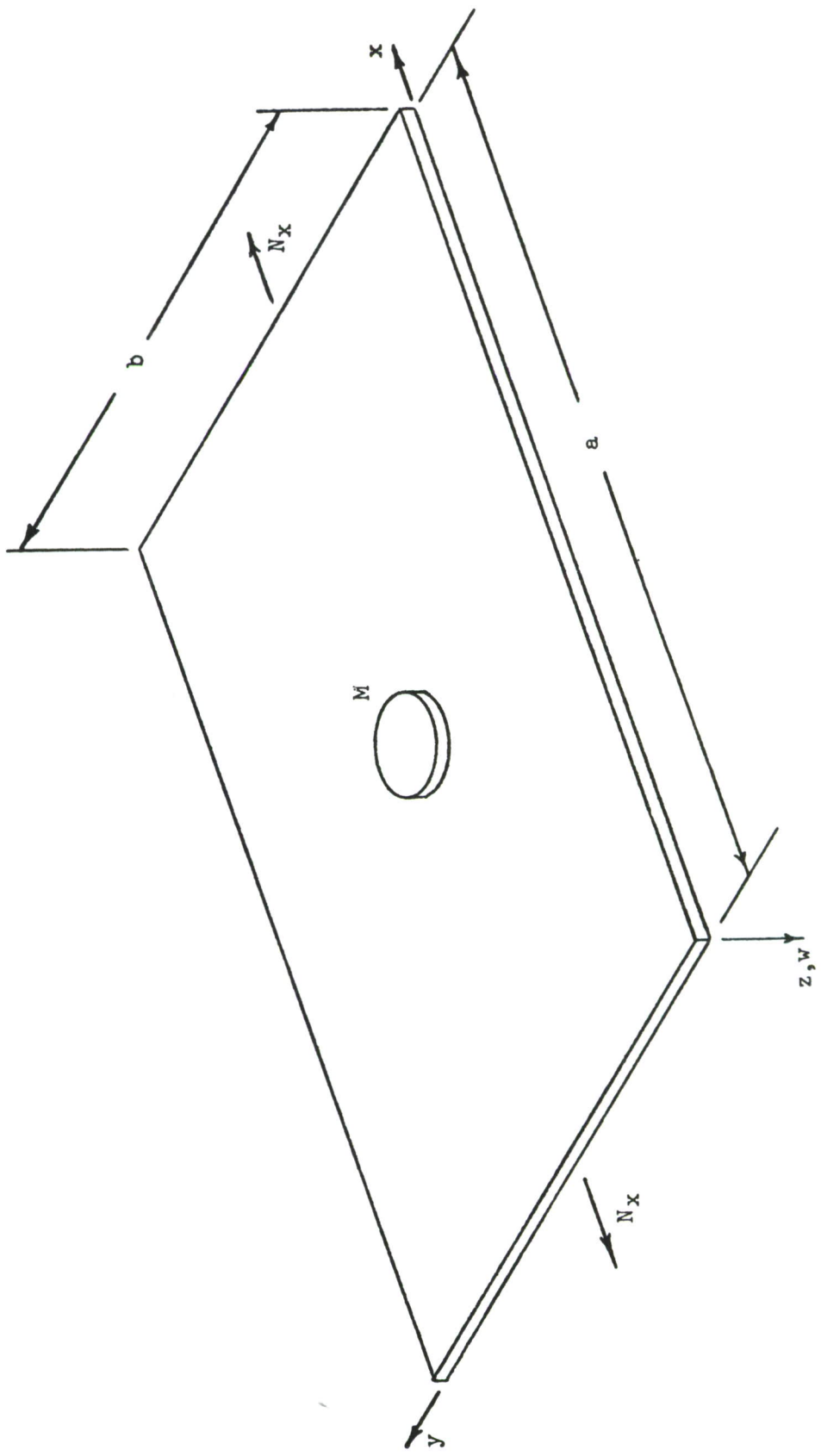


FIGURE 1. PANEL COORDINATES

Substituting equation 7 back into equation 6 results in

$$f = \left[ f_s^2 + \frac{N_x}{4\rho h} \left( \frac{m}{a} \right)^2 \right]^{1/2} \quad 8$$

The critical panel compressive stress,  $\sigma_{xc}$ , is obtained when the panel frequency becomes zero. Then

$$\sigma_{xc} = -4\rho f_s^2 \left( \frac{a}{m} \right)^2 \quad 9$$

which is the relationship between the unloaded panel frequency and the critical axial buckling stress.

## 2.2 Effect of Panel Edge Flexibility

The effect of edge flexibility on panel frequency is accounted for by the introduction of an empirical constant K (Reference 19) into equation 7 as illustrated below

$$f_r = \frac{\pi K}{2} \left( \frac{D}{\rho h} \right)^{1/2} \left[ \left( \frac{m}{a} \right)^2 + \left( \frac{n}{b} \right)^2 \right] \quad 10$$

For the fundamental panel mode K is approximately equal to 1.48. On replacing the simply supported panel frequency in equation 8 with the stiffened panel frequency, equation 10, and on rearranging the terms, the expression for the stiffened panel frequency with inplane load is obtained and given by

$$f = f_r \left\{ 1 + \frac{\sigma_x h a^2}{\pi^2 m^2 K^2 D \left[ 1 + \left( \frac{a n}{b m} \right)^2 \right]^2} \right\}^{1/2} \quad 11$$

The critical buckling stress is a function of panel aspect ratio. The lowest critical buckling stress may occur with an axial panel mode higher than the fundamental. Only limited data (Reference 19) is available on the higher order modal frequencies for typical aircraft panels. This data is insufficient for constructing a frequency correction curve for the higher order axial panel modes. The frequency correction factor, for the higher order axial panel modes, can, however, be obtained from the theory in Reference 21, page 117, which predicts the effect of panel edge rotational restraint on panel frequency. The two longer panel edges are rotationally restrained whereas the two shorter edges are simply supported. A representative rotational edge stiffness parameter can be extracted from the theory by requiring the ratio of the stiffened panel frequency to the simply supported panel frequency to equal 1.48 at a panel aspect ratio of two. There-

after, the remainder of the frequency correction curve is readily obtained from the theory and is illustrated in Figure 2 as a function of effective aspect ratio defined by  $(a/b)$ . Limited test data is included in Figure 2 for comparison.

### 2.3 Effect of Added Panel Center Mass

The effect of an added panel center mass  $M$  on the panel frequency can be computed considering the generalized mass of the panel and the added weight. The generalized mass  $M_r$  for the panel is given by

$$M_r = \rho h \int_0^a \int_0^b w(x,y) dx dy \quad 12$$

The generalized mass of the added mass is equal to  $M$  for a simply supported mode shape as the modal displacement is unity at the center of the panel. The corresponding panel generalized mass is equal to  $0.25 \rho abh$ . The ratio of the generalized mass of the panel to the generalized mass of the added mass and the panel is

$$\frac{\rho abh}{\rho abh + 4M}$$

The relationship between the simply supported panel frequency with (Reference 21, pp. 147) and without the attached mass follows directly and is given by

$$f_M = f_s \left( \frac{\rho abh}{\rho abh + 4M} \right)^{1/2} \quad 13$$

### 2.4 Panel Frequency Design Equation

The addition of the center mass will not affect the critical buckling stress which is still related to the stiffened panel frequency without the attached mass. The final expression for the stiffened panel frequency with both the axial inplane load and the attached mass is given by

$$f_d = f_r \left\{ \frac{\rho abh}{\rho abh + 4M} \right\}^{1/2} \left\{ 1 + \frac{\sigma_x ha^2}{\pi^2 m^2 K^2 D \left[ 1 + \left( \frac{an}{bm} \right)^2 \right]^2} \right\}^{1/2} \quad 14$$

where  $f_r$  is given by equation 10.

### 3. Panel Stress

In typical stiffened aircraft panels which are subjected to acoustic loading, the greatest panel bending stresses occur in the fundamental mode in a

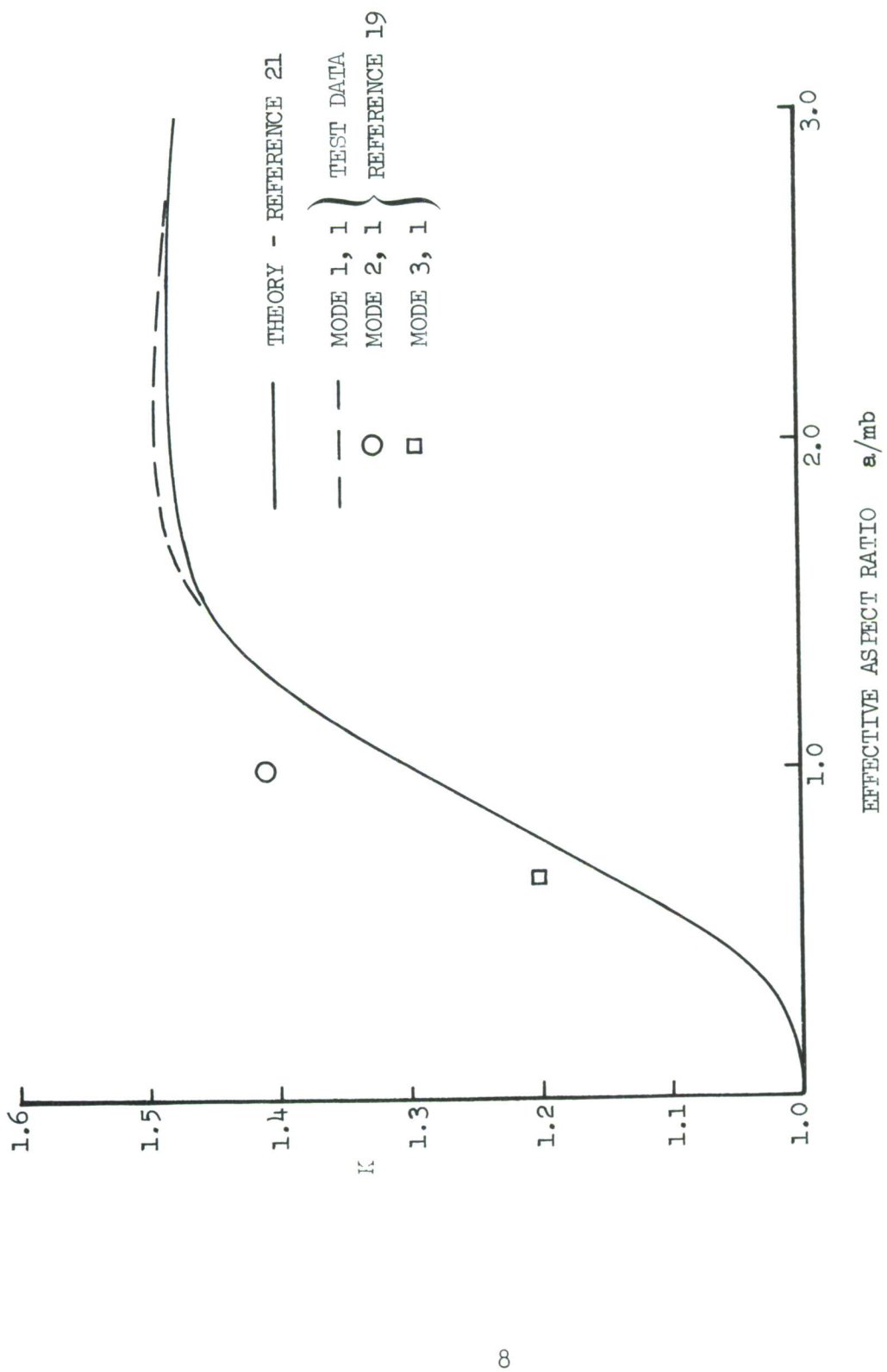


FIGURE 2. FREQUENCY CORRECTION FACTOR FOR HIGHER ORDER AXIAL PANEL MODES

direction normal to the panel edge both at the center of the longest panel edge and at the center of the panel. The resulting lateral panel stress distribution is generally symmetrical about the panel centerline. After peaking at the panel edge, the stress distribution falls off to zero somewhere between the panel edge and center and, thereafter, to a negative peak at the panel center. The magnitude of the panel edge and center stresses are comparable for the level of edge flexibility encountered in stiffened aircraft panel structures. The panel edge is, however, more critical for fatigue crack initiation because of the stress concentration effect of the frame edge and the fastener holes. Sonic fatigue and flight load cracks usually emanate from fastener holes in this region which has been chosen as the location for the programmed cracks in this study. Consequently, attention will be focused on panel stresses in the panel edge region.

Accurate prediction of panel edge stresses in these stiffened panels due to acoustic loading is difficult as the magnitude and distribution of stresses are affected by such parameters as the stiffener geometry, the stiffener width and the method of attachment (References 23 and 24). Sufficient empirical data is available on the panel edge stresses for typical stiffened panels when excited by random acoustic loading (Reference 19). Consequently, it is only necessary to predict changes in the panel edge stress due to the attached mass, damping and inplane load in order to use the above data for design purposes. This method is based on the assumption that the addition of the center mass and the application of inplane load do not affect the mode shape in the vicinity of the panel edge.

The addition of a panel center mass and the use of the shaker to simulate the acoustic excitation, will increase the force requirement, not only because of the increased inertia force, but also due to the added back electro-motive force (EMF) induced damping from the shaker. The back EMF damping can be eliminated by switching off the shaker and maintaining open circuits during the acoustic excitation calibration tests. Thus, the combined as well as independent effects of added mass and damping must be determined.

When the psuedo random flight loads are simultaneously applied with the simulated random acoustic loading a biaxial stress field will be obtained in the panel. Insight into the nature of the biaxial stress field at the panel edge can be obtained by considering the instantaneous stress and strain state within the panel.

### 3.1 Panel Stress from Acoustic Excitation

The panel edge axial and lateral modal strains,  $\epsilon_{xe}$  and  $\epsilon_{ye}$ , respectively, are related to the panel mode shape  $w(x,y)$  by

$$\epsilon_{xe} = 0 \quad 15$$

$$\epsilon_{ye} = \frac{h}{2} \left[ \frac{\partial^2 w(x,y)}{\partial y^2} \right] \quad 16$$

$x = \frac{a}{2}, y = 0$

The random acoustic spectrum represented by  $G(\xi_1, \xi_2, \omega)$  in its most general form, includes information on the distribution of the acoustic pressure field over both the surface of the panel and the frequency range.  $\xi_1$  and  $\xi_2$  are separation distances on the surface of the panel given by  $(x_2 - x_1)$  and  $(y_2 - y_1)$ , respectively, and  $\omega$  is the circular frequency. Using the normal modes approach, the mean square panel edge strain  $\overline{\epsilon_{ye}^2}$  due to random acoustic excitation (References 25 and 26) is given by

$$\overline{\epsilon_{ye}^2} = \int_0^\infty \frac{\epsilon_{ye}^2}{|Z(i\omega)|^2} \iint_{A A} w(x_1, y_1) \cdot w(x_2, y_2) G(\xi_1, \xi_2, \omega) \cdot dA_1 \cdot dA_2 \cdot d\omega \quad 17$$

where

$$\frac{1}{|Z(i\omega)|^2} = \frac{1}{M_r^2 \left\{ (\omega_r^2 - \omega^2)^2 + 4\delta^2 \omega_r^2 \omega^2 \right\}} \quad 18$$

and  $\omega_r$  is the panel resonant circular frequency and  $\delta$  is the viscous damping coefficient. The double area integral in equation 17 represents the generalized load or force spectrum. As the white noise spectrum level is independent of frequency, equation 17 can readily be integrated with respect to the circular frequency (Reference 26), using contour integration. to obtain the mean square panel edge strain. After integration, the mean square strain is given by

$$\overline{\epsilon_{ye}^2} = \frac{\epsilon_{xe}^2}{8M_r^2 \omega_r^3 \delta} GF \quad 19$$

where

$$GF = \iint_{A A} w(x_1, y_1) \cdot w(x_2, y_2) \cdot G(\xi_1, \xi_2) dA_1, dA_2 \quad 20$$

is the generalized white noise load spectrum

The panel edge frames are assumed to be stiff in bending. Consequently, the axial strain at the panel edge is zero. The modal panel edge stress and strain at the panel edge are related by

$$\sigma_{ye} = \frac{E\epsilon_{ye}}{(1 - v^2)} \quad 21$$

$$\sigma_{xe} = \frac{Ev\epsilon_{ye}}{(1 - v^2)} \quad 22$$

The mean square panel edge stress is, therefore, given by

$$\overline{\sigma}_{ye}^2 = \frac{\sigma_{ye}^2}{8M_r^2 \omega_r^3 \delta} \quad GF \quad 23$$

$$\overline{\sigma}_{xe}^2 = \frac{v^2 \sigma_{ye}^2}{8M_r^2 \omega_r^3 \delta} \quad GF \quad 24$$

### 3.2 Effect of Added Mass on Panel Stress

The effect of the added panel center mass is to reduce the panel frequency while increasing its generalized mass. The resulting mean square panel edge stress normal to the panel edge becomes

$$\overline{\sigma}_{yeM}^2 = \frac{\sigma_{ye}^2}{8(M_r + M)^2 \omega_d^3 \delta_M} \quad GF_M \quad 25$$

Thus, the ratio of mean square panel edge stress with the added mass and without the added mass is

$$\frac{\overline{\sigma}_{yeM}^2}{\overline{\sigma}_{ye}^2} = \left( \frac{M_r}{M_r + M} \right)^2 \left( \frac{\omega_r}{\omega_d} \right)^3 \left( \frac{\delta}{\delta_M} \right) \left( \frac{GF_M}{GF} \right) \quad 26$$

By substituting the panel frequency,  $f_d$ , at zero inplane load (equation 14) into the above equation, it becomes

$$\frac{\bar{\sigma}_{yeM}^2}{\bar{\sigma}_{ye}^2} = \left( \frac{M_r}{M_r + M} \right)^{1/2} \left( \frac{\delta}{\delta_M} \right) \left( \frac{GF_M}{GF} \right)$$

27

Depending on the magnitude of the added mass, the difference in the panel frequencies with and without the attached mass could be very large. A large difference in the panel frequency could affect the magnitude of both the generalized load spectrum and the damping coefficient (Reference 27) as both are a function of frequency. The empirical data in Reference 19 is in the form of design charts which are derived on the assumption of a fully correlated pressure field. Thus, when using these empirical data in equation 27, the generalized load spectra  $GF_M$  and  $GF$  can be considered to be equal for the same acoustic spectrum level. The magnitude of the panel damping without the mass can be obtained from Reference 27. The value for the mass added panel damping must be estimated as damping data for panels with a heavy center mass are not readily available.

### 3.3 Combined Acoustic and Flight Load Panel Stresses

In this analysis, the axially applied flight loads are assumed to introduce a state of plane stress in the test panel. The lateral stress from the flight loads is, therefore, zero. The instantaneous axial stress,  $\sigma_{xF}(t)$ , which is assumed to be uniform over the width of the panel is, therefore, related to the instantaneous axial strain,  $\epsilon_{xF}(t)$ , by

$$\sigma_{xF}(t) = E\epsilon_{xF}(t)$$

28

At the panel edge, the axial strain from the simulated acoustic loading is zero (equation 15). Consequently, the instantaneous panel edge axial and lateral stresses,  $\sigma_{xAF}(t)$  and  $\sigma_{yAF}(t)$ , respectively, as a result of the combined shaker simulated acoustic and flight loads, are related to the instantaneous axial flight load stress,  $\sigma_{xF}(t)$ , and the instantaneous lateral simulated acoustic load stress,  $\sigma_{yA}(t)$ , by

$$\sigma_{xAF}(t) = \sigma_{xF}(t) + v\sigma_{yA}(t)$$

29

$$\sigma_{yAF}(t) = \sigma_{yA}(t)$$

30

The simulated acoustic loading produces a bending stress in the panel skin which is a maximum at both surfaces and zero at half thickness. The surfaces of the skin are, consequently, subjected to a biaxial stress state and any interaction effects would be expected to initiate from either surface of the skin.

To assist in identifying interaction effects two ratios of inplane to bending load levels as a minimum should be used. With the programmed crack normal to the inplane load, equations 29 and 30 indicate that a more significant effect can be expected by changing the axial flight load stress while maintaining a constant simulated acoustic load level.

### 3.4 Panel Stress Distribution

In the previous sections, the emphasis is placed on predicting the stress at the edge of the panel due to simulated acoustic loading. As long as the crack propagates along the panel edge, the stress at the panel edge due to simulated acoustic loading can be used to predict the stress intensity factor. However, if the crack propagates from the edge to the center of the panel, it will encounter peak stresses at the edge which diminish to zero part way in and then peak again at the panel center.

It is, therefore, necessary to define the stress distribution within the panel. The curvature measured in Reference 16 cannot be used to obtain the stress distribution as fixed-fixed edge conditions were simulated in those tests.

Most theories assume a line attachment for the panel along the fastener line. In reality, the peak panel edge stress location is influenced by the panel edge, especially with asymmetric stiffness, where it gravitates towards the hard corner of the stiffener (Reference 23). The degree of edge flexibility is generally not known accurately. Since empirical data indicates similar lateral stress magnitudes for the edge and the center of the panel, a fundamental modal displacement function given by  $0.5(1 - \cos 2\pi y/b)$  is sometimes used (Reference 19) to represent the lateral panel modal deflection. For large aspect ratio panels, a simply supported axial mode shape can be assumed. The above mode shapes, when used in the Rayleigh Ritz analysis, will produce an over-estimation of the corresponding resonant frequency.

The above mode shapes can be used to describe both the strain and stress distribution within the panel in conjunction with the magnitudes of the strains and stresses determined by the analysis in previous sections or which are empirically determined from measurements at the panel edge. The axial and lateral panel strains,  $\bar{\epsilon}_x(x,y)$  and  $\bar{\epsilon}_y(x,y)$ , respectively, at point  $x, y$ , are given in terms of the peak lateral panel edge strain,  $\bar{\epsilon}_{ye}$ , by

$$\bar{\epsilon}_x(x,y) = -0.25 \bar{\epsilon}_{ye} \left(\frac{b}{a}\right)^2 \left[1 - \cos\left(\frac{2\pi y}{b}\right)\right] \sin\left(\frac{\pi y}{a}\right) \quad 31$$

$$\bar{\epsilon}_y(x,y) = \bar{\epsilon}_{ye} \cos\left(\frac{2\pi y}{b}\right) \sin\left(\frac{\pi x}{a}\right) \quad 32$$

and the corresponding stresses,  $\bar{\sigma}_x(x,y)$  and  $\bar{\sigma}_y(x,y)$ , respectively, in terms of the lateral peak panel edge stress,  $\bar{\sigma}_{ye}$ , by

$$\bar{\sigma}_x(x,y) = \bar{\sigma}_{ye} \left\{ -0.25 \left(\frac{b}{a}\right)^2 \left[ 1 - \cos\left(\frac{2\pi y}{b}\right) \right] \sin\left(\frac{\pi x}{a}\right) + v \cos\left(\frac{2\pi y}{b}\right) \sin\left(\frac{\pi x}{a}\right) \right\} \quad 33$$

$$\bar{\sigma}_y(x,y) = \bar{\sigma}_{ye} \left\{ \cos\left(\frac{2\pi y}{b}\right) \sin\left(\frac{\pi x}{a}\right) - 0.25 v \left(\frac{b}{a}\right)^2 \left[ 1 - \cos\left(\frac{2\pi y}{b}\right) \right] \sin\left(\frac{\pi x}{a}\right) \right\} \quad 34$$

#### 4. Simulation of Acoustic Loading

The degree of acoustic loading simulation possible with an electromagnetic shaker, apart from the previously derived effects on panel frequency and stress, can be determined by considering the generalized load or force spectrum given by equation 20 for both excitations. The increased damping due to back EMF can only be determined experimentally. Again for simplicity, a simply supported panel mode shape is assumed in the subsequent analysis.

##### 4.1 Acoustic Excitation

Two types of acoustic excitation are usually considered, namely; normal incidence and grazing incidence. For the fundamental panel mode with normal incidence noise and even with grazing incidence noise when the acoustic wavelength is considerably greater than the panel length, the pressure field is fully correlated over the surface of the panel. The generalized load spectrum, equation 17, reduces to the separate integral of the mode shapes over the surface of the panel multiplied by a constant noise spectrum level,  $G_0$ . For the fundamental mode of a simply supported panel, the fully correlated generalized load spectrum is reduced to

$$GF_A = \frac{16a^2 b^2}{\pi^4} G_0 \quad 35$$

With grazing incidence excitation for higher order panel modes and for the fundamental mode when the acoustic wave length approaches the panel length, the expression for the generalized load spectrum (Reference 26) is

$$GF_A = \frac{8a^2 b^2 \left[ 1 \pm \cos\left(\frac{\omega a}{c}\right) \right]}{n^2 m^2 \left[ \pi^2 - \left(\frac{\omega a}{cm}\right)^2 \right]^2} G_0 \quad 36$$

where + is used with odd m, n  
 - is used with even m and odd n

If the longest panel side is parallel with the acoustic propagation path, it is possible to excite the (2,1) mode, especially for high aspect ratio panels for which the (2,1) mode frequency can approach the frequency of the fundamental mode. The (2,1) mode, in addition, has a very low damping coefficient due to acoustic radiation cancellation effects. The (2,1) mode can, however, be eliminated by rotating the panel with the long side normal to the propagation path. The (1,2) mode that could now be excited would have a considerably higher frequency than the fundamental mode. Also, the (3,1) mode, after the panel is rotated, will have a small generalized load spectrum in comparison to the fundamental mode.

#### 4.2 Shaker Excitation

Even modes of the panel cannot be excited by the shaker when it is attached to the center of the panel. The shaker will, however, excite all the odd modes of the panel equally when a constant force spectrum level is used. With acoustic excitation, a smaller generalized load spectrum (equation 36) is generally obtained for the higher order panel modes. Unlike the acoustic excitation, the shaker is a point drive system acting at the center of the panel where the mode shape is unity. Thus, the shaker generalized force spectrum reduces to

$$GF_S = F_S$$

37

where  $F_S$  is the constant shaker force spectrum level.

#### 4.3 Ratio of Shaker to Acoustic Force

The generalized load spectrum for acoustic excitation can be written in terms of the force spectrum,  $F_A$ , acting on the panel and given by

$$F_A = a^2 b^2 G_0 \quad 38$$

The ratio of the shaker generalized force spectrum to acoustic generalized load spectrum becomes

$$\frac{GF_S}{GF_A} = \frac{\pi^4 F_S}{16 F_A} \quad 39$$

Thus, the shaker provides greater excitation for the same force spectrum level than does the acoustic excitation.

#### 4.4 Shaker Damping

If the ratio of the shaker coil weight to the panel weight is large, it is to be expected that the damping from the shaker due to back EMF effects would also be large. A damping coefficient in the order of 0.4 could be possible under these circumstances. The effect of damping on the normalized response spectrum of a single degree-of-freedom system is illustrated in Figure 3. The normalized single-degree-of-freedom response spectrum,  $H\left(\frac{\omega}{\omega_r}\right)$ , obtained by multiplying equation 18 by  $M_r^2 \omega_r^4$ , is given by

$$H\left(\frac{\omega}{\omega_r}\right) = \frac{1}{\left[1 - \left(\frac{\omega}{\omega_r}\right)^2\right]^2 + 4\delta^2 \left(\frac{\omega}{\omega_r}\right)^2} \quad 40$$

With a damping coefficient of 0.4, the response peak is shifted towards a lower frequency while the amplification near resonance is almost constant and close to unity. Under these circumstances it would be almost impossible to experimentally detect the resonant frequency and to obtain significant panel response with broad band random excitation.

#### 4.5 Band Limited and Forced Excitation

Limiting the bandwidth of the excitation to increase the excitation spectrum level has been widely used in sonic fatigue testing to obtain a greater stress level in the test specimen. The effect of limiting the excitation bandwidth on the mean square response of a single degree-of-freedom system has been determined from the theory in Reference 28 and is presented in Figure 4, normalized by the mean square response from white noise excitation. In general, the excitation bandwidth has to be at least 3.3 times the 3dB point bandwidth for a loss of 10 percent or less in the rms response level. This method is effective for structures with relatively low damping coefficients and correspondingly high amplification factors. In the case of high damping coefficients producing a broad panel response and near unity amplification, high stress levels can only be obtained by artificially increasing the amplification factor through the use of very narrow band excitation. Narrow band filters have a shape similar to a single degree-of-freedom system over the significant portion of the spectrum and, therefore, can be used to simulate the response of the single degree-of-freedom system. The filter bandwidth should be as close as possible to the desired single degree-of-freedom response 3dB bandwidth.

In acoustic fatigue tests and crack propagation tests, the crack growth and sonic fatigue life are a function of the rms panel stress (References 16 and 19). A Rayleigh distribution for the stress peaks is generally obtained in the test panel. A narrow band forcing function would produce similar effects in the test panel. A Rayleigh distribution of stress peaks is obtained with an ideal rectangular narrow band filter, indicating that the filter shape is not a significant parameter.

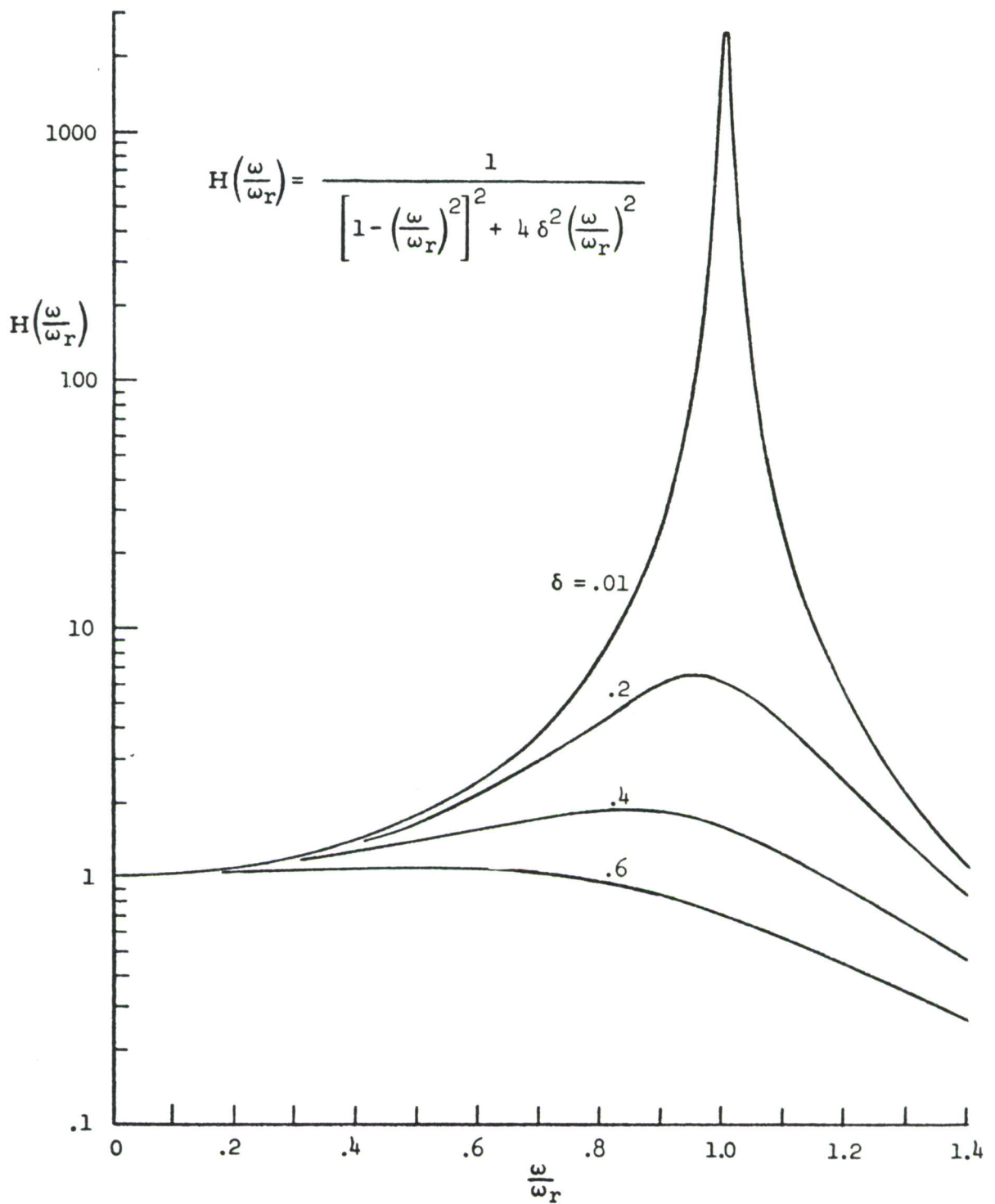


FIGURE 3. NORMALIZED SINGLE DEGREE OF FREEDOM FREQUENCY RESPONSE FUNCTION

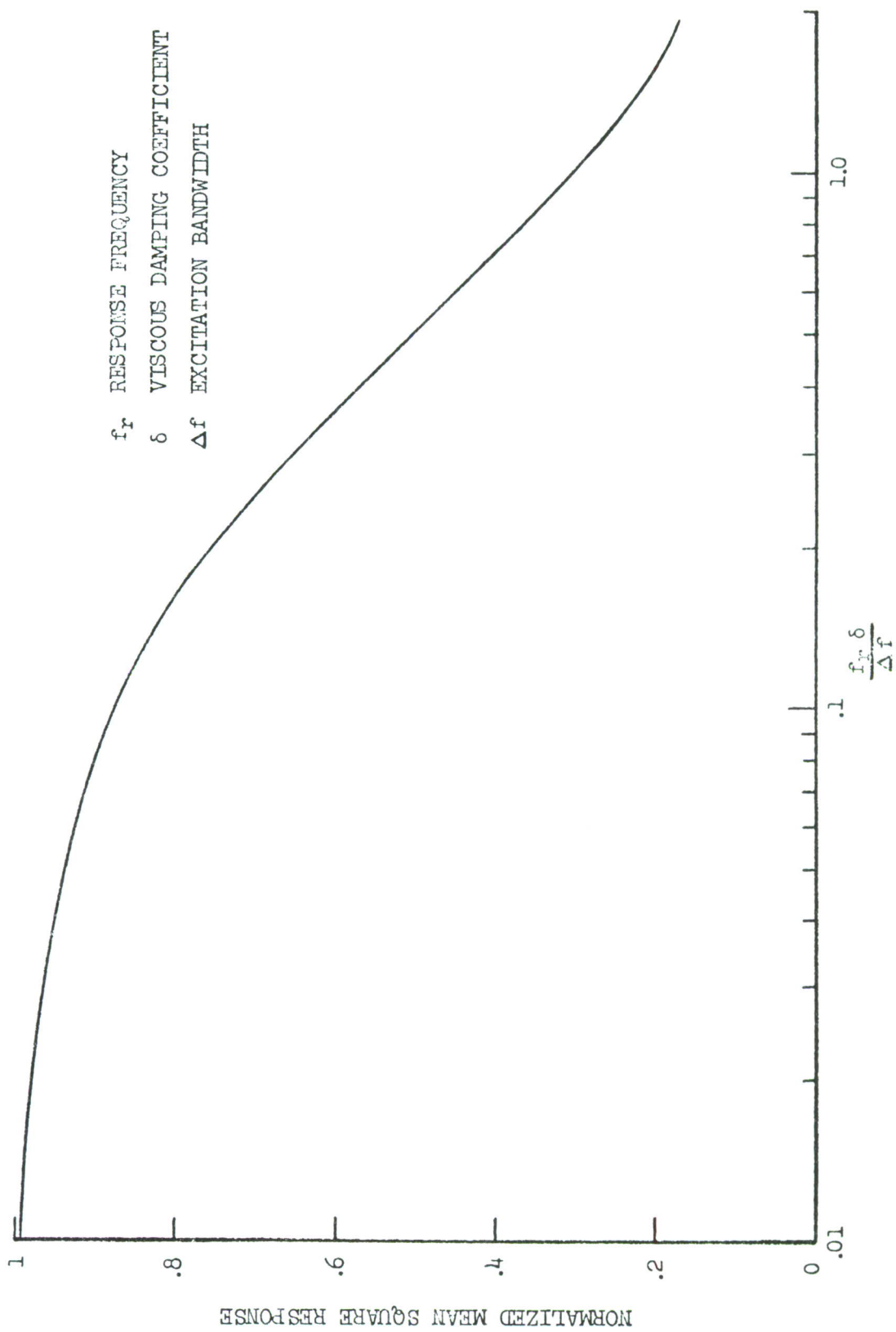


FIGURE 4. EFFECT OF BAND LIMITED RANDOM EXCITATION ON THE MEAN SQUARE RESPONSE OF A SINGLE-DEGREE-OF-FREEDOM SYSTEM

The use of a filter simulated response function will make it difficult to simulate the variation of panel response frequency with the inplane load normally encountered in structures with low damping when excited by broad band noise. With a highly damped response, a reasonable simulation can be achieved with a constant excitation frequency. Some gain in response amplitude can be obtained by employing a lower excitation frequency than the panel fundamental frequency (zero damping).

## 5. Detailed Design of Test Specimen

The final design of the test specimen illustrated in Figure 5 is a compromise between the requirements of the compressive load carrying capability of the panel, the interaction of the inplane loads with the centrally attached mass panel modal frequencies, the panel stresses due to shaker and acoustic excitations, and the capacity of the MTS fatigue machines for accurately controlling the tape load reproduction. This last condition imposed a minimal cross sectional area requirement on the test specimen.

### 5.1 Test Specimen Material and Thickness

7075-T6 aluminum alloy is used as the material for the panel skin, doublers and the frames. The need for a small test specimen cross sectional area and adequate depth for the countersunk fastener hole resulted in the employment of a 0.063 inch panel thickness. The extruded channel section stiffener has a thickness of 0.07 inches, a height of 3 inches and a flange width of 0.85 inches. Good sonic fatigue practice requires the stiffener to be one gage thicker than the panel, while the frame height was selected to ensure a sufficiently high frame bending frequency relative to the panel fundamental frequency, to preclude coupling effects.

### 5.2 Selection of Panel Size

Preliminary analysis indicates that a panel compression load stress and a critical panel buckling stress of 7500 psi and 15,000 psi, respectively, would be realizable with the test specimen while meeting the other design requirements. The 7500 psi difference is the safety margin used to preclude panel buckling, due to the uncertainty in the panel edge stiffness.

For a given panel thickness, the magnitude of the critical panel buckling stress essentially determines the panel width. The critical panel mode is, however, dependent on the panel length. In panels with large aspect ratios, the higher order panel modes produce the lowest critical buckling stresses. A large panel aspect ratio is, however, desirable to obtain a near constant panel edge stress distribution near the center of the longest panel edge in the fundamental mode. Unfortunately, higher order odd panel modes would also be excited by band limited random excitation needed to accomodate the theoretically predicted panel fundamental frequency variation due to the inplane flight loads, at large panel aspect ratios.

NOTE: ALL DIMENSIONS ARE IN INCHES

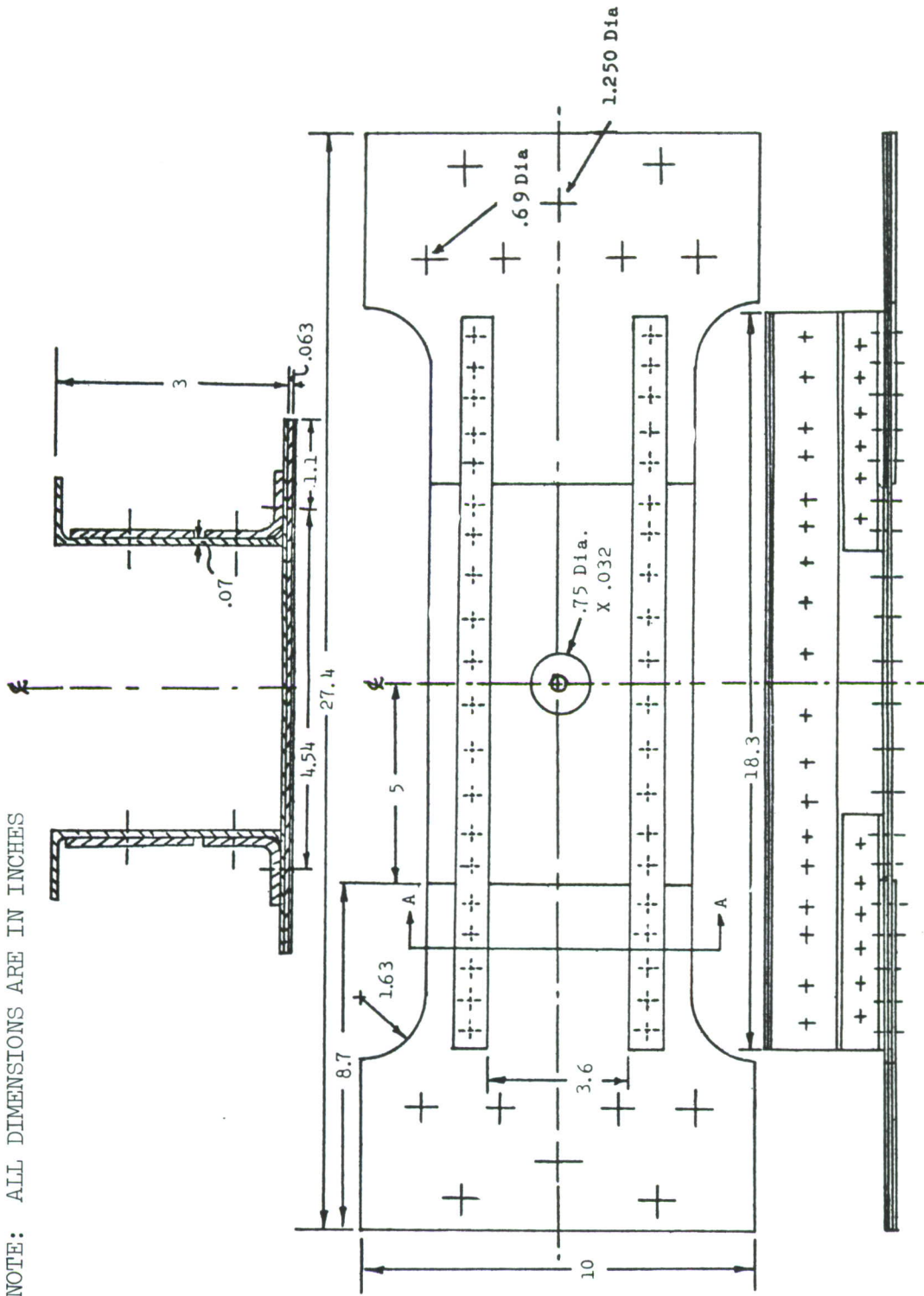


FIGURE 5. TEST PANEL DETAILS

A panel width of 4.5 inches and length of 10 inches are selected on a basis of calculations employing an interative type procedure which is schematically illustrated in Figure 6 . The calculated panel frequency variation with inplane panel stress and aspect ratio are illustrated in Figures 7 and 8, respectively. Equation 11, which is used to determine the panel frequency, may not be accurate for the higher order axial panel modes due to the greater influence of the attached panel center mass on the higher order axial mode shapes.

The analysis, however, indicates the possible occurrence of a 3,1 mode in addition to the fundamental mode at a compressive stress of 7500 psi. The large shaker coil weight of 3.09 pounds is responsible for the relatively low but acceptable panel fundamental frequency.

Panel edge crack growth data from random acoustic excitation (Reference 16) indicates that a stress level in the region of 3300 psi rms would be necessary at the panel edge to produce a crack growth rate commensurate with the available test time. Pretest analysis of the shaker attached panel response indicates that with the level of force available in the acoustic test facility, it is possible to reach 3300 psi rms stress level with a damping coefficient below 2 percent. However, spectrum shaping is necessary to obtain an increased spectrum level around the panel resonance.

No pretest analysis was conducted for the narrow band filtered force simulation of the single degree-of-freedom system response employed in the test program to overcome the extremely high shaker damping. The magnitude of the shaker damping could only be established during the calibration tests, thus the simulation had to be developed experimentally.

### 5.3 Design Detail

The panel ends are designed to transfer the inplane loads from the end grips by friction with the least possible stress concentration effect. The change in panel width employing large radii, together with the staggered doublers are designed to produce a uniform distribution of the axial panel stress across the panel width.

To ensure that the crack propagation is confined to the panel between the fastener lines, a free panel edge extending beyond the frame edge is employed. Analyses were carried out for the panel free edge and the stiffener frame flange buckling, the inter rivet buckling and the long column frame buckling up to the critical panel buckling stress. Panel fastener spacing was also checked for sonic fatigue requirements while fastener edge distances, compatible with good fatigue design, are employed throughout the test specimen. Eight 3/16 inch diameter countersunk fasteners are employed around the center of the long panel sides to represent actual airframe construction. The shallow head countersunk fasteners are selected to avoid knife edges in the fastener holes.

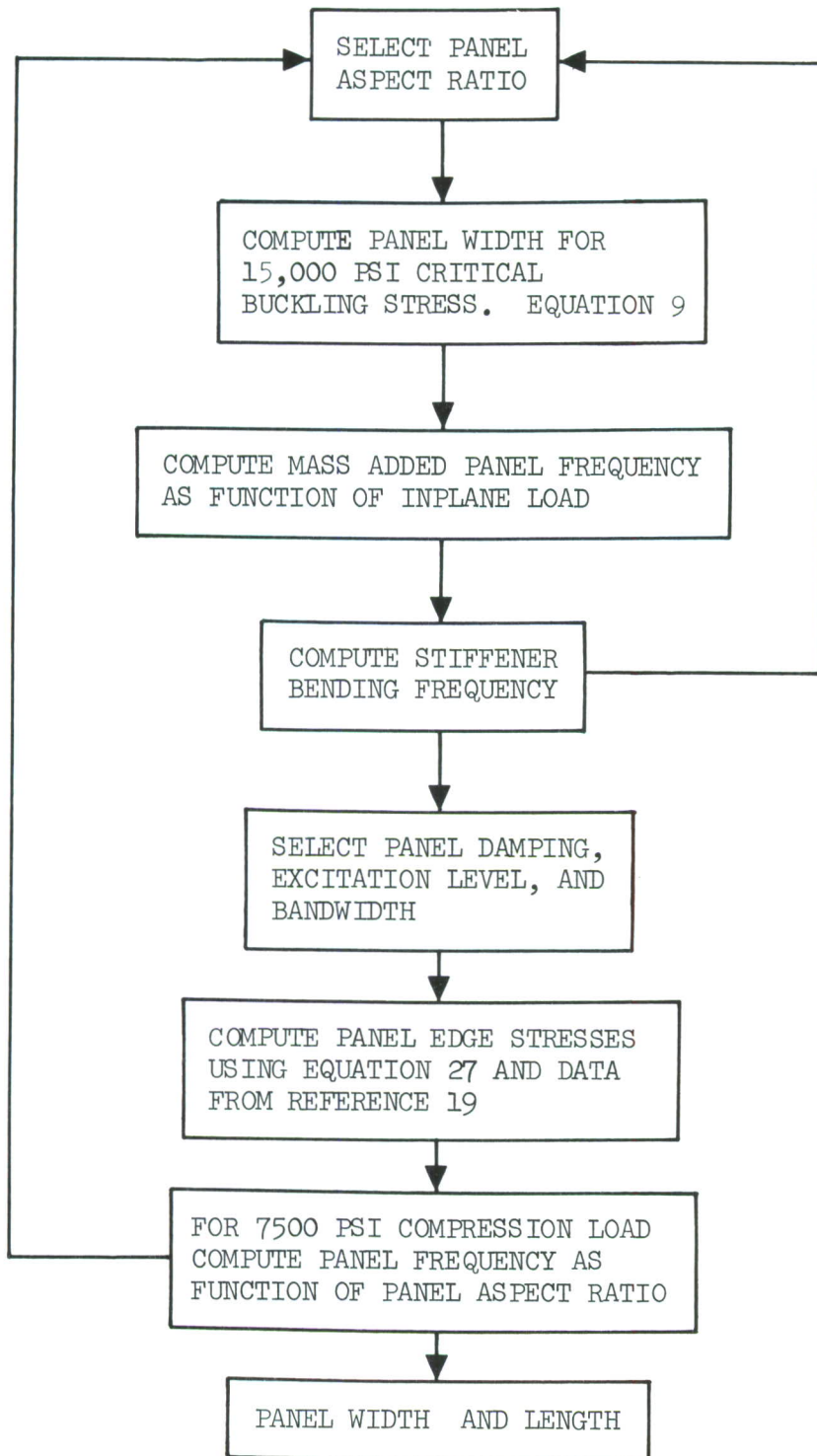


FIGURE 6. ITERATIVE PANEL DESIGN PROCEDURE

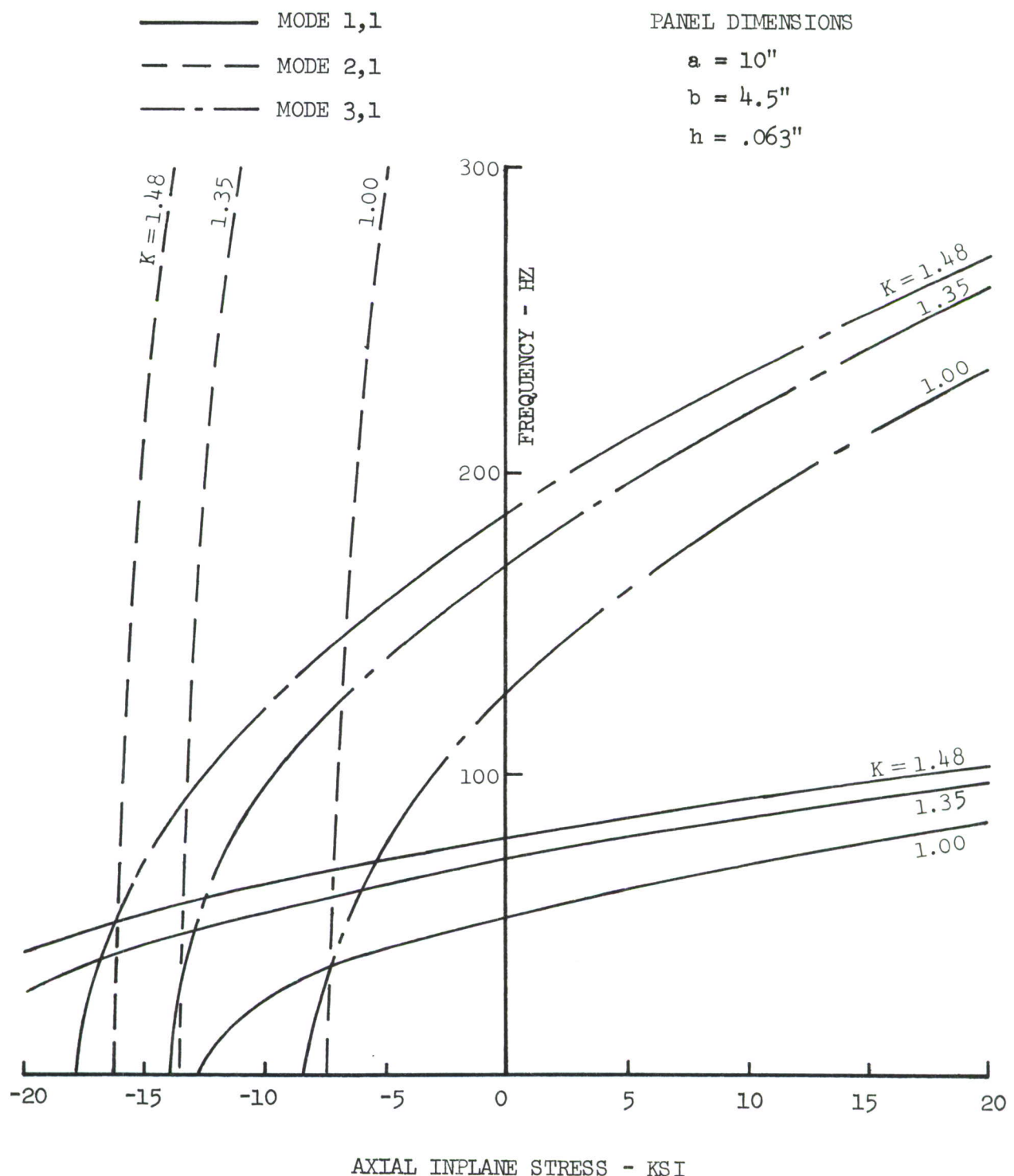


FIGURE 7. EFFECT OF AXIAL INPLANE STRESS ON PANEL FREQUENCY

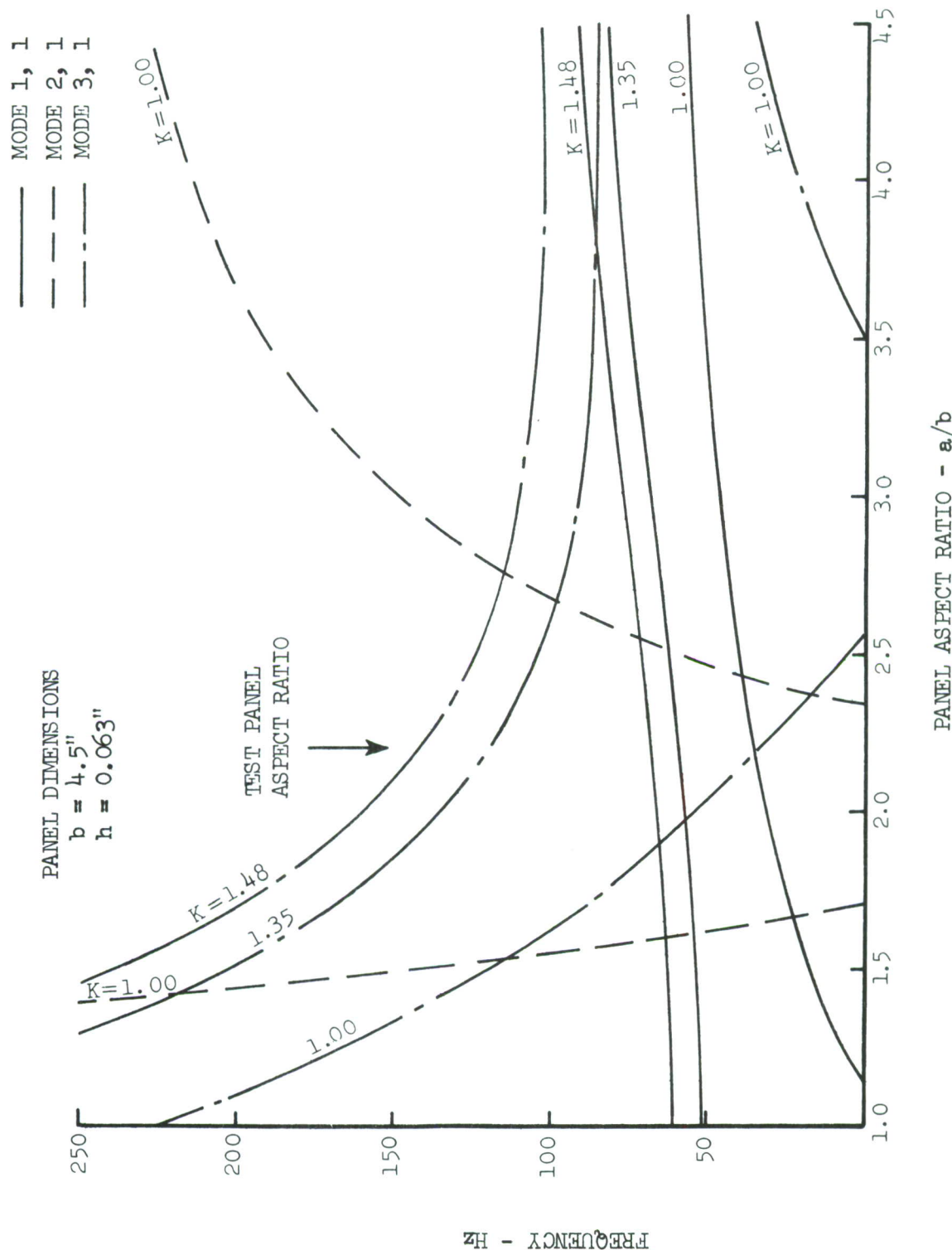


FIGURE 8. EFFECT OF ASPECT RATIO ON FREQUENCY OF PANEL SUBJECTED TO COMPRESSION STRESS OF 7500 PSI.

The B&K force gage is bolted as close to the panel surface as practical to measure the true force, free of flexibility effects (Figure 9). The panel center is reinforced by bonding a 0.032 inch thick circular doubler (0.75 inch diameter) to each side of the panel per Lockheed specification LCP79-2061-Type 20. A washer is inserted between the doubler and the force gage to provide a more gradual stress transfer to the panel. The shaker drive rod is attached to the other side of the force gage through a machined adapter. Analysis of the shaker rod bending frequency was conducted to assist in reducing the probability of resonant coupling with the panel fundamental mode.

#### 5.4 End Grip Design

Existing MTS fatigue machine end grips are modified by machining the outer end grip surfaces parallel to the panel axis. The upper attachments (Figure 10) are machined from one inch thick steel plate to fit on the outer surface of the end grips and pick up the frame loads through a full length doubler on each frame flange. The lower attachments are machined from 1/4 inch thick steel plate to the same shape as the panel ends and fit over the panel ends to provide a friction type grip with a gradual load transfer into the face sheet. The test panel ends fit over the other outer surface of the end grips. This arrangement is dictated by the need for the load axis to pass through the centroid of the test specimen cross section to eliminate frame bending and the associated panel stress.

#### 5.5 Fatigue Crack Initiation

A single simulated crack is employed normal to the panel fastener line in one of the countersunk fastener holes (Figure 11) nearest to the center of the panel, in all test panels except the calibration panel. The simulated crack is made, initially, by cutting a slot with a jeweler's saw into the face sheet at the selected fastener hole, prior to final assembly. After assembly, with the test specimen mounted in the fatigue machine, the test specimen is fatigue loaded at a reduced level relative to the test load until a 0.01 inch long crack is obtained at the end of the slot. An additional simulated crack is made parallel to the fastener line (Figure 12) in the panel center fastener hole adjacent to the above crack, in two of the test panels subjected only to shaker simulated acoustic loading. The additional crack location is typical of a sonic fatigue induced crack. Crack initiation in this instance is by the application of shaker simulated random loading.

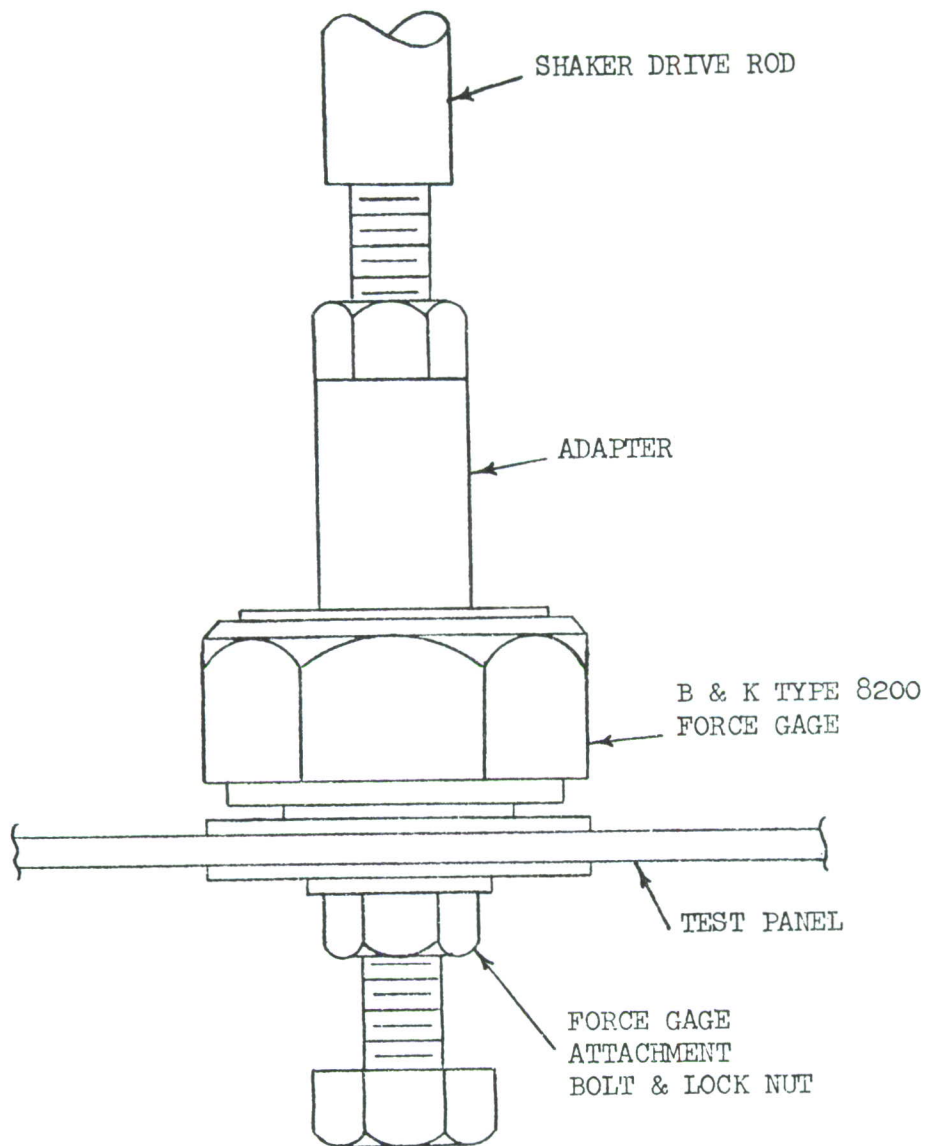


FIGURE 9. FORCE GAGE

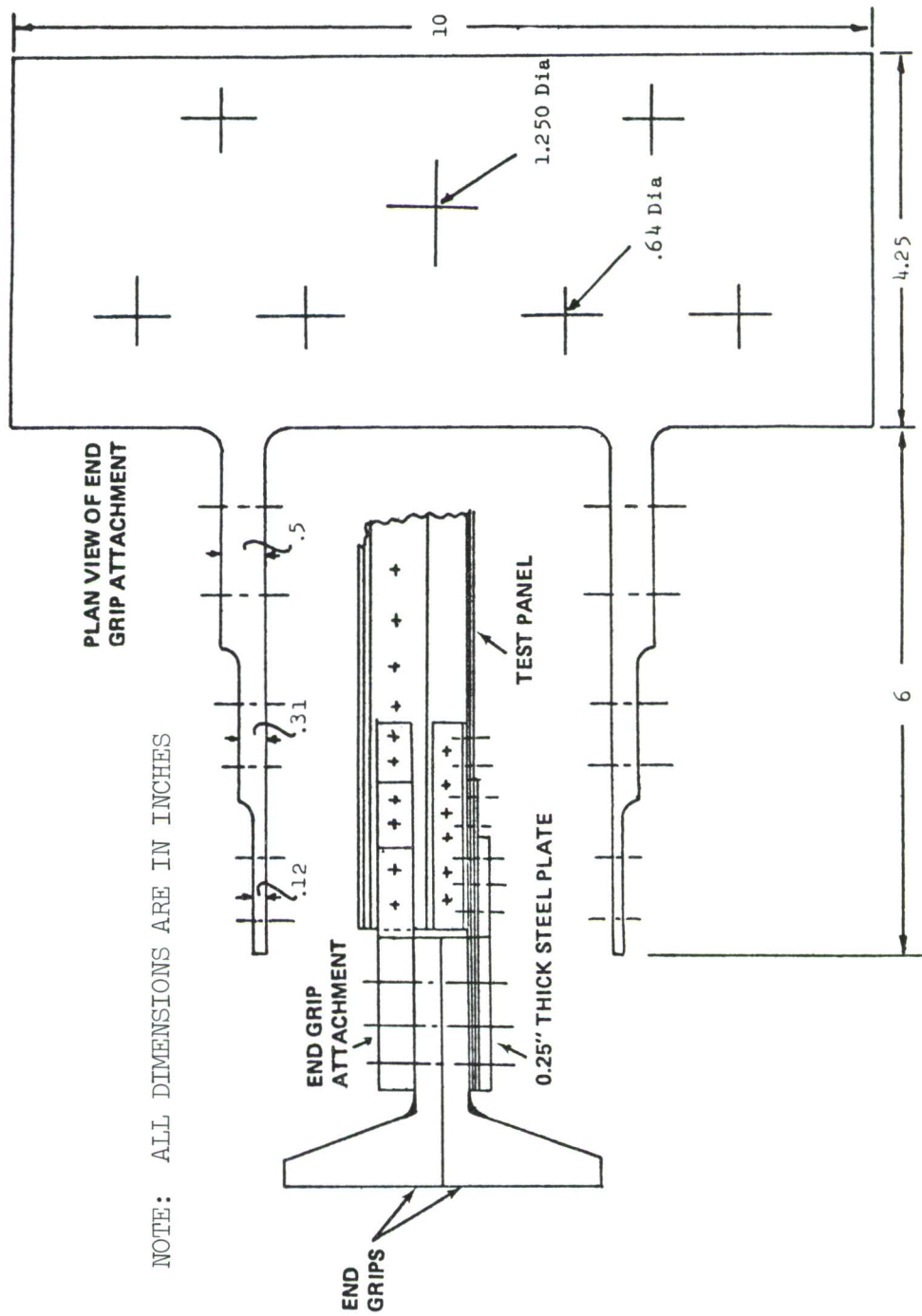


FIGURE 10. PANEL END GRIP ASSEMBLY

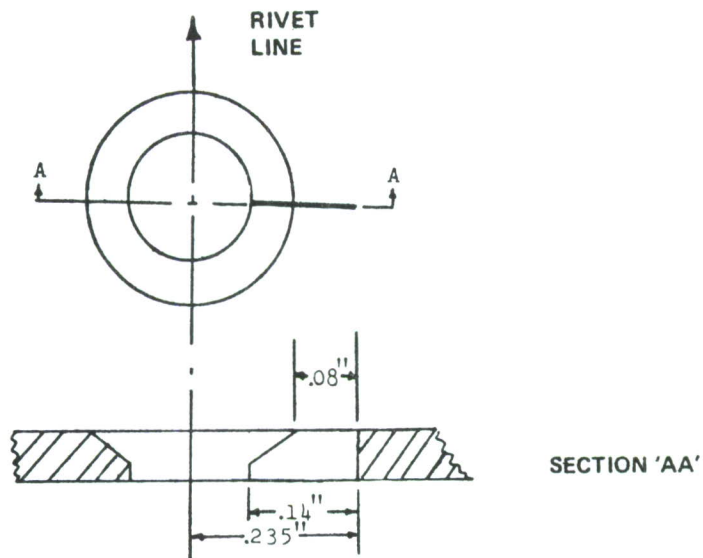


FIGURE 11. PRECRACK FOR COMBINED LOADS

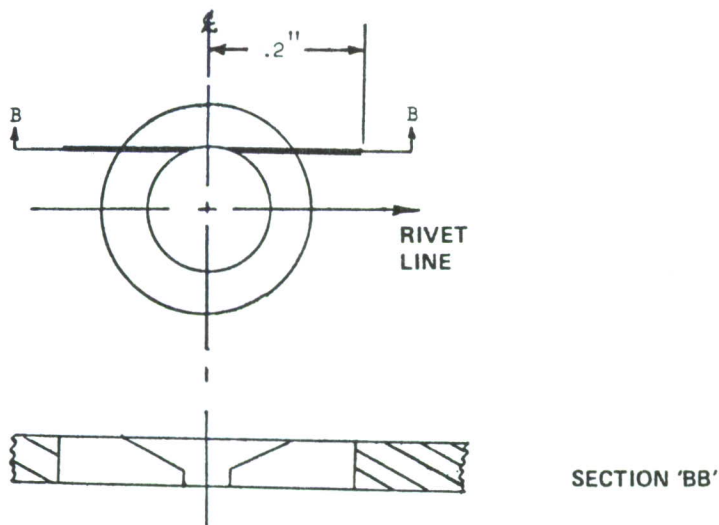


FIGURE 12. PRECRACK FOR SHAKER SIMULATED  
ACOUSTIC LOADING

### III LOAD HISTORIES AND SPECTRA

#### 1. Introduction

The discussion in this section describes the development, from existing data, representative flight load and acoustic test spectra and, thereafter, the corresponding time histories which are recorded onto magnetic tapes. The flight load tape typically contains pseudo random flight-by-flight load time histories of representative runway, landing impact, gust and maneuver load spectra. The acoustic tape contains typical takeoff and accelerated flight jet noise time histories. These tapes will be used to control the load applied to the test panels by both the MTS fatigue machines and the electro-magnetic shakers.

The flight load spectra along with the time histories, in general, have to be modified to conform to the requirements imposed by the specimen design, test facility capability and the load tape duration. Truncation of the low level portion of the load spectra, for example, is carried out due to the limitation on number of flight cycles that can be accommodated within a reasonable flight duration. This truncation permits the application of high amplitude cyclic loads at lower frequency and with high accuracy.

The real time simulation of the ground acoustic loading, in this program, amounts to a duration of approximately 18 seconds of the total acoustic loading of each flight. The duration of the flight portion is determined by the flight load requirements. The lower level, but very much longer duration of the flight acoustic load, can introduce a significant effect on crack growth which is spread over a longer period of time. To compensate for this situation, the level of the flight acoustic loading can be increased in a trade-off against time, to conform to the flight duration imposed by the flight spectral requirements.

The analysis in Section II indicates that at least two ratios of flight loads to acoustic loads are desirable to identify trends. The propulsion configurations in advanced short takeoff and landing (STOL) transport type airplanes indicate that both upper and lower wing flight loads in combination with acoustic loads are of interest. The upper and lower wing spectra are generally of different magnitudes. Thus the employment of the upper and lower wing load spectra with a constant level acoustic excitation will satisfy both of the above needs.

#### 2. Flight-by-Flight Loads

The flight-by-flight load spectra are generally based on mission profiles and operation load spectra for a specific aircraft category. Such spectra indicate the relative frequency but not necessarily the sequence with which specific loading levels are reached or exceeded during a specified period of time. The mission profile defines the number and duration of each mission type and the number of landings for the life of the aircraft. This data estab-

lishes the proper mix ratio to be used in the load tapes. The individual alternating load cycles within each mission is selected randomly from the pool of appropriate load spectra corresponding to the specific mission. The accumulated number of load cycles for each mission category is based on the load spectra and the duration of both the acoustic and flight loadings for each flight.

## 2.1 Basic Mission and Spectral Data

The basic mission profiles and the flight-by-flight load spectral data employed in this program have been obtained from References 29 and 30 for a STOL type airplane. The simplified three mission profiles, for the STOL airplane, are summarized in Table 1 and schematically illustrated in Figure 13. The corresponding spectra for these missions are summarized in Tables 2 through 5. Table 2 represents the taxi, takeoff and landing roll spectra. The maneuver and gust load spectra (Table 3(a)) and the corresponding turbulence parameters (Table 3(b)) are based on MIL-A-8866A, Tables VII and VIII. Table 4 contains the gust-plus-maneuver spectrum for the low level resupply mission and Table 5 contains the landing impact spectrum.

As a further simplification, the three mission catagories (Table 1) are reduced to two, namely, the typical and the low level resupply missions, by combining the basic training missions with the typical missions. The duration of each flight within the two missions has been fixed at 0.5 hours and 0.9 hours for the low level resupply and the typical mission, respectively. Since the number of typical missions is approximately three times that of the low level resupply missions, a total number of 40,250 takeoffs and landings are calculated for the 30,000 hour life of the airplane using the above flight durations. Touch-and-go landings have been omitted.

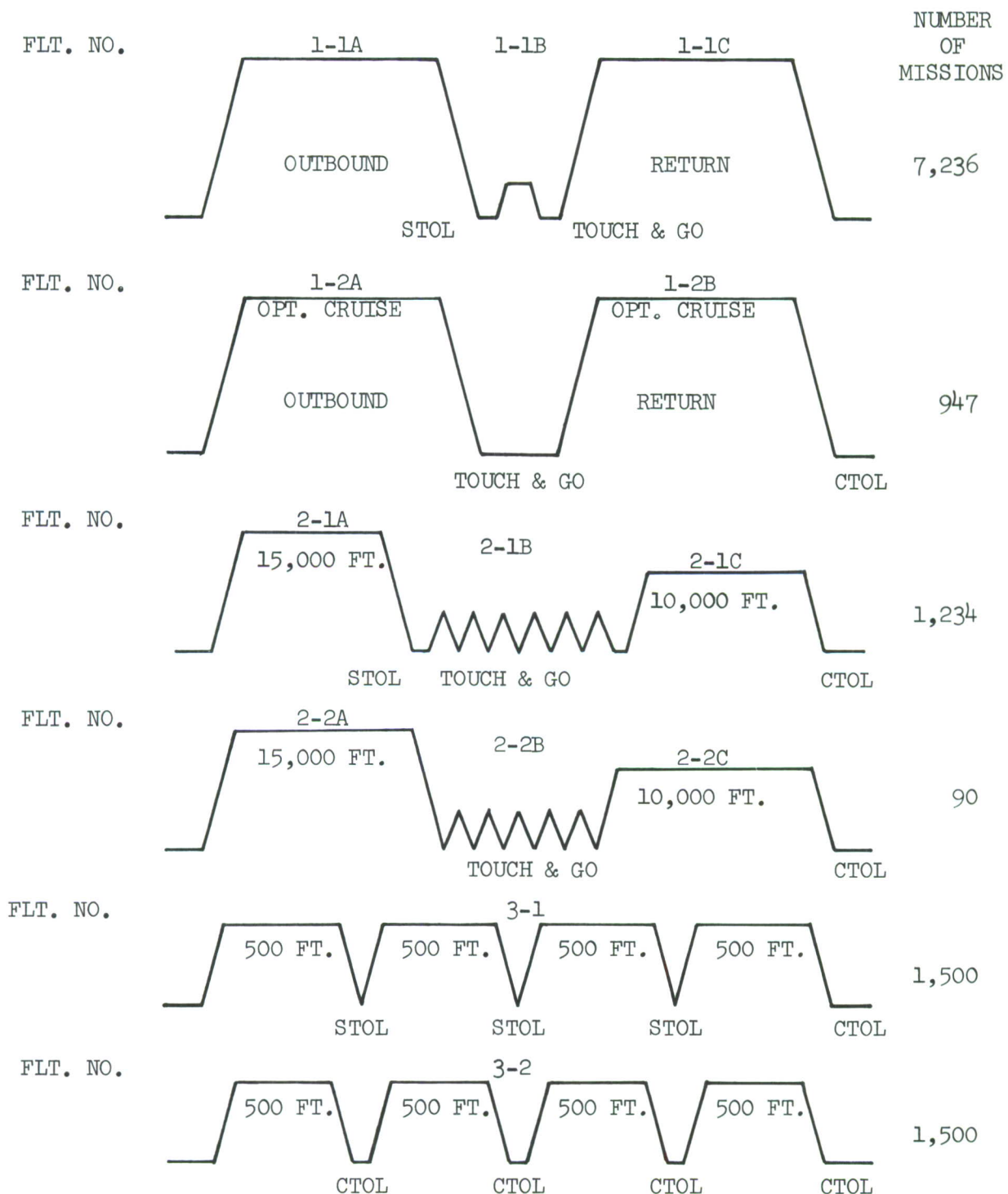
Simulated flight duration of approximately 28 seconds takes into account an 18 second duration for the takeoff acoustic loading and approximately a 10 second duration for the flight load. The number of flights that can be accomodated on a 90 minute tape is, therefore, around 185 which also allows time for the initial calibration signal. This permits a selection of 74 missions of which 18 missions are considered to be in the low level resupply mission category and the remaining 56 missions in the typical mission category. Table 1 and Figure 13 indicate that each low level resupply mission has four flight segments, while a typical mission has two flight segments. Hence, the actual number of flights that can be accomodated by a 90 minute duration load tape is 184.

The actual duration of the ground and flight section in each flight does vary for the upper and lower wing surface loading and differs slightly from the above values in the final tape. The intention, however, is to maintain the same values for these flight sections in both upper and lower wing surface load tapes.

TABLE 1. PABST AIRCRAFT UTILIZATION (MODIFIED SPECTRUM)

Plt. No.	Description	Landing <sup>a</sup> Per Mission				Service Life				Number of Missions	Pay Load		
		Mission Length Flt. Hrs. N Mi.	STOL	CTOL	Touch and Go	Hrs. Per Landing	Flight Hrs.	% of Total Flt. Hrs.	STOL	CTOL	Touch and Go	Total	% of Total
1-1	Typical	2.765	489	1	1	.92	20007	66.6878	7236	7239	21708	47.0849	7236
1-2	Typical	2.000	715	1	1	1.00	1804 21901	6.3131 73.0009	7236	417 8186	1841 8186	4.1081 51.1930	747 7933
2-1	Basic	1.603	394	1	1	6	1974	6.5748	1234	7404 7944	9572	21.4125	1234
2-2	Training	1.400	370	1	1	6	.20	126 2100	4200 6.9948	90 1324	630 1032	1.3664 22.7789	90 1324
3-1	Low Altitude	2.000	582	3	1	.5	3000	9.9997	4500	1500	6000	13.0141	1500
3-2	Re-Supply	2.000	573	4		.5	.3000 6000	.9.9997 19.9994	4500	6000 7500	6000 12000	13.0141 26.0282	1500 3000
							3000	100.0000	12970	17007	16127	46104	100.0000
												12509	

NOTE: Table is Taken From Table A Of Reference 30, Attachment 1.



NOTE: Figure Taken From Reference 30.

FIGURE 13. PABST AIRCRAFT UTILIZATION (SIMPLIFIED)

TABLE 2. TAXI, TAKEOFF, AND LANDING ROLL  
SPECTRUM (PREPARED AND SEMI-  
PREPARED RUNWAYS)

$\pm \Delta g$	CUMULATIVE OCCURRENCES/1000 TAXI'S		
	Prepared Runways	Semi-Prepared Runways	Unprepared Runways
.1	194,094	280,000	280,000
.2	29,094	100,000	210,000
.3	2,094	30,000	130,000
.4	94.155	5,000	68,000
.5	4.155	750	22,000
.6	0.155	100	5,300
.7	0.005	15	900
.8		2	130
.9		0.3	20
1.0		0.05	3
1.1			0.5

NOTE: Table Taken From Reference 30, Attachment 3.

TABLE 3(a). MANEUVER LOAD SPECTRA FOR  
TRANSPORT AIRCRAFT

Spectrum Equation

$$1. \quad \Sigma N(\Delta g) = N_{o1} e^{-\Delta g/b_1} + N_{o2} e^{-\Delta g/b_2}$$

$$2. \quad \Sigma N(\Delta g) = N_{o1} e^{-\Delta g^2/2b_1^2} + N_{o2} e^{-\Delta g^2/2b_2^2}$$

Mission Type		EQ. #	$N_{o1}$	$N_{o2}$	$b_1$	$b_2$
$C_{Assault}$ *	Climb	+	$2.7 \times 10^5$	$2.5 \times 10^2$	.0492	.1646
		+	$9.0 \times 10^4$	50.0	.0869	.2877
	Cruise	+	$4.0 \times 10^4$	$10^3$	.0523	.0986
		+	$2.1 \times 10^4$	62.0	.0921	.2621
	Descent	+	$1.9 \times 10^5$	0	.0543	0
		+	$1.7 \times 10^5$	$4.5 \times 10^2$	.0942	.2311
$C_{Transp.}$ (Logistics) **	Climb	+	$9.0 \times 10^3$	$10^3$	.1200	.1614
		+	$2.6 \times 10^5$	54	.06157	.2942
	Cruise	+	$4.52 \times 10^2$	95	.1452	.1885
		+	$9.0 \times 10^4$	75	.0408	.1687
	Descent	+	$8.83 \times 10^3$	$2.2 \times 10^2$	.1336	.1827
		+	$3.5 \times 10^5$	$4.0 \times 10^2$	.05509	.19054
$C_{Transp.}$ (Training) **	Climb	+	$1.6 \times 10^5$	0	.0598	0
		+	$5.2 \times 10^5$	$2.7 \times 10^3$	.0835	.1820
	Cruise	+	$4.0 \times 10^4$	0	.0566	0
		+	$4.6 \times 10^5$	40	.0843	.2966
	Descent	+	$5.5 \times 10^4$	$9.5 \times 10^3$	.0476	.0841
		+	$5.4 \times 10^5$	$1.6 \times 10^4$	.0670	.1922

\* MIL-A-8866A Table VIII Assault Spectrum for Transport Airport

\*\* MIL-A-8866A Table VII Transport and Training Spectra For Transport Aircraft

NOTE: Table Obtained From Reference 30, Attachment 3.

TABLE 3(b). TURBULENCE PARAMETER

Altitude (Ft)	Mission Segment	Direction 1	P <sub>1</sub>	b <sub>1</sub> * (Ft/Sec)	P <sub>2</sub>	b <sub>2</sub> * (Ft/Sec)	L (ft)
0 - 1,000	Low Level Contour	Vertical	1.00	2.68	$10^{-5}$	10.55	500
0 - 1,000	Low Level Contour	Lateral	1.00	3.08	$10^{-5}$	13.92	500
0 - 1,000	Climb, Cruise, Descent	Vert & Lat	1.00	2.50	.005	5.00	500
1,000 - 2,500	Climb, Cruise, Descent	Vert & Lat	.42	2.93	.0033	5.75	1750
2,500 - 5,000	Climb, Cruise, Descent	Vert & Lat	.30	3.23	.0020	7.70	2500
5,000 -10,000	Climb, Cruise, Descent	Vert & Lat	.15	3.20	.00095	8.25	2500
10,000 -20,000	Climb, Cruise, Descent	Vert & Lat	.062	2.59	.00028	8.33	2500
20,000 -30,000	Climb, Cruise, Descent	Vert & Lat	.025	2.11	.00011	7.92	2500
30,000 -40,000	Climb, Cruise, Descent	Vert & Lat	.011	1.63	.000095	5.48	2500
40,000 -50,000	Climb, Cruise, Descent	Vert & Lat	.0046	1.44	.000115	3.87	2500
50,000 -60,000	Climb, Cruise, Descent	Vert & Lat	.0020		.000078	2500	
60,000 -70,000	Climb, Cruise, Descent	Vert & Lat	.00088		.000057	2500	
70,000 -80,000	Climb, Cruise, Descent	Vert & Lat	.00038		.000044	2500	
above 80,000	Climb, Cruise, Descent	Vert & Lat	.00025		0	2500	

NOTES: (1) Parameter values labeled "Vert & Lat" are to be used equally in both the vertical and lateral directions.

(2) For altitudes below 2,500 ft. the scale of turbulence, L, can be assumed to vary directly with altitude.

(3) These values of b<sub>1</sub> and b<sub>2</sub> are based on equivalent airspeed - AGPA computer program requires equivalent airspeed

TABLE 4. LOW LEVEL RE-SUPPLY MISSION  
GUST PLUS MANEUVER LOAD SPECTRUM

Alt. = 1000 Ft.

V = 300 KEAS

$\pm \Delta g$ c.g.	Cumulative Occurrence Per Flight Hour
.1	1,300
.2	420
.3	160
.4	52
.5	17
.6	4
.7	2.8
.8	0.95

NOTE: Table Taken From Reference 30, Attachment 3.

TABLE 5. LANDING IMPACT INCREMENTAL LOAD SPECTRUM

$\Delta g$	CTOL Per 1,000 Landings	STOL Per 1,000 Landings	
		G.W. < 153,000#	G.W. > 153,000#
.1	530		
.2	50	900	800
.3	9	600	290
.4	4.3	450	160
.5	2.2	320	94
.6	1.3	250	60
.7	0.65	210	39.1
.8		163	25.02
.9		133	14.04
1.0		110	10.99
1.2		70	4.58
1.4		50	
1.6		37	
1.8		26	
2.0		20	
2.2		15.5	
2.4		11.3	
2.6		7.4	
2.8		4.8	
3.0		3.2	
3.2		2.2	
3.4			

NOTE: Table Taken From Reference 30, Attachment 3.

## 2.2 Lower Wing Surface Load History

Except for portions of the takeoff and landing runs, the flight conditions will impose tension loads on the lower wing surface. The flight-by-flight load history is generated using the following described techniques. A total of 50 load cycles can be accommodated within each flight segment when using the preselected flight duration of 10 seconds and a nominal loading frequency of 5 cps. There are 72 flight segments for the 18 low level resupply missions. The total number of load cycles is then 3600 cycles. The truncated load spectrum is shown in Figure 14 together with a spectrum based on Table 4 with 18 missions (36 flight hours). The number of cycles at selected load levels are also shown in Table 6. The load spectra for the typical mission and the low level resupply mission are presented separately. The high load level truncation is used to eliminate the infrequent high load. The low load level truncation is based on the limit of the total number of 3600 cycles allotted to the 18 low level resupply missions. The two high and low load level truncation justifications apply equally for the other spectra.

Similar truncation is carried out for the spectrum of the 56 typical missions. The typical mission has two flight segments. Based on 50 cycles per flight segment, the total number of load cycles is 5600 cycles which is more than enough to accommodate the whole spectrum as given in Table 3. However, the low load level truncation at  $\Delta g = 0.2$  is selected and 2600 cycles of  $\Delta g = 0.0$  are inserted to replace the surplus cycles. The high load level truncation is at  $\Delta g = 0.7$  which is the same as for the low level resupply missions. The resulting truncated spectrum is shown in Figure 14 and Table 7.

The taxi, takeoff, and landing roll spectrum is reduced to a constant sustained load covering the duration of the entire ground load segment of the derived spectrum. This simplification can be justified by the reasoning that compressive cyclic loads about a compressive mean load do not have significant effect on the crack growth behavior. The value of the sustained load factor is selected to be 0.5g based on the critical buckling load of the test panel.

From Table 5, it can be seen that the once per landing incremental load factor (for landing impact) is approximately 0.6 to 0.7g. This value is similar to the sustained load level considered for the ground load segment. Hence, the landing impact spectrum is not considered in the generation of the load history.

The flight-by-flight load history is generated from the modified load spectra using a computerized randomization procedure. From the total of 18 low level resupply missions and 56 typical missions, 7 mission types composed of 4 low level and 3 typical mission types are selected for randomized repetition. The sequences of the individual load cycles within each of the four flight segments in a low level resupply mission and the three flight segments in the typical mission are randomized. The number of repetitions for each of the 7 mission types and the number of individual load cycles within each mission type are selected to match as close as possible the flight load spectra in Figure 14. Thus in the low level missions, Mission Types 1 and 2 are repeated five times each and Mission

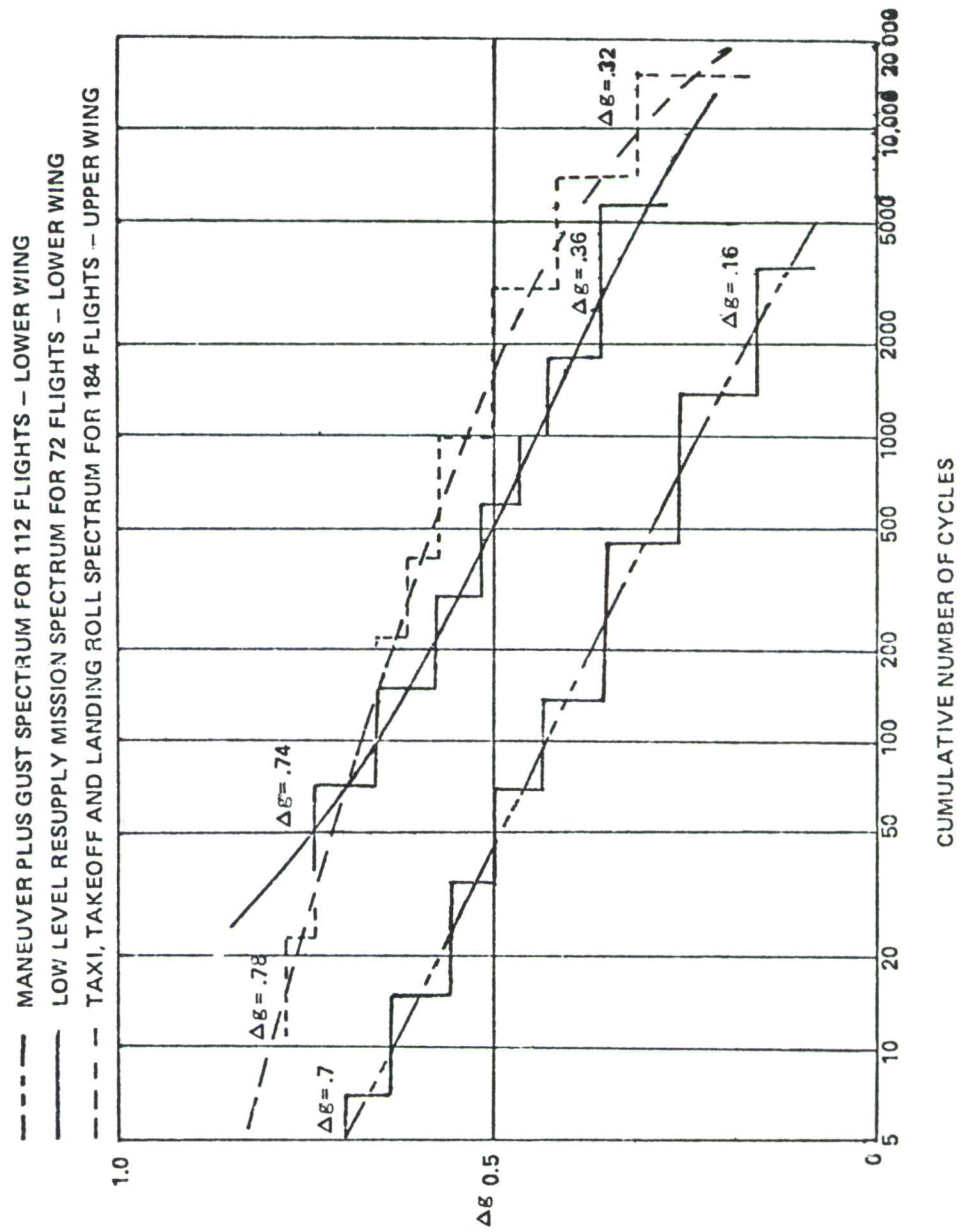


FIGURE 14. TRUNCATION OF LOAD SPECTRA

TABLE 6. THE TRUNCATED LOW LEVEL RE-SUPPLY  
MISSION SPECTRUM FOR 18 MISSIONS

$\Delta g$	No. of Cycles
0.74	72
0.66	78
0.58	150
0.52	300
0.48	400
0.44	800
0.36	1800

TABLE 7. THE TRUNCATED TYPICAL MISSION  
SPECTRUM FOR 56 MISSIONS

$\Delta g$	No. of Cycles
0.70	7
0.64	8
0.56	20
0.50	35
0.44	50
0.36	310
0.26	950
0.16	2100

Types 3 and 4 are repeated 4 times each. In the typical mission, Mission Type 1 is repeated 40 times and Mission Types 2 and 3 are repeated 4 times each. The number of mission types and the number of repetitions are selected using as a guideline the number of load cycles at the high truncation load level. The loads with a frequency of occurrence less than once-per-flight are generally assigned to one mission type, making it more severe.

The conversion factor from 1g flight load to stress is 7400 psi as shown in Reference 29. The ground load and landing impact is simulated using a sustained constant load factor of -0.5g. The conversion factor from 1g ground load to stress is 5000 psi (Reference 29).

### 2.3 Upper Wing Surface Load History

A composite flight-by-flight load history can be generated also for the upper wing surface following a similar procedure to that described above for the lower wing surface. However, significant quantitative differences exist between the two composite load histories primarily because on the upper wing surface the tension cyclic loads are induced by the ground loads and the compressive cyclic loads are induced by the flight loads. This consideration leads to the selection of an 18 second ground load segment and a 10 second flight load segment. The selection of a 10 second flight duration instead of a shorter time span is required to maintain the same flight acoustic load duration as employed in the lower wing surface load history.

Based on the 18 second duration on the ground and a nominal loading frequency of 5 cps, the total number of cycles obtained for the 184 ground load segments is 16,560 cycles. The taxi, takeoff and landing roll spectrum, shown in Table 2, is modified accordingly. The high load level truncation is selected to be 0.8g. The low load level truncation is limited by the total number (16,560) of cycles allowed for ground load segments.

One additional step was included in constructing the taxi, takeoff, and landing roll spectrum for the basic set of 72 missions (a total of 184 flight segments) to reflect a proper mix of the three runway configurations which are: (1) unprepared runway, (2) semi-prepared runway, and (3) prepared runway. A runway configuration mix for the three runway configurations is obtained using the mission profile data in Table 1. The resulting runway configuration mix includes 42 percent of runway (1), 24 percent of runway (2), and 34 percent of runway (3). Based on the above mix of runway configurations, the milder spectrum shown in Figure 14 and in Table 8, has been constructed. The tension loads induced by the landing impacts are neglected.

A similar randomization procedure to that employed for the lower wing surface is used to generate the flight-by-flight ground load time history. Based on the load spectra in Table 8, eight basic ground load segments are selected, each repeated 23 times in a randomized sequence. The individual load cycles within each segment are also randomized.

The  $lg$  stress conversion factor is equal to 5000 psi. The somewhat arbitrary sustained load factor of  $-lg$  is selected for the flight segments. This value corresponds to a compression stress of 5000 psi which is just below the buckling limit calculated for the test panels.

TABLE 8. THE TRUNCATED TAXI, TAKEOFF, AND LANDING SPECTRUM FOR 72 MISSIONS

Incremental Load Factor g's	Number of Cycles
0.78	23
0.74	27
0.70	50
0.66	120
0.62	280
0.58	600
0.50	2000
0.42	4000
0.32	7720*

\* This value should be 9460 cycles in order to be consistent with the 184 ground load segments which is 16,560 cycles. However, because the accumulative incremental load factor falls off significantly beyond 14,820 cycles the lower value for the 0.32 level is used.

### 3. Acoustic Loads

The acoustic load levels and durations are required to be established for the ground and flight regimes for simultaneous application with the corresponding flight-by-flight loads. The acoustic spectrum level developed for the test program is based on the estimated takeoff spectrum level of 139 dB on the wing of a STOL type advanced transport airplane (Reference 29). The flight spectrum level, however, is not defined and is calculated using the takeoff noise level and a variation in the noise level with airplane speed based on the fifth power of the relative jet exhaust velocity.

The duration of the acoustic loading is generally obtained by relating the airplane power utilization profile and the corresponding jet noise levels

to an equivalent duration at the takeoff noise level (Reference 27). For sonic fatigue analysis, the equivalent duration is computed using a trade-off procedure relating acoustic level to duration through random fatigue S/N data for the appropriate airplane structure. The power utilization profile includes engine maintenance runs, aircraft taxi, takeoff and landing in addition to the flight missions (Reference 27). Thus, the progressive reduction in the noise level during the takeoff run and the subsequent flight with increasing airplane speed and altitude (Reference 27) is accounted for in the tradeoff procedure.

The duration of the ground utilization up to liftoff and after touchdown, was estimated at 18 seconds per flight in the absence of detailed information. This represents a total duration of 201 hours for the 40,250 flights. The duration of the flight acoustic loading is based on the mission profile data for a STOL type advanced transport airplane (Reference 30). The flight noise level is calculated using the fifth power law of the relative jet exhaust velocity and a tradeoff procedure based on crack propagation data in Reference 16.

In Reference 16 a relationship between the crack growth rate and the rms stress intensity factor is established for a panel with an edge crack subjected to random acoustic excitation. Since the acoustic level is proportional to the panel rms stress and therefore to the rms stress intensity factor, the ratio of the durations,  $t_1$  and  $t_2$ , of equal crack growth, at the corresponding excitation levels,  $G_{01}$  and  $G_{02}$  (in dB/Hz.) is given by

$$\frac{t_2}{t_1} = 10^{0.2(G_{02} - G_{01})} \quad 41$$

Based on the use of the above equation together with the flight utilization data, the equivalent total flight duration of 130 hours is obtained for the 40,250 flights at a spectrum level of 139 dB. The 130 hours represents a duration of 11.6 seconds per flight. Since the combined ground and flight portions have to be contained within 28 seconds per flight, the duration of the flight portion is reduced to 10 seconds for the flight acoustic load representation in this program.

The use of the accelerated flight spectrum level of 139 dB for simulating the flight noise environment essentially assumes that no interaction effects on crack growth are obtained from the combined acoustic and flight loads. The benefits of a constant flight and takeoff acoustic load spectrum which include reduced flight time, ease of data interpretation, and simplified acoustic load simulation outweigh the above limitation.

#### 4. Load Tapes

##### 4.1 Flight-by-Flight

The flight-by-flight load tapes for controlling the MTS fatigue machines are generated by a hybrid computer program based on the load histories developed in Section III2. The randomization of the loads is carried out within the computer program. Each cycle of the randomization load is represented by a sinewave.

The complex nature of the combined flight-by-flight and acoustic loads required the use of a step-by-step process for the application of the combined loads. Three flight-by-flight load tapes of increasing complexity have been developed for use in conjunction with the acoustic loading for each set of the upper and lower wing surface loads. The first load tape contains the spectral load time history, the second tape contains flight-by-flight loads but with the duration of the compression load reduced to a minimum, and the third tape contains the full flight-by-flight load time history. The sequence and level of each load peak is identical within each set of the three tapes. Representative sections of the three load tapes are illustrated in Figures 15 and 16 for the upper and lower wing surface loads, respectively.

Each load tape contains load calibration signal pulses for counting flights and two identical load tracks for comparison purposes as a safe-guard against spurious load pick-up by the MTS fatigue machines.

##### 4.2 Acoustic

The acoustic loading is recorded on one inch wide magnetic tape for reproduction by an Ampex tape recorder that feeds the signal directly to the shaker amplifier independent of the MTS fatigue machine tape deck. The random acoustic loading is generated by analogue equipment consisting of a Brüel and Kjaer (B&K) random noise generator, a  $3\sigma$  signal peak clipper to prevent shaker overload shut down, a 2 Hz bandwidth filter with a 63 Hz center frequency to simulate a single degree of freedom system response, and an attenuator to reduce the signal to a level acceptable to the tape recorder. This method of generating the acoustic loading is necessitated by the very high internal damping of the shaker which eliminates the panel resonance peak as encountered in the test program. The resulting signal history is typical of a narrow band random load history, with an appearance of a randomly modulated sinewave.

TAPE GA1  
SPECTRAL  
TIME  
HISTORY

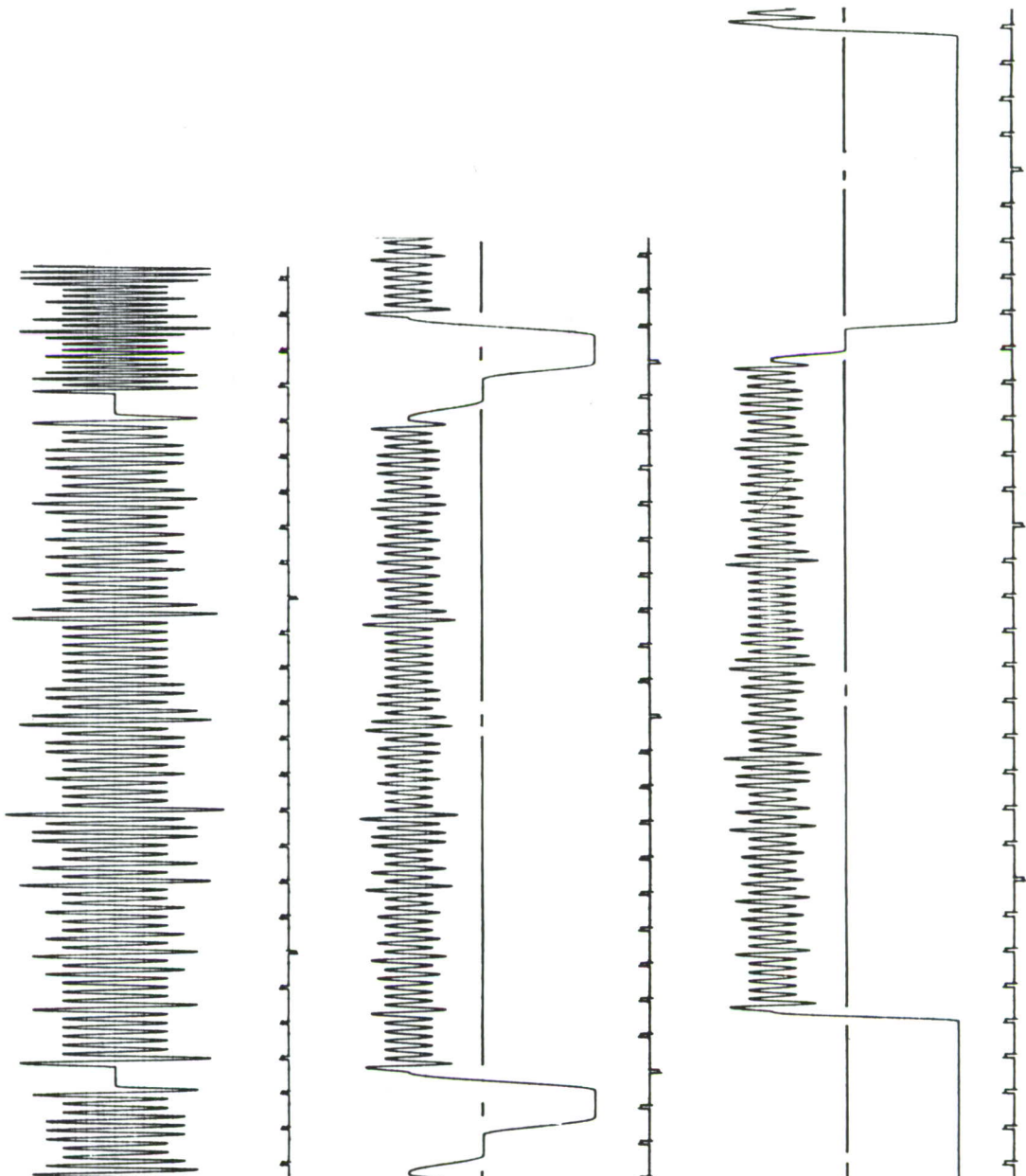


FIGURE 15. TYPICAL SECTION OF UPPER WING LOAD TIME HISTORY

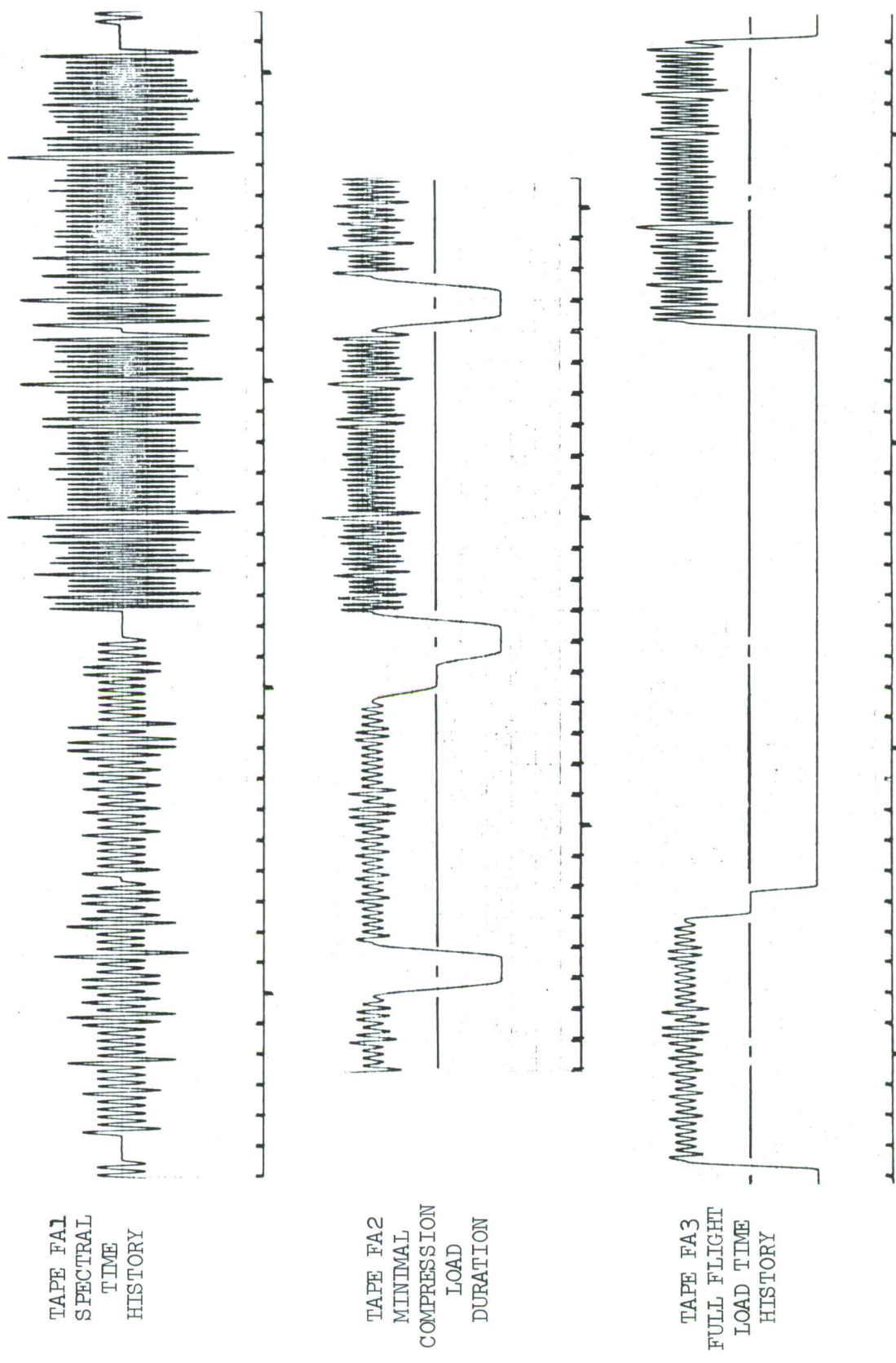


FIGURE 16. TYPICAL SECTION OF LOWER WING LOAD TIME HISTORY

## IV CRACK GROWTH THEORY

### 1. Introduction

The analysis and, ultimately, the prediction of the rate and path of crack growth due to realistic loading conditions are of great importance to the study of failure in aircraft structures. Analysis methods have been developed to predict the crack growth due to flight-by-flight loads. As the problem of combined acoustic and flight loads has not previously been investigated, no theory has been developed which predicts the effect of combined acoustic and flight loads on crack growth.

In the absence of a suitable combined load theory, it is necessary to determine if existing analysis methods can be used to predict the crack growth under combined acoustic and flight loads, and if not, to indicate the direction of future development. Accordingly, the existing analysis methods pertaining to the prediction of crack growth due to flight loads and acoustic loads are summarized. Equations used in the subsequent crack growth analysis are identified.

### 2. Flight-by-Flight Load Analysis

The programmed crack orientation employed in all the combined load tests performed in this study is in the most critical direction for the flight loads because it is hypothesized that the crack will be originated by the flight-by-flight loads. Consequently, the flight-by-flight analysis becomes more significant. Any significant interaction effects between the acoustic and the flight load induced panel stresses on the crack growth may be indicated by deviations from the theoretically predicted data beyond normal experimental scatter common to flight load crack growth data.

#### 2.1 Crack Growth Laws

Numerous publications on the subject have proposed various crack growth laws based on physical models, dimensional considerations, and empirical observations. References 31 and 32 offer a detailed review of the subject.

Based on the elastic fracture mechanics approach, the stress intensity factor,  $K$ , is regarded as the critical parameter controlling the mechanism of crack propagation. Of the various relationships which define the rate of crack growth as a function of the stress intensity factor, the following crack growth laws are the most popular:

$$\frac{da}{dN} = f(\Delta K) \quad \text{Paris} \quad 42$$

$$\frac{da}{dN} = f \left[ \frac{(\Delta K)^{\beta}}{K_c - K_{\max}} \right] \quad \text{Forman} \quad 43$$

$$\frac{da}{dN} = f \left[ K_{max}^{(1-\beta)} (\Delta K)^\beta \right] \text{ Walker, Erdogan} \quad 44$$

where  $da/dN$  is the crack growth rate,  $\Delta K$  is the change in stress intensity factor of the load cycle,  $K_c$  is the plane stress fracture toughness,  $K_{max}$  is the maximum stress intensity factor of the load cycle,  $\beta$  is an empirical constant, and  $f$  indicates some monotonically increasing function. Often  $da/dN$  data is accurately fitted by a log-log straight line. Accordingly, equation 44, for example, takes the form

$$\frac{da}{dN} = C_w \left[ (1 - R)^m K_{max} \right]^n \quad 44(a)$$

where  $C_w$  and  $n$  are empirical constants and  $R$  is the stress range ratio (minimum tensile stress divided by maximum tensile stress).

The crack growth laws listed above or their variations have been used with reasonable success when employed to describe crack growth behavior of different materials under constant amplitude load cycles. If, however, the load is of arbitrary varying amplitude, a linear cumulative growth approach is often found to be conservative.

## 2.2 Crack Growth Retardation Models

The phenomenon of crack growth retardation has been studied since the early 1960's and Reference 7 offers a significant insight into the subject. The retardation model introduced in Reference 7 is often referred to as the "Wheeler Model".

Wheeler's model for crack growth retardation suggests the utilization of a reduction factor, following a high peak load, on the subsequent constant amplitude crack growth rate. The model can be described as,

$$\frac{da}{dN} = C_p f \left[ \Delta K, K_{max} \right] \quad 45$$

where  $C_p$ , the retardation parameter, is given by

$$C_p = \left[ \frac{r_p}{(r_{ep})_j} \right]^m \quad 46$$

and

$$(r_{ep})_j = \text{MAX} \left[ (r_{ep})_{j-1} - (\Delta a)_{j-1}, (r_p)_j \right] \quad 47$$

In the above equations,  $m$  is an empirical constant and  $(r_{ep})_j$  is the distance from the crack tip to the elastic-plastic interface during the  $j$ th cycle after the application of a high load. The parameter  $r_p$  is the radius of the plastic zone and is proportional to the square of the ratio of stress intensity to tensile yield stress.

$$r_p = C \left( \frac{K}{\sigma_{ys}} \right)^2 \quad 48$$

The retardation parameter,  $C_p$ , calculated using equation 46 accounts for the retardation effect  $N$  cycles after a high load is applied.

In a modification to the Wheeler model, proposed in Reference 33, the crack growth rate due to spectrum loading is expressed in terms of the effective stress intensity range,  $\Delta K_{eff}$ , by:

$$\frac{da}{dN} = C \left[ \Delta K_{eff} \right]^n \quad 49$$

where

$$\Delta K_{eff} = \left[ \frac{\frac{K_{max}}{*}}{K_{max}} \right]^{\frac{2m}{n}} f(\Delta K, R), \text{ for } K_{max} < K_{max}^* \quad 50$$

$$= f(\Delta K, R), \text{ for } K_{max} \geq K_{max}^*$$

$$K_{max}^* = K_{max}^{OL} \left[ 1 - \frac{\sum \Delta a}{(r_p)_{OL}} \right]^{1/2} \quad 51$$

and  $K_{max}^{OL}$  is the maximum stress intensity factor due to the overload,  $(r_p)_{OL}$  is the plastic yield zone size due to the overload, and  $\sum \Delta a$  is the sum of crack growth since the overload. In addition, the coefficient  $m$  in equation 50 is related to the threshold stress intensity factor (Reference 33) by

$$m = \frac{n}{2} \frac{\log \left[ \frac{f(\Delta K, R)}{g \left( \Delta K_{th} \Big|_{R=0}, R \right)} \right]}{\log S} \quad 52$$

where  $g(\Delta K_{th}|_{R=0}, R)$  is the function used in defining the threshold stress intensity factor,

$$\Delta K_{th} = g\left(\Delta K_{th}|_{R=0}, R\right) \quad 53$$

and  $S$  is approximately equal to 2.3 for 2024-T3 aluminum and equal to 2.8 for Ti-6Al-4V.

Another retardation model, proposed by Willenborg, et al, Reference 8, is based on the approach of an effective stress intensity factor and can be expressed as,

$$\frac{da}{dN} = f\left[\left(\frac{K_{min}}{K_{max}}\right)_{eff}, \left(\frac{K_{max}}{K_{min}}\right)_{eff}\right] \quad 54$$

$$\left(\frac{K_{max}}{K_{min}}\right)_{eff} = \text{MAX} \left\{ 0, K_{max} - K_{max} \left[ \left( \frac{r_{ep}}{r_p} \right)_{j}^{1/2} - 1 \right] \right\} \quad 55$$

$$\left(\frac{K_{min}}{K_{max}}\right)_{eff} = \text{MAX} \left\{ 0, K_{min} - K_{min} \left[ \left( \frac{r_{ep}}{r_p} \right)_{j}^{1/2} - 1 \right] \right\} \quad 56$$

For spectrum loading in the Willenborg model, the crack growth retardation is expressed in terms of a stress reduction,  $\sigma_{red}$ . For the  $j$ th cycle in a load sequence

$$\left(\sigma_{red}\right)_j = \left(\sigma_{max}\right)_j \left[ \left( \frac{r_{ep}}{r_p} \right)_{j}^{1/2} - 1 \right] \quad 57$$

In equation 57, both  $r_{ep}$  and  $r_p$  are computed for the current  $j$ th cycle. The maximum and the minimum stresses for the  $j$ th cycle  $(\sigma_{max})_j$  and  $(\sigma_{min})_j$  are then reduced by the amount  $(\sigma_{red})_j$  to the respective effective values,  $(\sigma_{max})_{j,eff}$  and  $(\sigma_{min})_{j,eff}$ . These effective stress levels are then used together with appropriate crack growth rate curves to estimate crack growth due to the  $j$ th cycle. By this means the Willenborg model becomes much simpler to use than the Wheeler model.

For flights with a large number of cycles, where it is difficult to calculate the effect of retardation cycle-by-cycle, the retardation effect can be approximated by assuming a constant  $r_{ep}$  caused by the highest cyclic load.

This approximation results in a slight overestimate of  $\sigma_{red}$  and, consequently, an overestimation of the retardation effect. In other words, a lower bound of the crack growth rate is obtained using this assumption. Since the crack growth rate calculated with no retardation provides a corresponding upper bound, a reasonable estimate of the crack growth behavior can be obtained without an extensive analysis effort.

Using the constant elastic-plastic interface assumption and selecting the elastic-plastic zone size produced by the highest stress,  $\sigma_{max}$ , in the entire load spectrum to be the constant  $r_{ep}$  value, equation 53 can be rewritten as,

$$(\sigma_{red})_j = (\sigma_{max})_j \left\{ \left[ \frac{\sigma_{max}}{(\sigma_{max})_j} \right] - 1 \right\} \quad 58$$

$$(\sigma_{max})_j^{eff} = \text{MAX} \left[ 2(\sigma_{max})_j - \sigma_{max}, 0 \right] \quad 59$$

$$(\sigma_{min})_j^{eff} = \text{MAX} \left[ (\sigma_{max})_j + (\sigma_{min})_j - \sigma_{max}, 0 \right] \quad 60$$

where the function MAX (x,y) takes the value of the largest of its arguments.

### 2.3 Stress Intensity Factor for Open Hole

The initial crack in this study is programmed into a rivet hole. Consequently, the stress intensity formula for an open hole, given in Reference 34, is modified for an assumed close-fit hole as discussed in Reference 10. The resulting Mode I stress intensity factor is given by:

$$K_I = \sigma \left[ \pi a \right]^{\frac{1}{2}} F_o \left[ \frac{a}{r+a} \right] \quad 63$$

where  $r$  is the hole radius,  $a$  is the crack length, and

$$F_o \left[ \frac{a}{r+a} \right] \cong 3.365^{-m\eta} \quad 64$$

with  $m = 1.85$  and  $\eta = \frac{a}{r+a}$ ,

$$\text{or } F_o(\eta) = \exp (1.2133 - 2.205\eta + 0.6451\eta^2) \quad 65$$

## 2.4 Crack Growth Calculation

The procedure for calculating the crack growth due to flight loads involves the computation of the modified stress intensity factor (equations 63 to 65) corresponding to the minimum and maximum stress in each load cycle. The corresponding maximum and minimum stress intensity factors are, thereafter, substituted into equation 44(a) to obtain the crack growth rate and by summation, the crack growth. With crack retardation included, the maximum and minimum flight load stresses are replaced in the above analyses by the effective maximum and minimum stresses given by equations 59 and 60 for the simplified Willenborg retardation model. This procedure for calculating the crack growth has been computerized employing an integration procedure (Reference 36) in place of the cycle-by-cycle summation to speed up the computation.

The simplified Willenborg retardation model is used in this program because of its ease in use and acceptable accuracy as verified later in this report. The baseline crack growth data, used in conjunction with equation 44(a), is obtained from Reference 35 for the 7075-T6 alloy used in this program.

The maximum and minimum flight load stresses and the number of flight cycles at each stress level of the flight load spectra developed in section III2 and used in the analysis are summarized in Tables 9 and 10 for the lower and upper wing surfaces, respectively. The corresponding effective maximum and minimum stress levels due to retardation are included in the above tables.

This analysis indicated a slower than planned crack growth time for a desired crack growth of approximately 0.8 inches. Subsequent analysis indicated that a 60 percent increase in the stress level is required in order to complete tests within a reasonable time period. A comparison of the original stress levels and the stress levels used in the test program, together with the corresponding MTS fatigue machine load levels, are summarized in Tables 11 and 12 for the lower and upper wing surfaces, respectively. The test specimen cross sectional area of 1.433 square inches is used in converting the panel stresses into the fatigue machine loads.

The crack growth predictions corresponding to the increased load levels are discussed and presented in Section VI, Correlation and Evaluation.

## 3. Acoustic Load Analysis

The sonic fatigue cracks generally occur along the rivet line or the stiffener edge initiating at the center of the longest panel side. This location corresponds to the peak bending stress region in the fundamental mode. During the initial crack propagation, the crack edge is effectively simply supported, held in place by the rough crack surface. After some time when the rough crack surface is ground smooth by the continual

TABLE 9. STRESS LEVELS FOR THE LOWER WING SURFACE SPECTRUM

Level	$\sigma_{\max}$ , PSI	$\sigma_{\min}$ , PSI	$(\sigma_{\max})^{\text{eff}}$ , PSI	$(\sigma_{\min})^{\text{eff}}$ , PSI	No. of Cycles
1	12880	1924	12760	1804	72
2	12280	2516	11560	1796	78
3	11690	3108	10380	1798	150
4	11250	3552	9500	1802	300
5	10950	3848	8900	1798	400
6	10660	4144	8320	1804	800
7	10060	4736	7120	1796	1800
8	13000	(-7500)	13000	0	72
9	12580	2220	12160	1800	7
10	12140	2664	11280	1804	8
11	11690	3108	10380	1798	20
12	111100	3700	9200	1800	35
13	10660	4144	8320	1804	70
14	10060	4736	7120	1796	310
15	9320	5476	5640	1796	950
16	8580	6216	4160	1796	2100
17	13000	(-7500)	13000	0	112

NOTE: The above spectrum includes:

- (1) 18 low level missions - 72 flights
- (2) 56 typical missions - 112 flights
- (3) 184 G-A-G cycles

TABLE 10. STRESS LEVELS FOR THE UPPER WING SURFACE SPECTRUM

Level	$\sigma_{\max}$ , PSI	$\sigma_{\min}$ , PSI	$(\sigma_{\max})^{\text{eff}}$ , PSI	$(\sigma_{\min})^{\text{eff}}$ , PSI	No. of Cycles
1	8900	1100	8900	1100	23
2	8700	1300	8500	1100	23
3	8500	1500	8100	1100	46
4	8300	1700	7700	1100	138
5	8100	1900	7300	1100	161
6	7900	2100	6900	1100	598
7	7500	2500	6100	1100	1978
8	7100	2900	5300	1100	3956
9	6600	3400	4300	1100	9568
10	8900	(-7500)	8900	0	23
11	8700	(-7500)	8500	0	23
12	8500	(-7500)	8100	0	46
13	8300	(-7500)	7700	0	92

NOTE: The above spectrum includes: (1) 184 taxi segments  
 (2) 184 G-A-G cycles

TABLE 11. LOWER WING TEST LOAD AND PANEL STRESS DATA

Type of Load	Original Levels		Final Test Levels	
	Stress, PSI	Load, Pound	Stress, PSI	Load, Pound
Mean Tension	7400	10610	12230	17520
Maximum Varying	5480	7850	9050	12970
Mean + Maximum Varying	12880	18460	21280	30490
Compression	7500	10750	7500	10750

TABLE 12. UPPER WING TEST LOAD AND PANEL STRESS DATA

Type of Load	Original Levels		Final Test Levels	
	Stress, PSI	Load, Pound	Stress, PSI	Load, Pound
Mean Tension	5000	7170	8000	11460
Maximum Varying	3900	5590	6240	8940
Mean + Maximum Varying	8900	12760	14240	20400
Compression	7500	10750	7500	10750

vibration, the crack edge becomes free and the crack will turn at both ends into the panel. For long panel edge cracks, relative to the panel length, the crack will grow into the panel in a direction normal to the panel edge.

With progressive wave type acoustic excitation parallel to the long panel edge significant stresses can be obtained in both the fundamental and the (2,1) mode which will affect the crack growth rate.

Both the crack edge condition and the two mode panel response are included in the analysis method presented in Reference 16 for predicting panel edge crack growth due to acoustic loading.

### 3.1 Discussion of Analysis Method

The basic analysis method is developed for a fixed-fixed type panel with an edge crack positioned at the center of the longest panel edge. Composite static beam type mode shapes are used to represent the cracked panel deflection in the extended Rayleigh Ritz analysis to determine the variation of both the panel frequency and the corresponding composite mode shapes with crack growth.

Expressions relating the crack tip stress intensity factor to the displacement at a modal displacement reference point are developed from the composite mode shapes. For the simply supported crack edge, the crack opening mode, Mode I, is considered to be dominant. The Mode I stress intensity factor for a simply supported crack of length  $2a$  in the boundary between a flexible panel and a rigid structure was derived and given by

$$K = 0.8 \sigma \sqrt{\pi a} \quad 66$$

where  $\sigma$  is the panel edge cylindrical bending stress remote from the crack tip. For a panel, the stress,  $\sigma$ , is replaced by the nominal crack tip bending stress,  $\sigma_{ye}$ , as determined by the Rayleigh Ritz analysis.

Random response theory, similar to equations 17 through 20 but in terms of displacement instead of strain, is used together with the predicted two modal frequencies and the corresponding cracked panel mode shapes to obtain the rms displacements at the modal reference points and, therefore, the corresponding rms stress intensity factor,  $\bar{K}$ . The appropriate material random reverse bending crack growth data in form of the crack growth rate equation

$$\frac{da}{dN} = \bar{C} \bar{K}^n \quad 67$$

which is used together with the rms stress intensity factor to predict crack growth by means of numerical integration.  $\bar{C}$  and  $n$  are empirically determined material constants.

The above analysis is very involved and requires extensive computation.

Consequently, a simplified crack propagation analysis procedure is suggested in Reference 16 based on the results of the more involved analysis.

### 3.2 Simplified Analysis Procedure

The method assumes that the panel has significant response only in the fundamental mode, which is a commonly used assumption in sonic fatigue analysis. The crack edge is also assumed to be simply supported. The analysis procedure is as follows:

- a. Compute the maximum panel edge rms stress,  $\bar{\sigma}_{ye}$ , in the uncracked panel using the procedure described in Reference 18.
- b. For a crack length to panel length ratio  $B$ , the crack tip bending rms stress will be approximated by  $\bar{\sigma}_{ye}(1-B^2)^2$  and the corresponding rms crack tip stress intensity factor  $\bar{K}$  given by

$$\bar{K} = 0.8 \bar{\sigma}_{ye}(1-B^2)^2 \sqrt{\pi a} \quad 68$$

where  $a$  is the half crack length.

- c. Equation 68 can be used in the appropriate material crack growth equation given by equation 67, resulting in

$$\frac{da}{dN} = \bar{C} [0.8 \bar{\sigma}_{ye}(1-B^2)^2 \sqrt{\pi a}]^n \quad 69$$

- d. The crack growth per stress reversal is converted to the crack growth per unit time by the use of the fundamental panel frequency for the uncracked panel. The cracked panel frequency remains fairly constant for a value of  $B$  up to about 0.4.
- e. The time taken for the crack to grow from the flaw size to any crack length up to 40 percent of the panel length, can be determined by numerical integration.

The above procedure is satisfactory for a value of  $B$  up to about 0.4.

### 3.3 Crack Growth Calculation

The basic random crack growth data for reverse bending (equation 67) is not available for the 7075-T6 material. However, such data can be generated from extensional constant amplitude crack growth data by the use of the relationship between extensional and bending crack growth data developed in Reference 37, the Rayleigh distribution of stress peaks, and linear summation (Miner's Rule) as described in Reference 16. The resulting random crack growth data over-estimates the measured crack growth data. Better correlation with the measured data is obtained in Reference 16 by the inclusion of the crack closure effect (Reference 38) in the analysis.

The constant amplitude reverse bending crack growth data was found, in Reference 16, to be highly dependent on the loading frequency, differing by as much as a factor of 3 between 4 Hz and 175 Hz. This frequency dependence requires, by implication, extensional data of the appropriate frequency to be developed in order to obtain the corresponding random data by the above procedure. Also, the expression for the panel edge crack stress intensity factor (equation 66) may not be valid for riveted panels where the peak bending stresses alternate between the rivet line and the frame edge during each stress reversal.

Due to the many sources of potential error described above, generation of random reverse bending data using the procedure in Reference 16 is not justified. Existing random crack growth data can be used to provide the indication as to the crack growth rate for the 7075-T6 alloy. The L71 alloy used in the crack growth studies in Reference 16 is similar in composition and crack growth characteristics to the 2024-T4 alloy, which, in turn, has a lower crack growth rate than the 7075-T6 alloy. The lower loading frequency of 63 Hz in this program, as opposed to 175 Hz used in Reference 16, should further increase the crack growth rate in the test panels. Assuming that the expression for the edge crack stress intensity factor (equation 66) is also valid for skin stiffener type structures, the random crack growth data in Reference 16 should represent a lower bound for the expected crack growth from the acoustic type crack in Figure 12. The random crack growth data indicates that no crack growth due to acoustic loading can be expected from the flight load crack due to its small width, which can be considered as an approximation of the effective crack length for the acoustic loading.

## V TEST PROGRAM

### 1. Introduction

The objectives of the test program are to:

- o demonstrate the degree of correlation achieved in the panel response from acoustic and electromagnetic shaker excitation,
- o correlate the shaker excitation levels with the acoustic excitation levels,
- o determine the extent to which the combination of acoustic loads with flight loads affects crack growth, and
- o obtain data to evaluate current crack growth analysis methods.

A two phase test program is used to accomplish the above objectives. The first phase involves the demonstration of the degree of correlation achieved between the shaker and acoustic excitation, culminating in a calibration curve between the acoustic and shaker load levels. An acoustic progressive wave tunnel, a flexibly mounted electromagnetic shaker, and a single test panel are employed in this phase of the program.

The second phase represents the main test effort involving the generation of crack growth data from the various acoustic and flight load combinations to isolate any effects on crack growth. Two MTS fatigue machines together with two flexibly mounted electromagnetic shakers are used to apply the prescribed load successively to a total of twelve test specimens.

### 2. Calibration Tests

The crack growth rate due to acoustic loading is proportional to the rms stress (Reference 16) in the region of the crack. The calibration between the acoustic and shaker loading is consequently obtained on the basis of equal rms panel stress at the appropriate location on the test panel. Panel edge cracks are used in the second phase of the test program. It is, therefore, necessary to determine the panel stress distribution in this region as a function of both the shaker and acoustic loading. The rms panel stress is also a function of the panel frequency and damping which are, consequently, of interest.

#### 2.1 Instrumentation

Six 120 ohm strain gages and one B&K type 8200 force gage are attached to the acoustic calibration test panel. The strain gage locations are illustrated in Figure 17. The B&K type 8200 force gage is attached to the center of the panel. Two half-inch Dynagage type 524 microphones are mounted flush with the interior wall of the progressive wave tunnel, one opposite the center of the test panel and the other, which is used as a reference microphone,

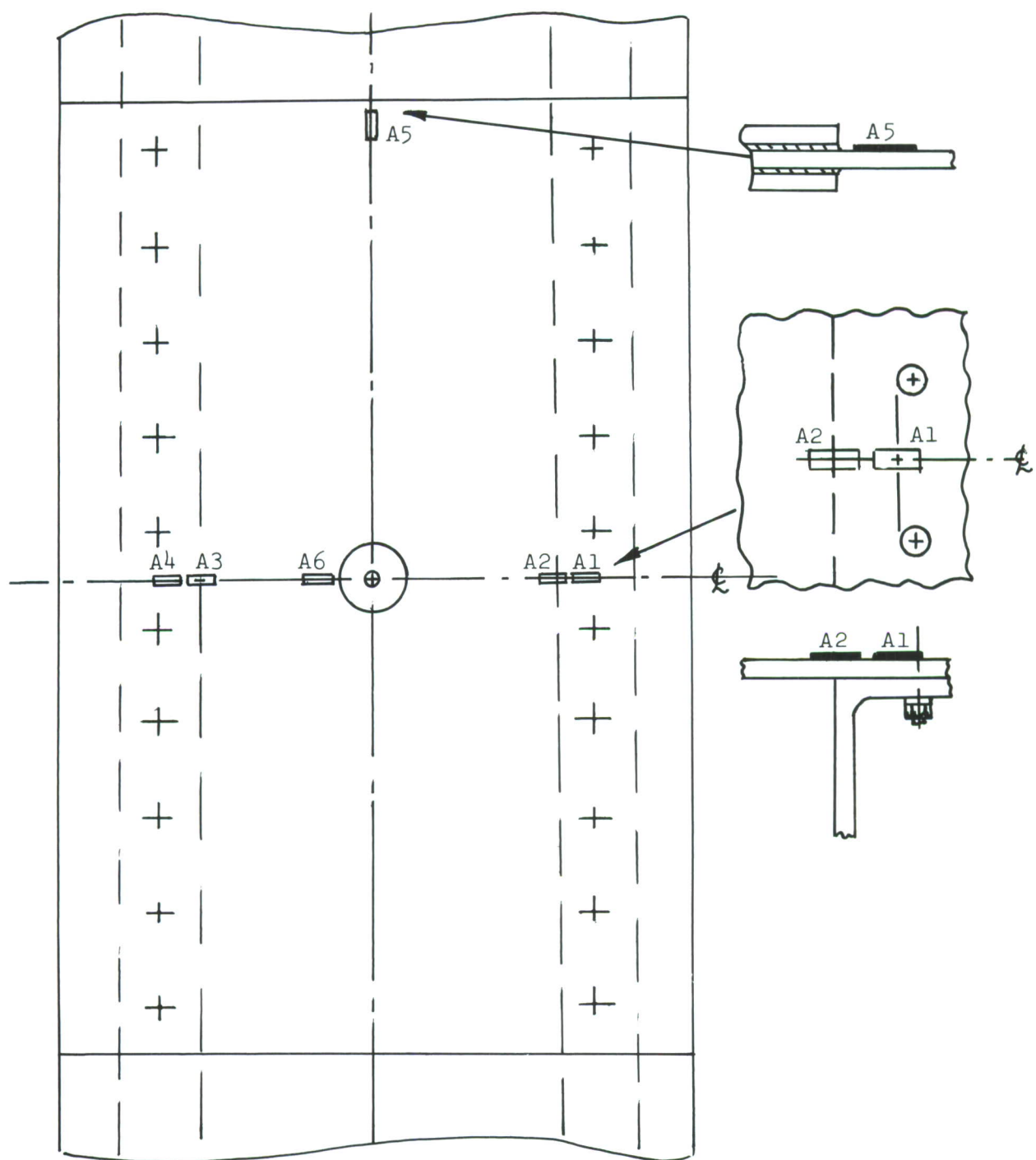


FIGURE 17. CALIBRATION PANEL STRAIN GAGE LOCATIONS

in an upstream location.

The microphones are calibrated prior to the test with a Photocon PC-125 calibrator at 140 dB and 1000 Hz frequency. The force gage is calibrated by loading the force gage with a known weight. The strain gage and amplifier circuits are calibrated by unbalancing the bridge with a high precision resistor built into the bridge circuit.

## 2.2 Test Set-Up

The acoustic progressive wave tunnel with a NORAIR MK VII noise generator and the electromagnetic shaker mounting are illustrated in Figure 18. The shaker is suspended by four turnbuckles which are used to adjust its position relative to the panel center. The shaker is stabilized by two 0.063-inch thick aluminum flexures attached at one end to the bottom of the shaker and at the other end to a channel frame welded to the progressive wave tunnel. The flexures and turnbuckles in combination with the shaker weight permit shaker motion only normal to the panel surface, thereby preventing excessive moments from being applied to the force gage. This arrangement enables the full shaker force to be realized at the panel provided that the shaker drive rod resonant frequency is considerably greater than that of the panel.

Details of the acoustic calibration test panel, the panel fixture, the force gage position and the shaker drive rod are illustrated in Figure 19. Both steel and aluminum 1/4-inch thick end plates are used to bolt the test panel and the frames at each end to a stack of three one-inch thick plywood boards. The center section is cut out of the plywood boards to accommodate the length of the frames and to just clear the panel sides. This method of panel attachment provides a good simulation of the structural attachment used later on in the program. The plywood boards are bolted together and held in the progressive wave tunnel aperture by cantilevered block and threaded rod type clamps.

## 2.3 Test Procedure, Data Analysis and Results

The data needed to develop a calibration of the shaker and acoustic excitation is obtained from several different tests involving the shaker/panel combination. These tests involve calibration of the progressive wave tunnel, panel damping and frequency, panel response to shaker excitation, and panel response to acoustic excitation.

2.3.1 Progressive Wave Tunnel Calibration - Prior to the installation of the test panel, the progressive wave tunnel is calibrated with the test aperture blocked by a concrete plug to obtain the correct tunnel sound pressure levels. The noise spectrum is shaped to provide a constant spectrum level, in the frequency band of 50 Hz to 200 Hz, at the center of the test section. The sound pressure level is measured using the two flush mounted microphones.

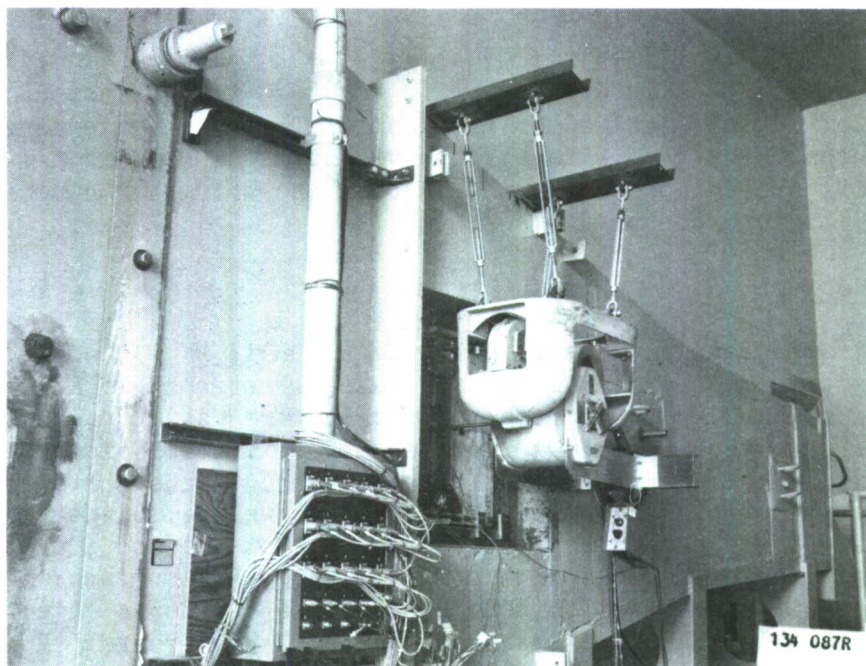


FIGURE 18. SHAKER AND SPECIMEN MOUNTING ON PROGRESSIVE WAVE TUNNEL

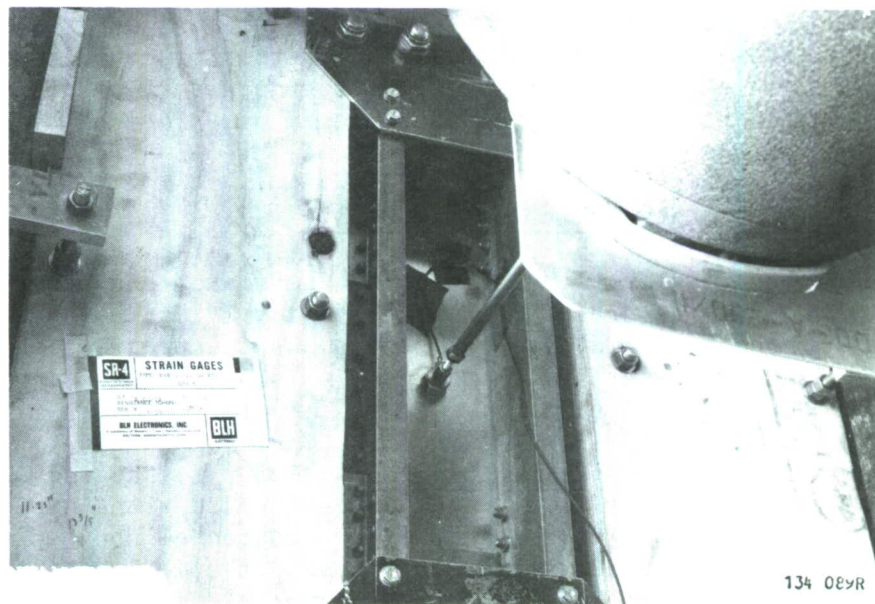


FIGURE 19. SHAKER/PANEL DRIVING ROD AND FORCE GAGE DETAIL

The upstream reference microphone, which is less susceptible to panel acoustic radiation effects, is used to monitor the sound pressure level in the subsequent panel response tests.

The data is analyzed using the Hewlett-Packard Model 8054A third octave real time analyzer together with the B&K type 2416 rms voltmeter to obtain third octave sound pressure levels and the overall sound pressure level. Typical spectrum level plots obtained from the third octave data are illustrated in Figure 20 for both microphone locations.

**2.3.2 Panel Damping and Frequency** - The damping tests are performed with the test panel installed in the progressive wave tunnel and with the shaker attached to the test panel. The panel is excited by tapping the shaker coil when the power to the shaker is switched, in turn, both on and off to produce a free decay of the panel response. The free decay as measured by the strain gages, is recorded on magnetic tape and fed into the Central Data System Xerox 5 computer for both a quick look on the cathode ray tube (CRT) display and hard copies of the data. Typical free decays are illustrated in Figure 21 with the shaker power switched on and in Figure 22 with the shaker power switched off.

The panel viscous damping coefficient is obtained from the log-decrement of the decay. The measured viscous damping coefficients for the panel fundamental mode are approximately 0.4 and 0.0095 for the shaker power on and off conditions, respectively. The corresponding panel fundamental frequency obtained by a cycle count of the free decay is approximately 70.4 Hz.

**2.3.3 Panel Response to Shaker Excitation** - A constant amplitude sinusoidal frequency sweep of the test specimen is initially performed using a Spectral Dynamics SD 104A sweep oscillator with a SD 105A servo control. The sweep produced a near flat panel response indicating the presence of high panel damping.

To overcome the problem of high panel damping, the narrowest available filter (Spectral Dynamics SD 101A tracking filter) with a 2 Hz 3 dB bandwidth is used together with a B&K type 1024 random noise generator, a  $3\sigma$  signal clipper and a signal attenuator to generate the force signal to drive the panel. The filter center frequency is set at 63 Hz.

The test panel is excited first with discrete frequency and then with the narrowband random force, described above, at typically four to five shaker rms force levels. The shaker rms force and the corresponding strain levels are measured in turn with an rms meter (TSI model 1060) using typically 100 seconds averaging time for the random data and the minimum time for the sinusoidal data. A dual beam storage oscilloscope (Tektronics 564) is used to monitor the test and in the capture mode, in conjunction with the rms voltmeter, to ensure that the  $3\sigma$  peak clipper is functioning properly. The measured panel edge rms strains are illustrated in Figure 23 as a function of the rms force for both the sinusoidal and narrow band random force excitation.

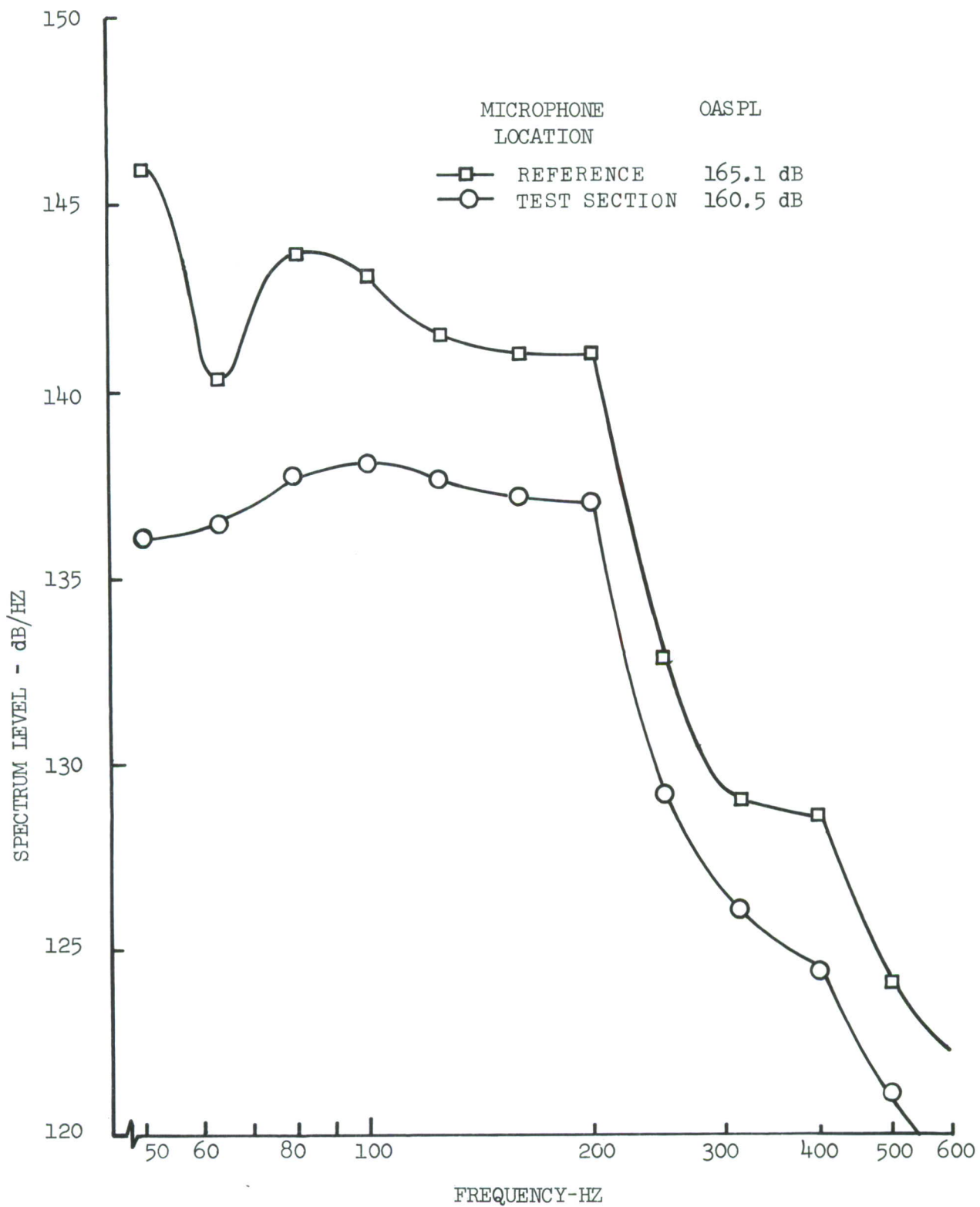


FIGURE 20. TYPICAL TUNNEL SOUND PRESSURE LEVELS FROM 1/3 OCTAVE MEASUREMENTS

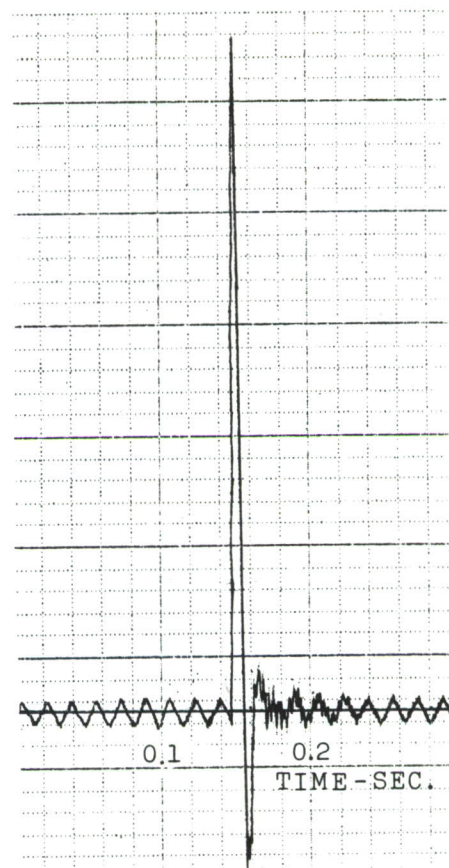


FIGURE 21. PANEL FREE DECAY WITH SHAKER POWER ON

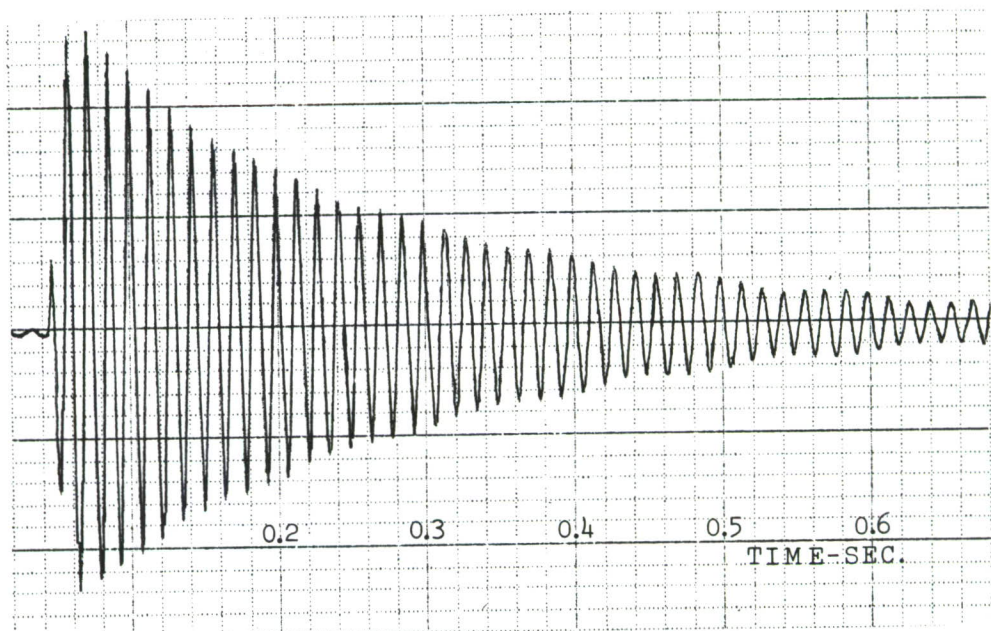


FIGURE 22. PANEL FREE DECAY WITH SHAKER POWER OFF

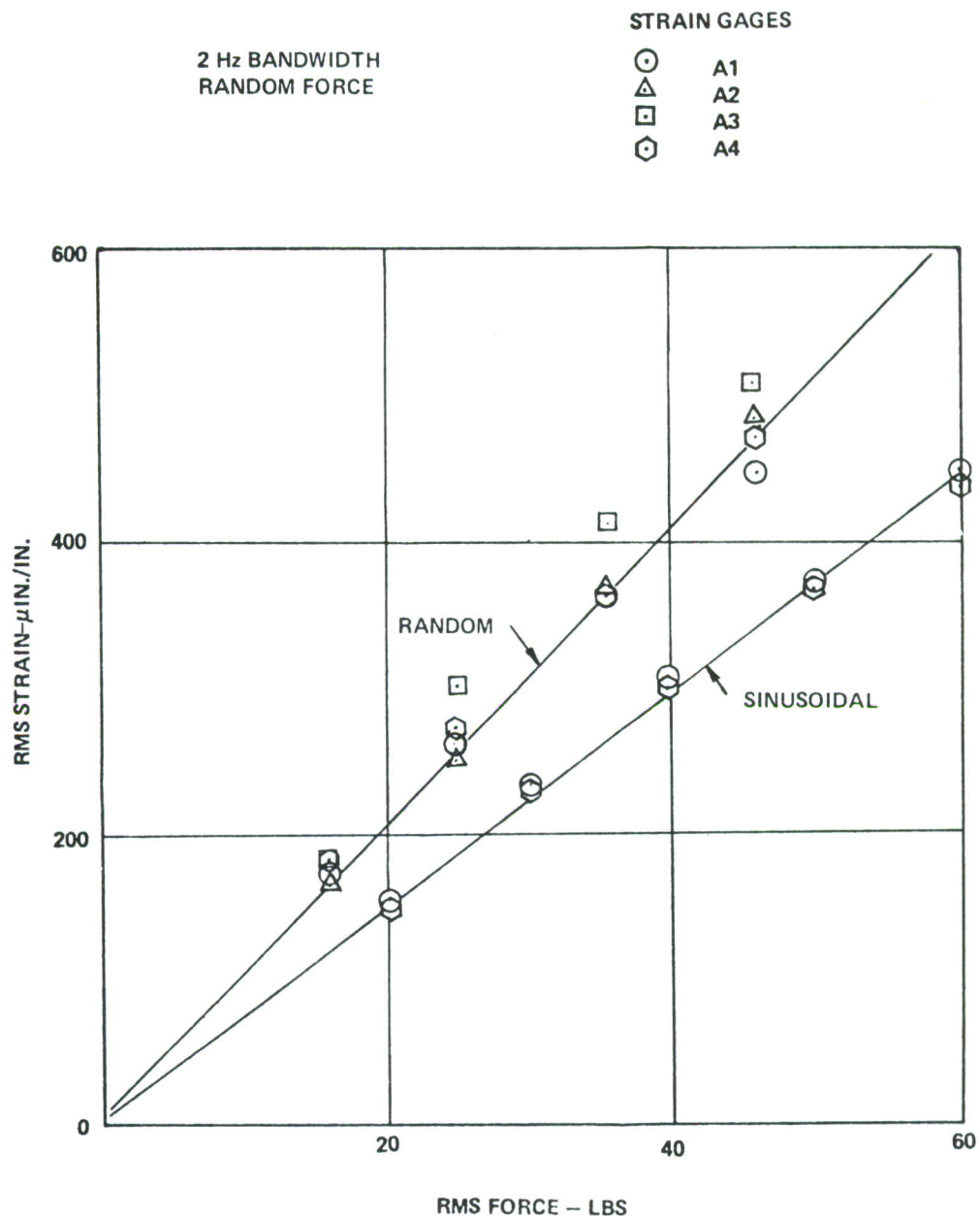


FIGURE 23. PANEL EDGE STRAIN AS A FUNCTION OF SHAKER FORCE

The random force and strain data is recorded on magnetic tape using a Sangamo 3568 fourteen channel tape recorder. The force signal is also recorded on magnetic tape, using an Ampex FR 1300 tape recorder, for use in phase 2 tests. Narrow band analysis of the random force and strain data, on magnetic tape, is conducted using a Spectral Dynamics SD 301 Real Time Analyzer in conjunction with the SD 302 Ensemble Averager and a CRT display. The analyzer is connected to the Central Data System Xerox 5 computer for scaling purposes and obtaining hard copies of the data. Typical narrow band analysis of the shaker force (35 pounds rms) and the corresponding panel edge strain (strain gage A1) are illustrated in Figures 24 and 25, respectively.

Peak and valley probability density distributions are obtained from the tape recorded panel strain data using a peak and valley count routine available on the Xerox 5 computer. Typical panel edge strain (strain gages A1 and A2) peak and valley probability density distributions with shaker excitation are illustrated in Figure 26.

**2.3.4 Panel Response to Acoustic Excitation** - The shaker power is switched off for this test. The random signal from the B&K random noise generator is fed through the General Radio type 1925 adjustable level third octave filters, to shape the spectrum, and through the power amplifier to the NORAIR MK VII noise generator. The sound pressure level in the progressive wave tunnel is measured at the upstream reference location using a half-inch Dynagage type 524 microphone. The overall noise level is measured with the B&K type 2416 rms voltmeter and the third octave levels are measured with the Spectral Dynamics real time analyzer. Four random noise excitation levels, at each of three excitation bandwidths of 10, 50 and 100 Hz, are used in the test. The 10 and 50 Hz bandwidths are centered at 70 Hz. The 150 Hz bandwidth lower and upper limits are set at 50 and 200 Hz, respectively.

The signals from the six strain gages and the force gage are fed through their respective conditioning systems and amplifiers into a multi channel selector switch. The rms panel strains and the force gage outputs are measured with the rms voltmeter using the 100 second time average. The measured panel edge rms strains are presented in Figure 27 as a function of the reference microphone overall sound pressure level for the three noise bandwidths. The force exerted by the panel on the shaker coil, as measured by the force gage, is presented in Figure 28 as a function of the reference microphone overall sound pressure level.

The reference microphone, the force gage and the strain gage outputs, which are monitored throughout the tests with a dual beam oscilloscope, are also recorded onto magnetic tape using a Sangamo tape recorder. Narrow band analysis of the magnetic tape data is performed using the Spectral Dynamics real time analyzer and scaled with the Xerox 5 computer. Typical narrow band analysis of the reference microphone noise at 170 dB OASPL and the corresponding panel strain (strain gage A1) are illustrated in Figures 29 and 30, respectively.

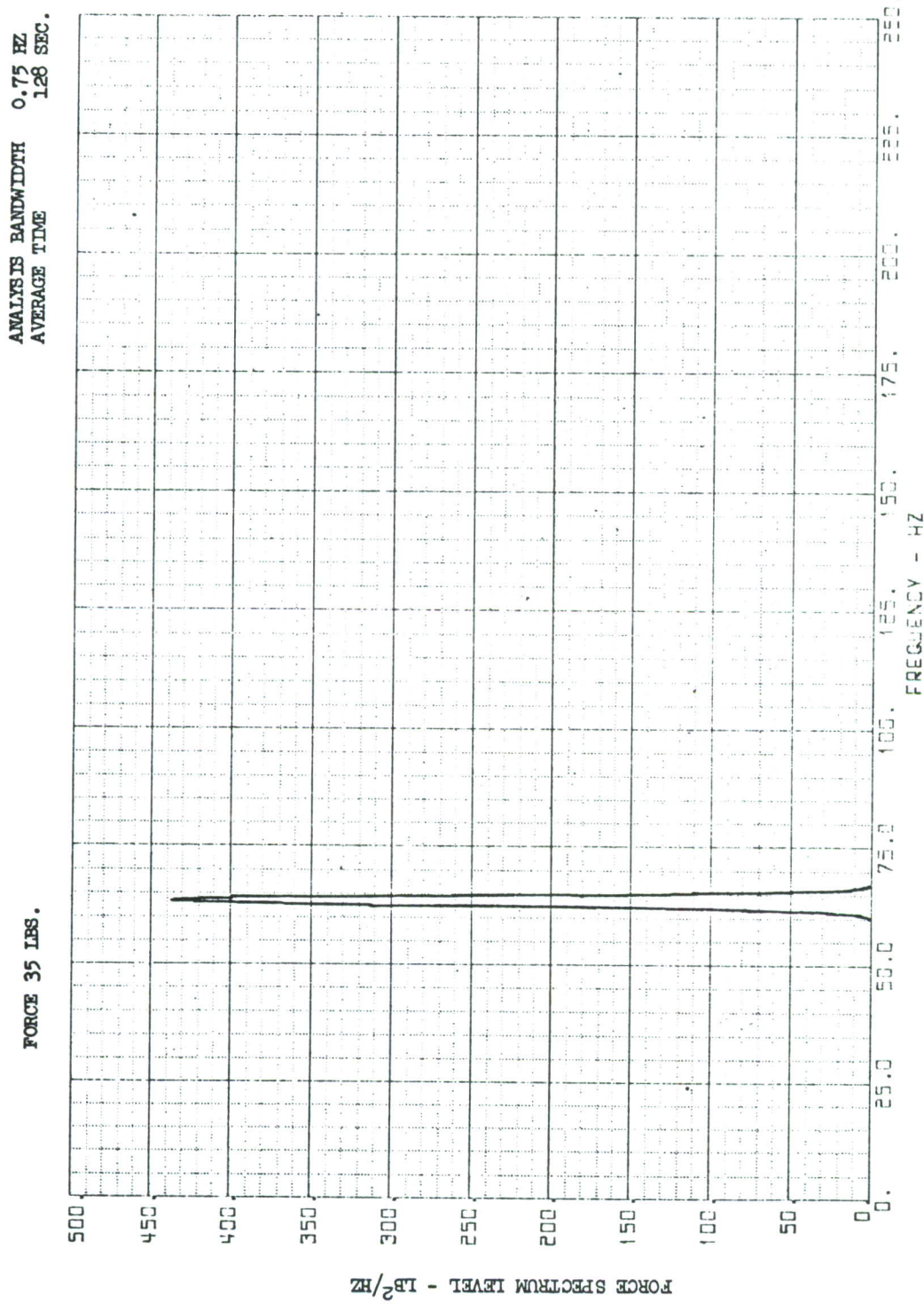


FIGURE 24. TYPICAL NARROW BAND ANALYSIS OF SHAKER FORCE

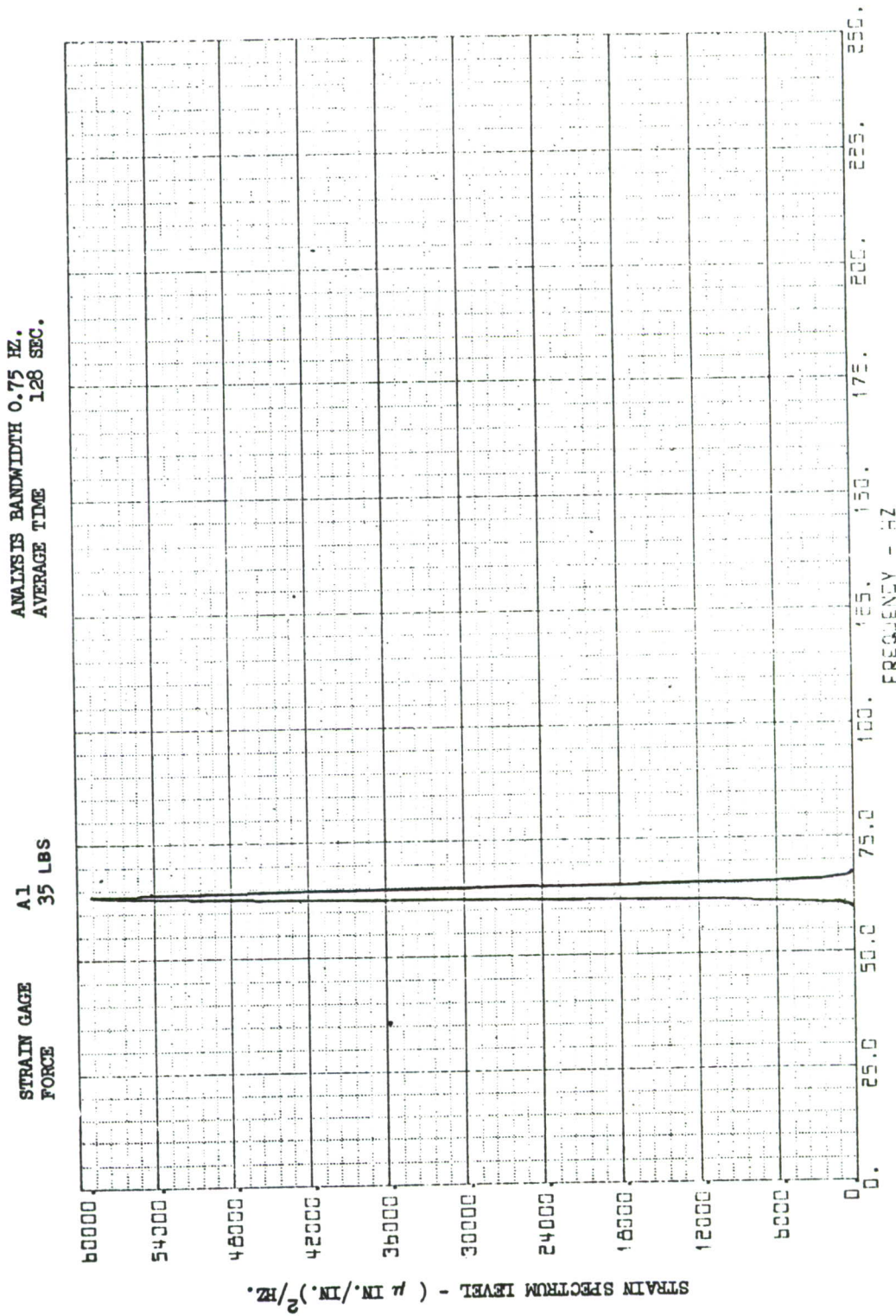


FIGURE 25. TYPICAL NARROW BAND ANALYSIS OF SHAKER EXCITED PANEL EDGE STRAIN

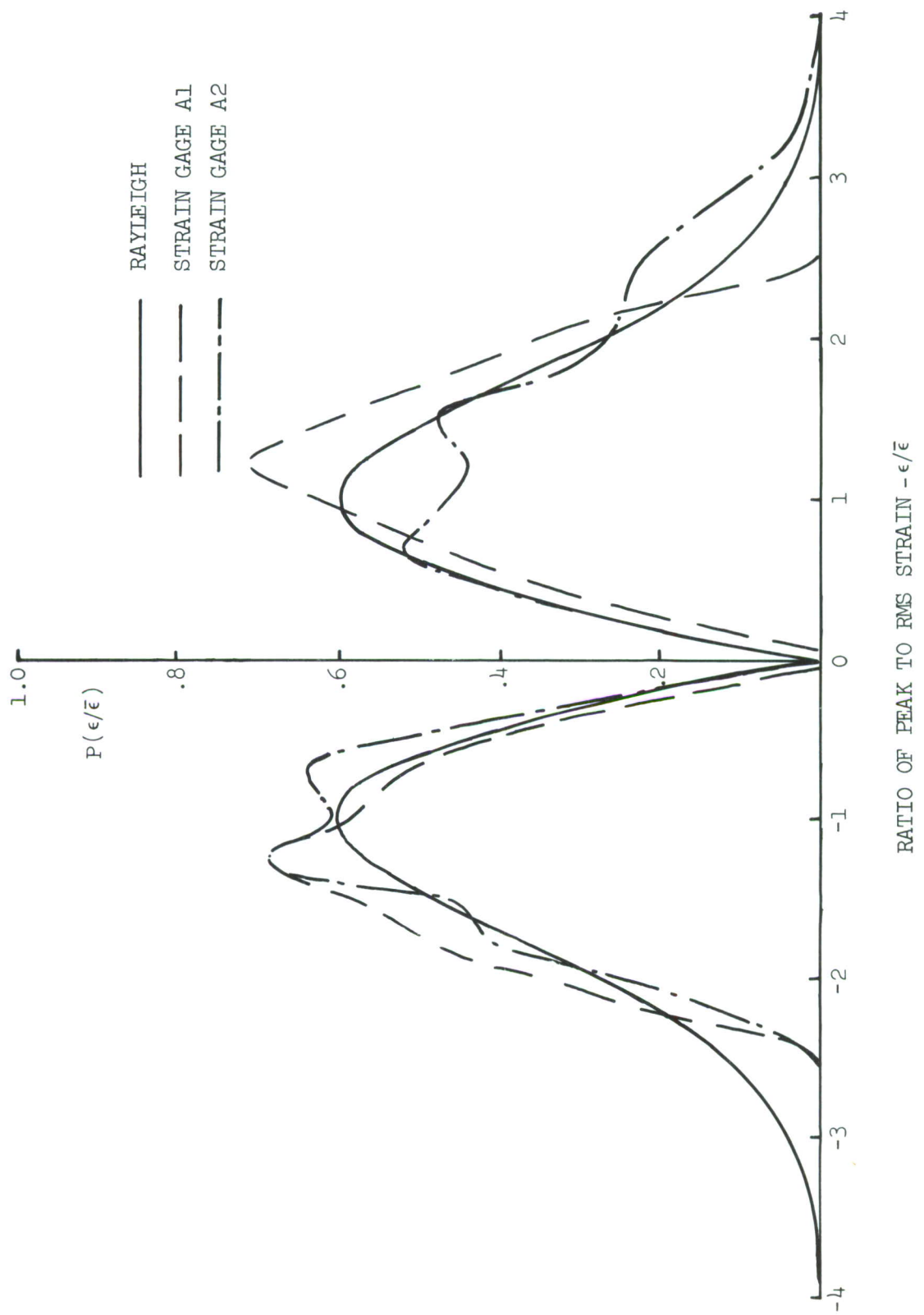


FIGURE 26. PROBABILITY DENSITY DISTRIBUTION OF STRAIN PEAKS AND VALLEYS FOR STRAIN GAGES A1 AND A2, SHAKER EXCITATION

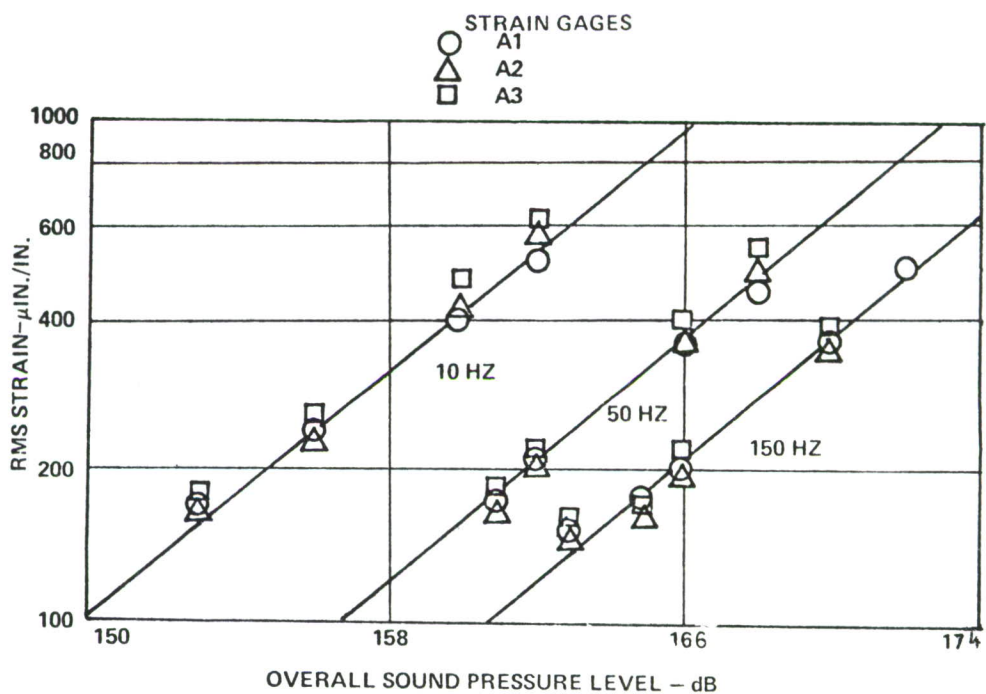


FIGURE 27. PANEL EDGE STRAIN AS A FUNCTION OF REFERENCE OASPL AND NOISE BANDWIDTH

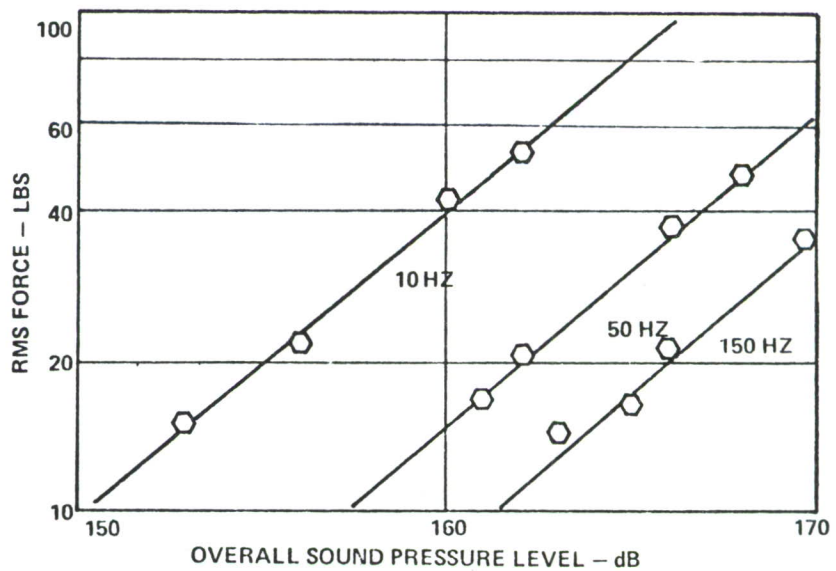


FIGURE 28. FORCE GAGE OUTPUT AS A FUNCTION OF REFERENCE OASPL AND NOISE BANDWIDTH

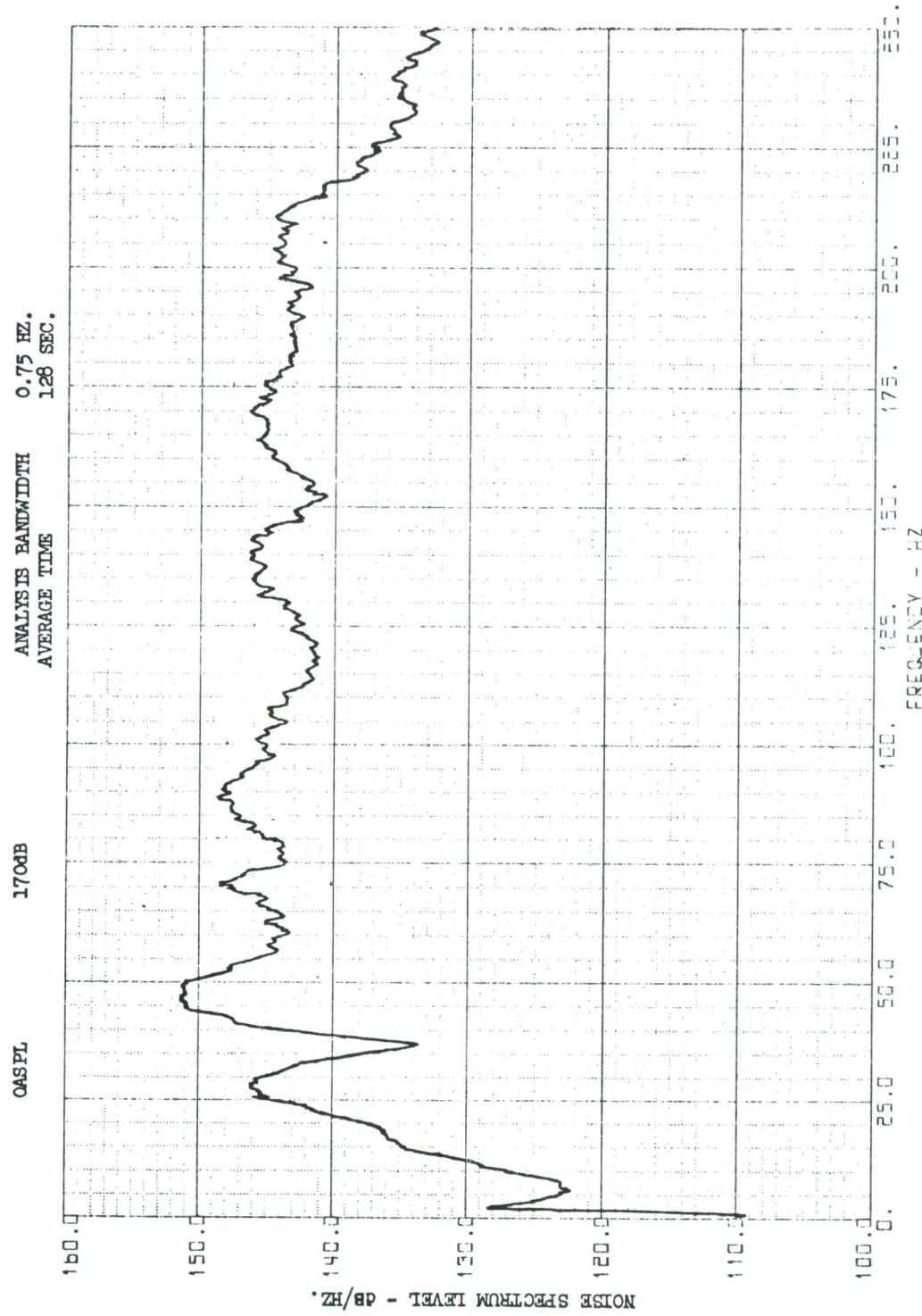


FIGURE 29. NARROW BAND ANALYSIS OF ACOUSTIC EXCITATION

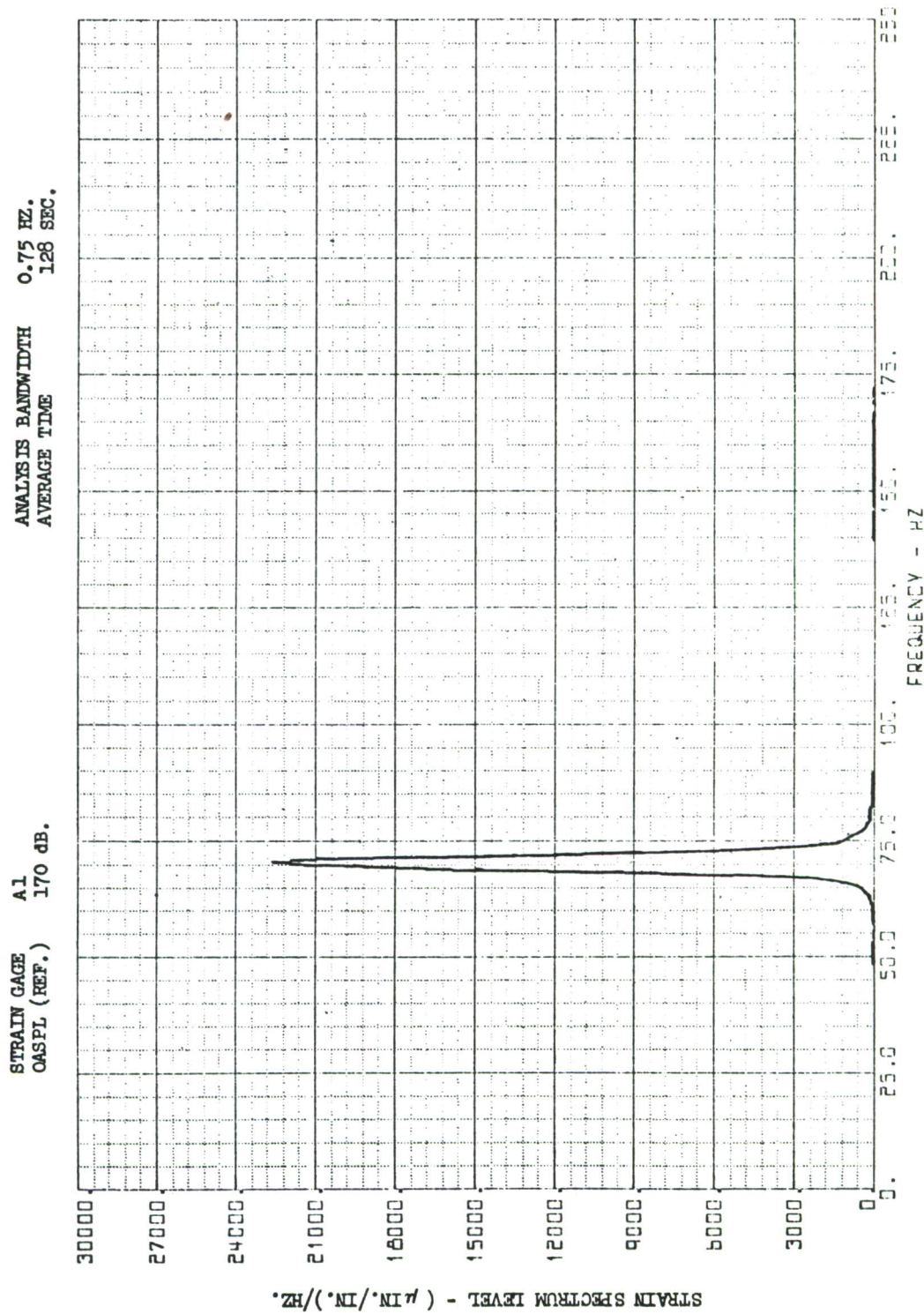


FIGURE 30. TYPICAL NARROW BAND ANALYSIS OF ACOUSTICALLY EXCITED PANEL STRAIN, STRAIN GAGE A1

Typical panel edge strain peak and valley probability density distributions from acoustic excitation are illustrated in Figure 31 for strain gages A1 and A2. An estimate of the panel lateral strain distribution based on the measured strain levels and strain gage locations is illustrated in Figure 32. The strain distribution given by equation 31, using a reduced panel width to reflect the shift of the panel edge stress peak towards the panel center, is included for comparison.

#### 2.4 Calibration of Shaker and Acoustic Excitation

The reference microphone overall sound pressure levels, at selected rms strain levels from Figure 26, are first converted to spectrum levels for the three excitation bandwidths. Thereafter, the reference microphone spectrum levels are corrected to test section spectrum levels at the test panel resonant frequency using Figure 20. Finally, the rms random force levels from Figure 23 are related to the test section spectrum level through the selected rms strain levels. The resulting calibration curve is illustrated in Figure 33.

#### 2.5 Discussion of the Test Results

**2.5.1 Progressive Wave Tunnel Calibration** - The data in Figure 20 indicates that satisfactory spectrum shaping has been obtained at the test section with the NORAIR MK VII noise generator. Variations in the spectrum level as indicated by the narrow band analysis in Figure 29 of the reference microphone noise, are not uncommon to acoustic progressive wave test facilities.

The correction factors obtained from Figure 20 appear to be of acceptable accuracy considering the small scatter in the calculated spectrum levels for the three excitation bandwidths illustrated in Figure 33.

**2.5.2 Panel Damping and Frequency** - In general, it is not possible to determine the damping accurately, using the free decay illustrated in Figure 21, by the log decrement method due to the limited number of cycles. The measured damping coefficient of 0.4 can only be considered as an order of magnitude estimate. Another method of determining the damping assumes that the frequency of the decay pulse, in this instance 65 Hz, corresponds to the frequency of the much reduced resonance peak. Since the measured resonant frequency with the shaker power switched off is 70.4, the single-degree-of-freedom theory indicates a damping coefficient of only 0.28 for the 5.4 Hz shift in the damped response peak frequency (Figure 3).

The measured panel frequency of 70.4 Hz without shaker power is equivalent to a frequency correction factor (equation 10) of 1.33. The 3,1 mode was not detected. A ripple with a frequency of approximately 294 Hz was detected on some free decay traces with the shaker power switched on. This frequency is considerably higher than the calculated mode (3,1) frequency and may be the drive rod or the panel frame resonant frequency.

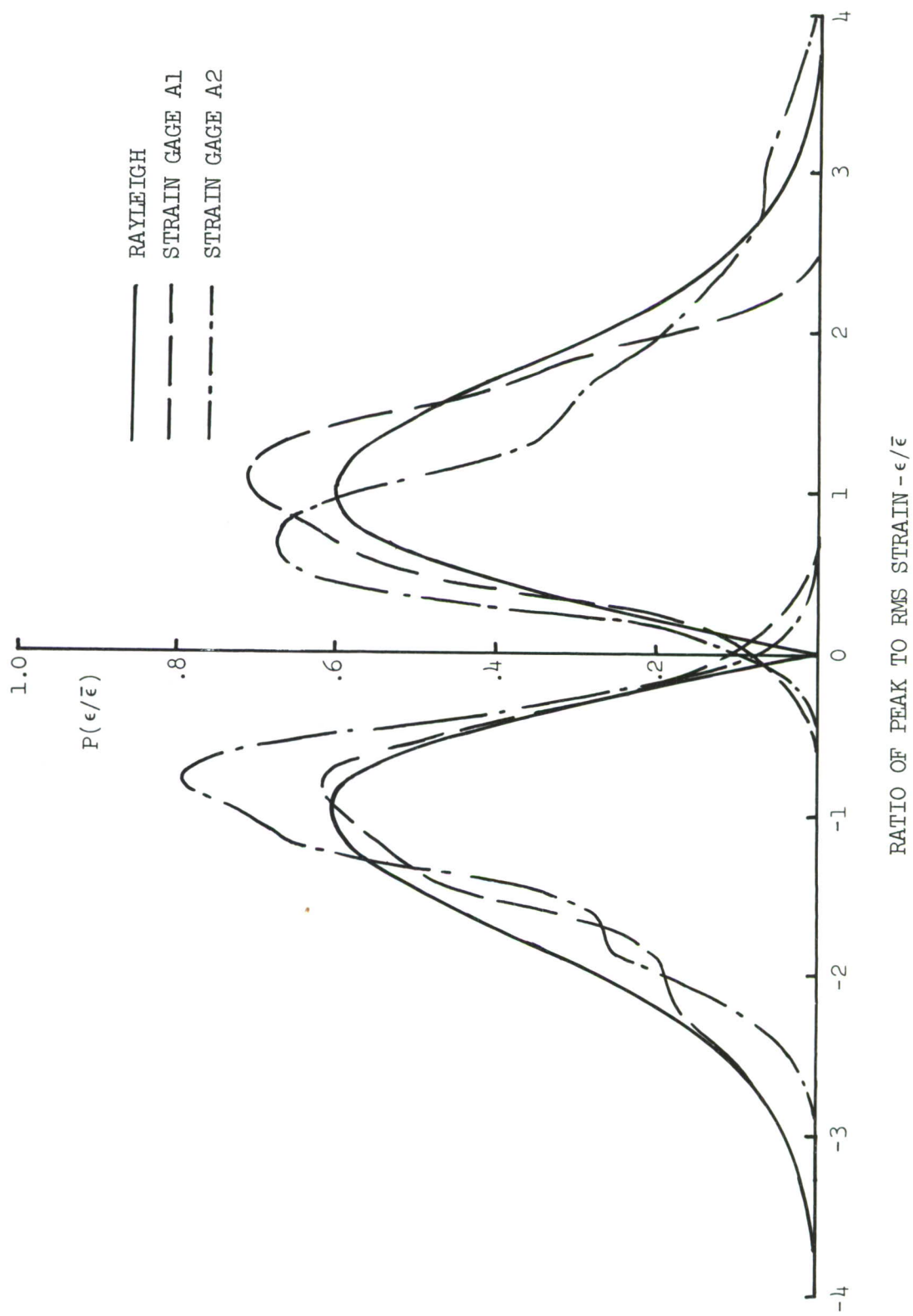


FIGURE 31. PROBABILITY DENSITY DISTRIBUTION OF STRAIN PEAKS AND VALLEYS FOR STRAIN GAGES A1 AND A2, ACOUSTIC EXCITATION

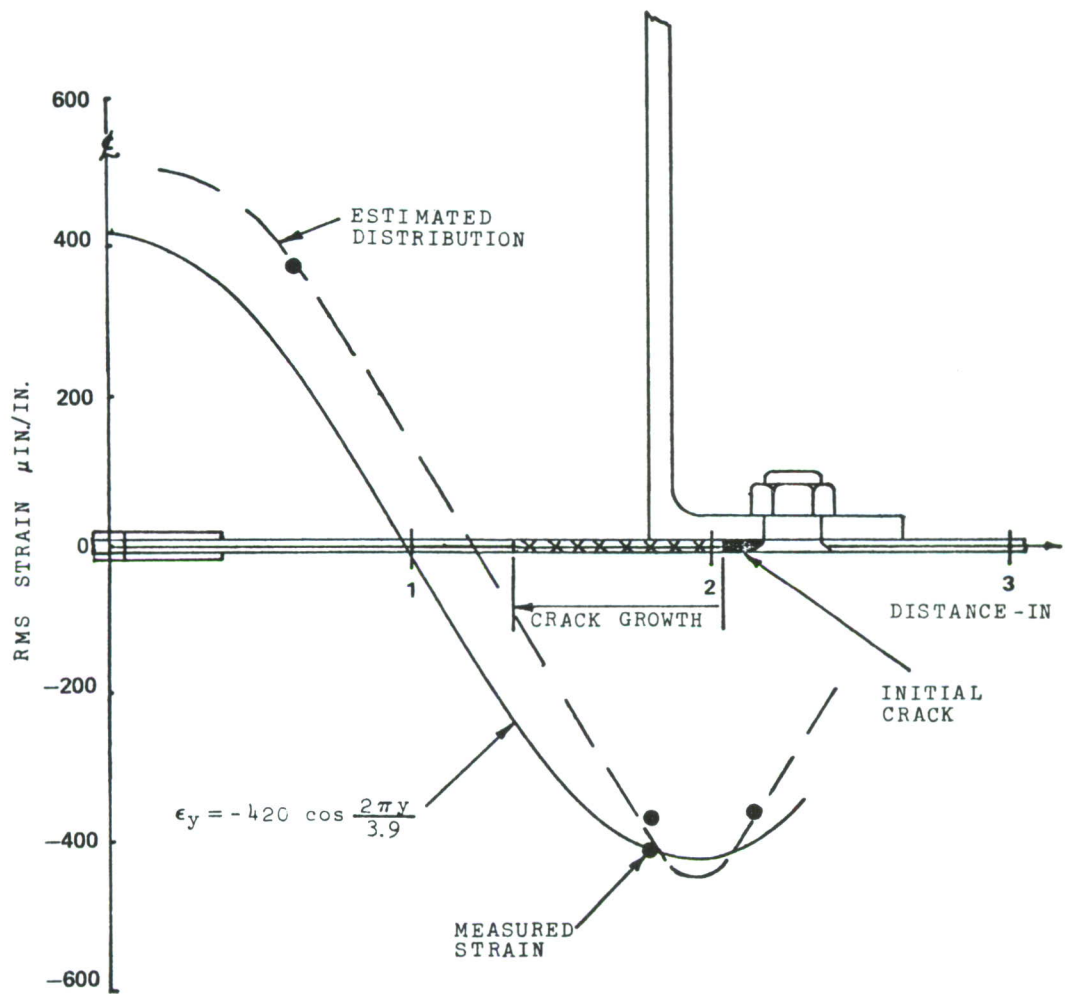


FIGURE 32. PANEL STRAIN DISTRIBUTION RELATIVE TO CRACK GROWTH AREA

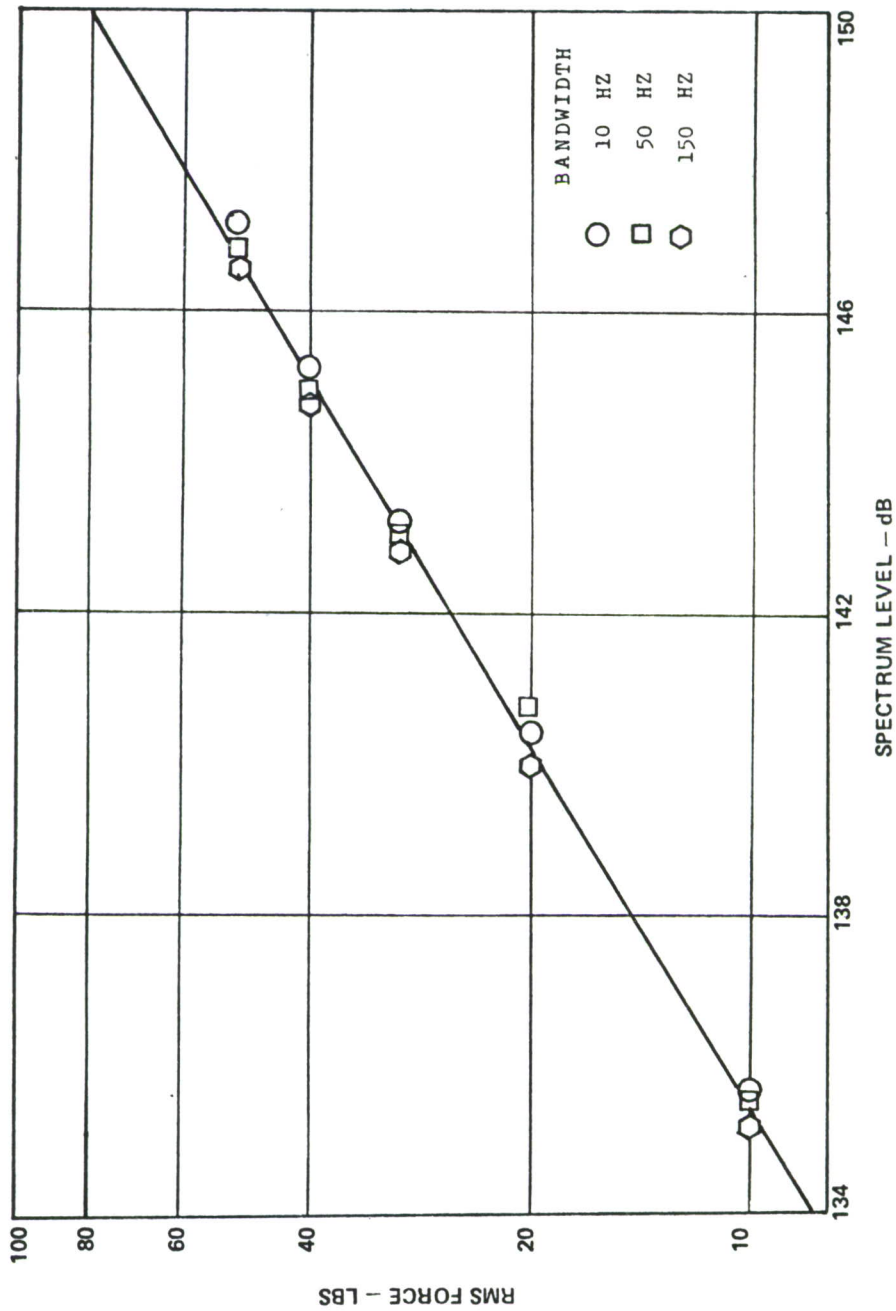


FIGURE 33. CALIBRATION CURVES FOR SHAKER FORCE AND NOISE EXCITATION

The damping coefficient of 0.0095, measured by the free decay method, is in marked contrast to the damping coefficient of 0.025, obtained from the 3 dB point bandwidth in Figure 30. Resolution errors can occur if the analyzer bandwidth is not sufficiently small. On repeating the analysis of the strain gage response using an analysis bandwidth of 0.3 Hz as opposed to 0.75 Hz used previously, at least four narrow band peaks around 70 Hz (Figure 34) are observed. The width of the peaks are compatible with that expected for a viscous damping coefficient of about one percent.

2.5.3 Shaker and Acoustically Excited Panel Response - The correlation of panel edge rms strain response with both shaker excitation force (Figure 23) and acoustic excitation sound pressure level (Figure 27) is generally good as characterized by the small scatter in the measured panel edge strains. The strain gages A1 and A4, placed across the rivet line on opposite sides of the panel (Figure 17) in the location used as the reference in subsequent combined loads tests, produced very small scatter with both discrete and random shaker excitation. Strain gage A4 failed at the beginning of the acoustic tests, thereby preventing a similar comparison with acoustic excitation. Good correlation in the force as measured by the force gage during both the shaker and acoustic excitation was obtained on the basis of equal rms strain.

The narrow band analysis (0.75 Hz bandwidth) of the panel edge strains indicates similar panel response spectra for both shaker (Figure 25) and acoustic (Figure 30) excitation. However, the strain spectrum level from acoustic excitation should be approximately fifty percent greater than that from the shaker excitation due to the differences in the corresponding 3 dB bandwidths, since the rms strain levels are comparable. The observed difference in the spectrum levels is due to the presence of four or more strain response peaks with acoustic excitation (Figure 34) as previously indicated. The approximate rms level can be obtained by first summing the peaks, assuming that the same bandwidth for each peak corresponds to a damping coefficient of 0.0095, multiplying by the bandwidth, and then taking the square root. Due to the narrower filter and reduced integration time, greater statistical errors in the stress peak levels are expected. The breakdown of a single peak into multiple peaks can be caused by small geometric differences, for example, in the force gage position or the rivet line location relative to the frame edge.

The correlation between the shaker excited (Figure 26) and the acoustically excited (Figure 31) panel edge strain probability density distributions indicates that a reasonable simulation has been achieved by the shaker excitation. The distribution of strain peaks and valleys, illustrated in Figure 31, is characteristics of riveted panel edge strains due to random acoustic loading. The large negative strain peaks at the rivet line (strain gage A1) are associated with the outward motion of the panel. The positive peaks are limited by the impingement of the panel on the frame edge during the inward motion of the panel. The large positive strain peaks at the frame edge (strain gage A2) are associated with the bending of the panel about the frame edge during the inward motion of the panel.

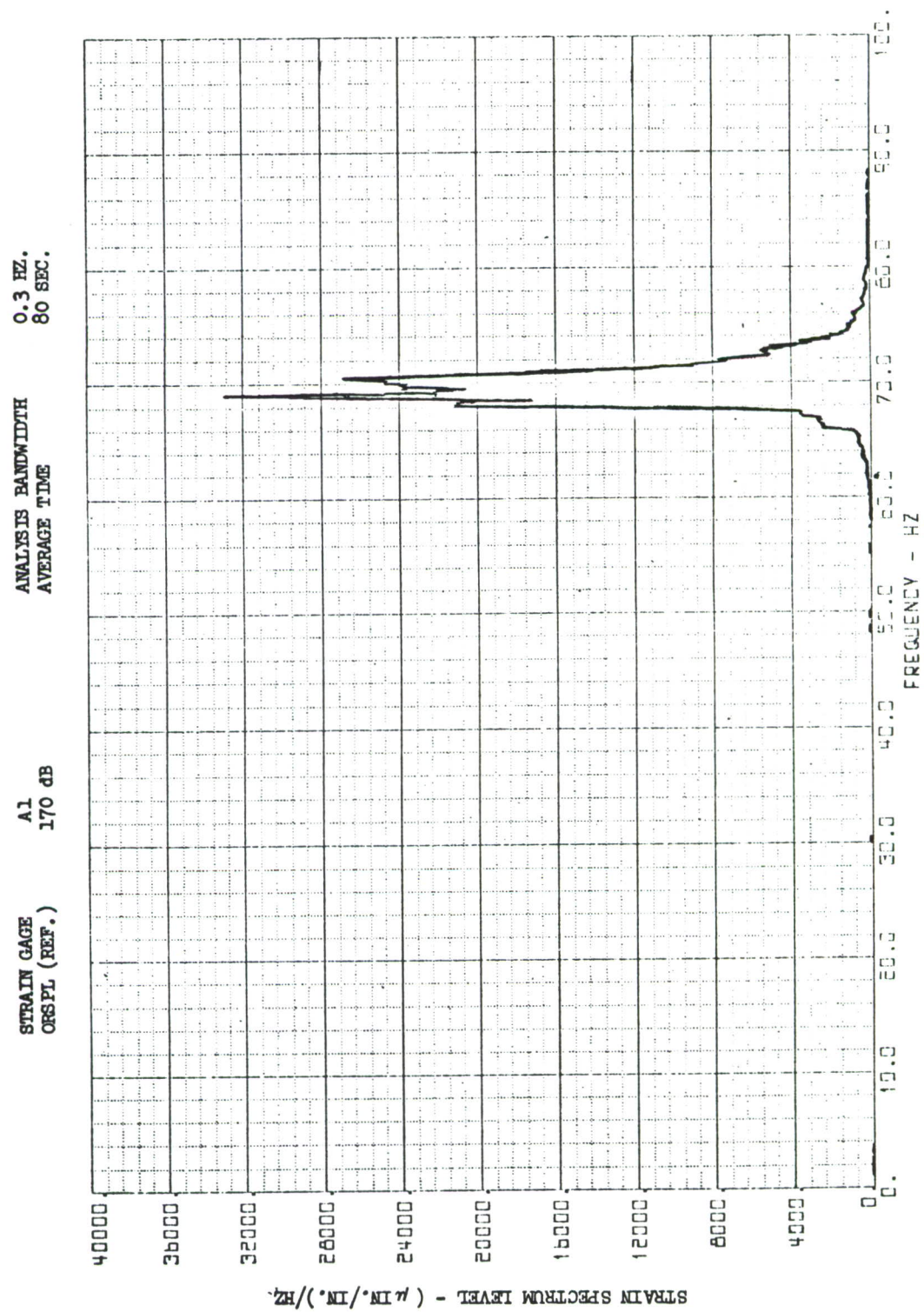


FIGURE 34. REDUCED BANDWIDTH ANALYSIS OF ACOUSTICALLY EXCITED PANEL EDGE STRAIN

The estimated lateral panel strain distribution based on a limited number of data points, illustrated in Figure 32, is influenced at the panel center by the panel center doublers and the finite width of the force gage attachment. Consequently, the correlation between the theoretically assumed and estimated strain distribution does not appear to be good. However, once clear of the center doubler, the correlation is expected to improve.

2.5.4 Calibration Curve - The calibration curve provides an acceptable means for equating the shaker force level to the acoustic excitation level for use in the combined loads tests.

### 3. Combined Loads Tests

The specimens used in the test program are designed to have a constant strain distribution across the panel and to be free of buckling over the proposed load range. Verification of these design objectives is necessary prior to performing the crack propagation tests.

The crack propagation calculations are based on existing constant amplitude crack propagation data. A baseline crack propagation test under comparable loading conditions is necessary to verify the use of the crack propagation data. The crack propagation path and the variation of the strain distribution with crack growth across the panel are also of interest.

The test specimens are subjected to variable inplane loads during the crack propagation tests. The panel edge rms stress produced by the shaker simulated acoustic loading is affected by the inplane loads and has to be determined experimentally. The panel fundamental frequency and damping are required to correlate the measured panel edge rms stress with that which would be obtained from acoustic loading in order to indicate the degree of simulation obtained.

Crack propagation tests are generally performed with a large number of test specimens to achieve a high degree of statistical accuracy. In this preliminary study, a small statistical sample represented by a single test panel at each load condition, is used. The confidence level, however, can be increased, to some extent, by the use of identical flight-by-flight load cycles and cycle sequences, apart from the compression load duration, in each set of three load tapes for the upper wing surface loads and also for the lower wing surface loads. Additional consistency, within each load tape set, can be obtained by assigning each load tape set to a specific fatigue machine. Variations between the test specimens can be determined by subjecting the test specimens to constant amplitude cyclic inplane loads.

To isolate the effects on crack propagation of the combined acoustic and flight loads, the flight-by-flight tests are performed without and then with simulated acoustic loading.

The use of two load levels, represented by the upper and lower wing surface loads, in conjunction with a constant shaker simulated acoustic loading, provides additional means, on a comparative basis, of isolating the combined acoustic and flight loads effects on crack growth.

Calculations for crack propagation under acoustic loading indicate that crack propagation will not be obtained from the flight load type crack. Consequently, a typical sonic fatigue crack from which crack propagation can be expected, is also included in the panels which are subjected only to acoustic loading, to verify the forgoing hypothesis and to provide preliminary data on crack propagation in riveted panels.

A matrix of the test sequence, test panels, load tapes and loading conditions employed in the phase 2 test program is presented in Table 13. The increased flight-by-flight load levels used in the test program correspond to conversion factors of 1g flight load to 12230 psi stress and 1g ground load to 8000 psi stress for the lower and upper wing surface load spectra, respectively. The compression stress is maintained at 7500 psi. The calibration signal on each load tape is equal to the maximum load level. The maximum loads are 30,490 and 20,400 pounds for the lower and upper wing surfaces, respectively (Tables 11 and 12).

The acoustic level corresponding to the increased flight loads is approximately 144 dB, which is equivalent to a shaker force of 35 lbs. rms (Figure 33), representing a panel rms bending strain of 350  $\mu$  in/in (Figure 23) at zero inplane load.

### 3.1 Instrumentation

Three uniaxial (F4, F5 and F6) and one strain gage rosette (F1, F2 and F3), illustrated in Figure 35, are employed on test panel CF3, which is used in the baseline test. Each strain gage is wired with three leads for temperature compensation. Strain gages F6 and F3 are used to establish the position of the neutral axis. The strain gage rosette is used to define the state of stress in the test panel and, consequently, is placed clear of the fasteners. Strain gages F3 to F5 provide information on the strain distribution across the panel. Strain gage F5 is also used to indicate the onset of buckling should it occur.

On all subsequent test panels, strain gage F6 is deleted and the strain gage rosette is relocated with strain gage F1 positioned across the rivet line at the panel lateral centerline, as illustrated in Figure 36. The F1 strain gage location corresponds to the strain gage A1 or A4 location on the calibration panel and is used to measure the strain due to shaker simulated acoustic loading. The position of strain gage F3 is essentially unaltered, whereas strain gage F2 position is such that it is now influenced by the fastener.

Table 13. PHASE 2 TEST PROGRAM MATRIX

TEST SEQUENCE	220 KIP MTS MACHINE		UPPER WING SPECTRA 220 KIP MTS MACHINE		LOWER WING SPECTRA 160 KIP MTS MACHINE		LOADING COMBINATIONS
	ACOUSTIC TEST PANEL	BASELINE TEST PANEL	TEST PANEL	LOAD TAPE	TEST PANEL	LOAD TAPE	
1		CF3					* GAG Cycle
2			CF7	GA2	CF8	FA2	* GAG + Spectra
3			CF9, CF9-2	GA2	CF10	FA2	* GAG + Spectra + Take Off Acoustic
4			CF11	GA3	CF12	FA3	* GAG + Spectra + Take Off and Flight Acoustic
5			CF5	GA1	CF6	FA1	Tension + Spectra + Continuous Acoustic
6			CF2				Continuous Acoustic
7		CF4					Continuous Acoustic + Compression

\* Ground-Air-Ground

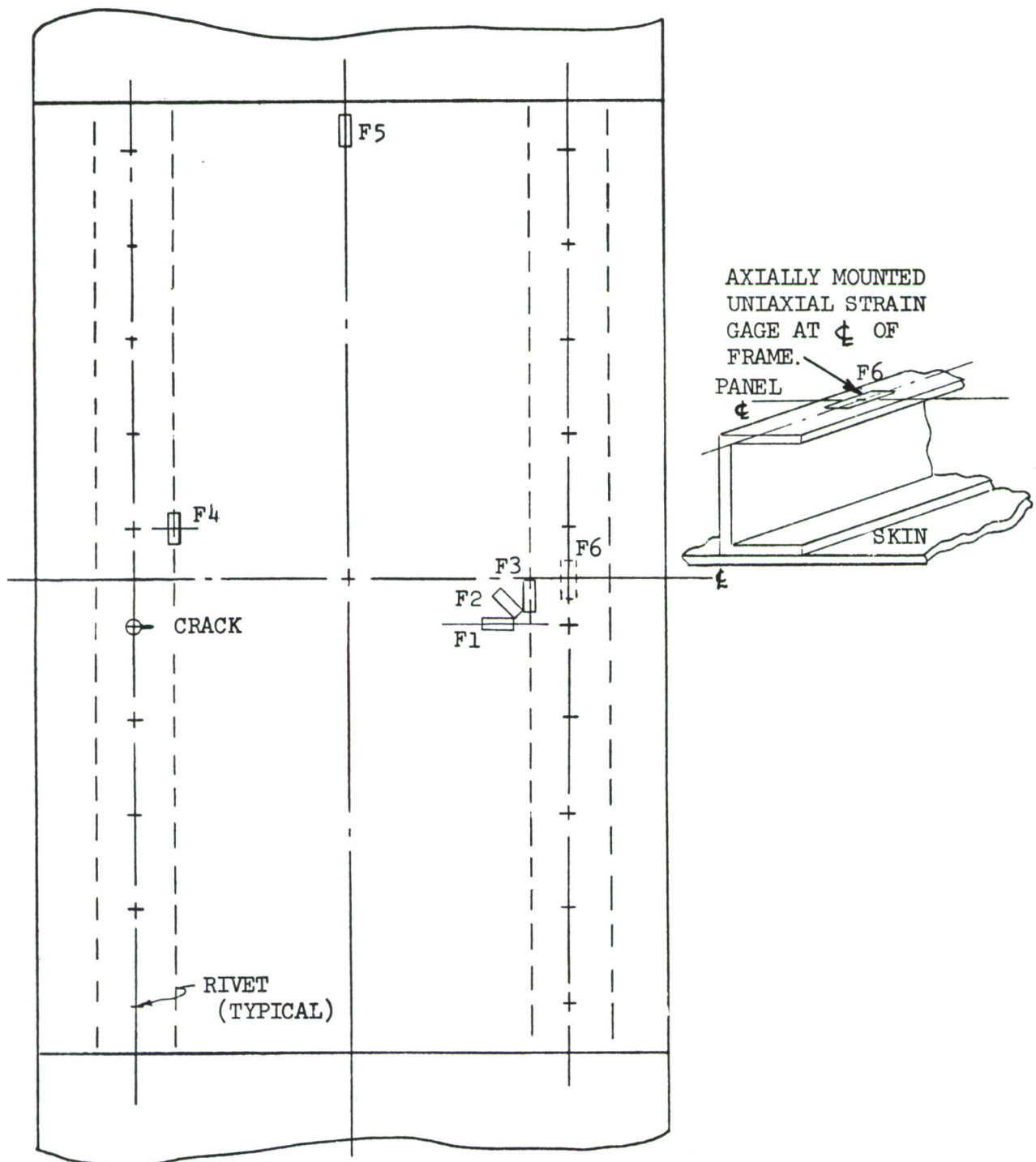


FIGURE 35. BASELINE TEST PANEL CF3 STRAIN GAGE LOCATIONS

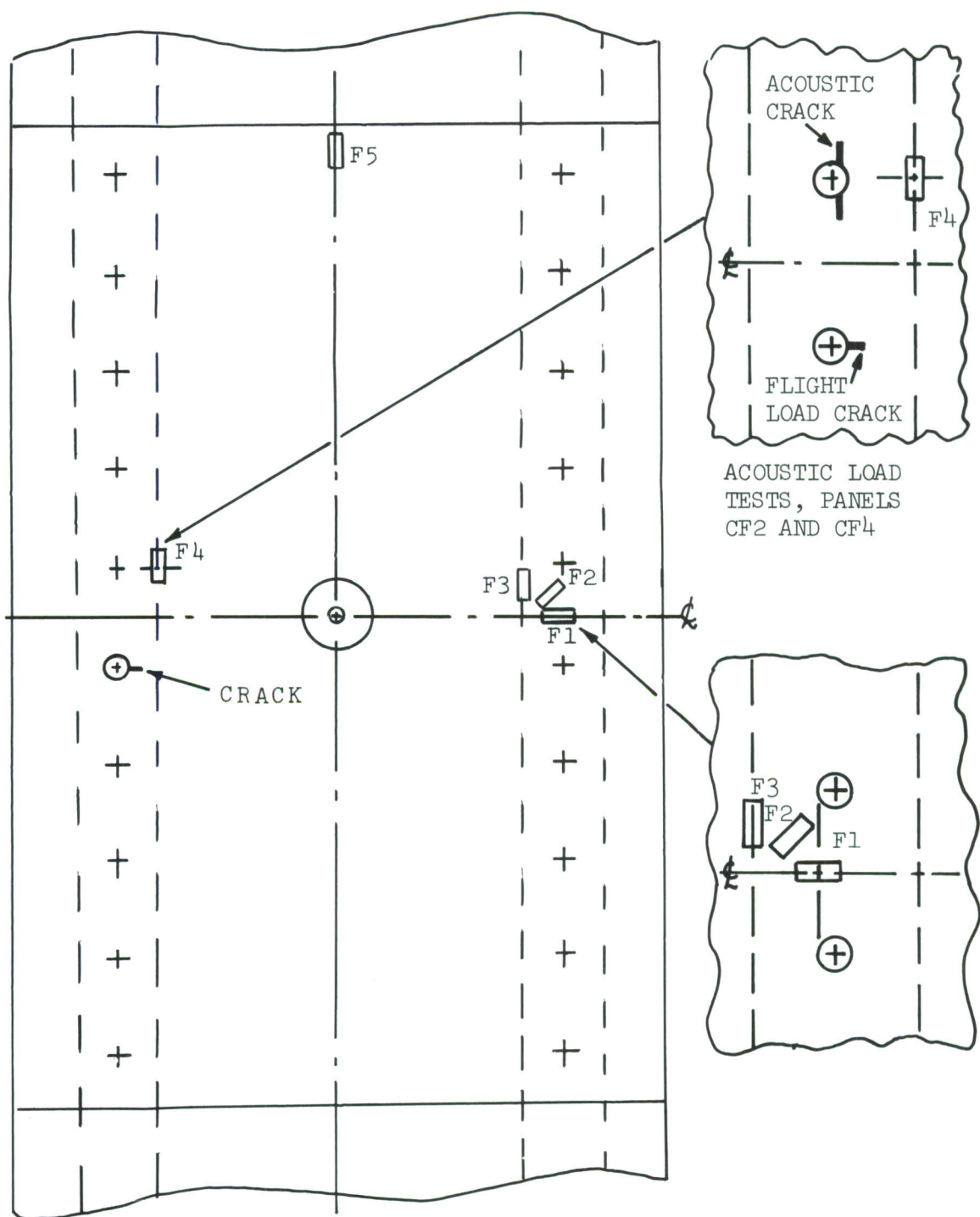


FIGURE 36. COMBINED LOADS AND ACOUSTIC LOADS PANEL STRAIN GAGE LOCATIONS

A single B&K force gage is mounted on the center of each test panel to measure the shaker simulated acoustic loading. The inplane panel loads are measured by calibrated load cells built into the fatigue machines.

The strain gages are calibrated prior to each data recording. The calibration is achieved first by zeroing the load cell and balancing each strain gage circuit. The strain gage bridge is then unbalanced with a high precision calibrated resistor to provide a known positive and negative equivalent strain. Each force gage is calibrated initially by loading the force gage with a known weight.

### 3.2 Test Set-Up

In preparing the fatigue machines for the crack growth tests, the end grips are first attached to the fatigue machine, aligned and torqued. The fatigue machine load cell is then zeroed and the test specimen is installed.

The installation of the test panel in the fatigue machine involves the attachment of the panel and the end grip attachments to the end grips by means of the two 1.25-inch diameter close tolerance bolts. The end grip attachments are aligned with the test panel, shimmed where necessary, and held by the 5/8-inch diameter bolts through the end grip attachments and the panel ends. The alignment is facilitated by the 0.69-inch diameter large clearance bolt holes drilled into the panel ends. The test panel frame web and lower flange, together with the panel skin, are drilled through the corresponding holes in the end grip attachments and the fasteners are installed. Four frame web stabilization blocks, two to each end of the test specimen, are fitted between the two frame webs, shimmed and fastened. The blocks are located near the discontinuities in the one-inch thick end grip attachment fingers to remove web bending loads introduced by the discontinuities. The need for the stabilization blocks was established during the cycling in the baseline test. Finally, the 1.250-inch and 5/8-inch diameter bolts are torqued to complete the installation. This complex installation procedure, which is dictated by interference between the end grip bolts and the one-inch thick end grip attachment, provides good panel alignment. After the completion of the installation, the load cell is zeroed in preparation for strain gage calibration.

The test panel installed in the 220,000-pound force MTS fatigue machine, together with the control console, is illustrated in Figure 37. The test set up illustrated in Figure 37 is used for the preliminary compression tests and the flight-by-flight load tests which do not involve shaker excitation. The fatigue machine load is controlled by magnetic tape or, for simpler loads, by waveform generators in the control console. The test set up used in the combined shaker simulated acoustic and flight-by-flight load tests is illustrated in Figures 38 and 39. The frame web stabilization blocks are visible in Figure 38. The shaker is mounted on free swinging turnbuckles and stabilized by two aluminum alloy flexures. The shaker

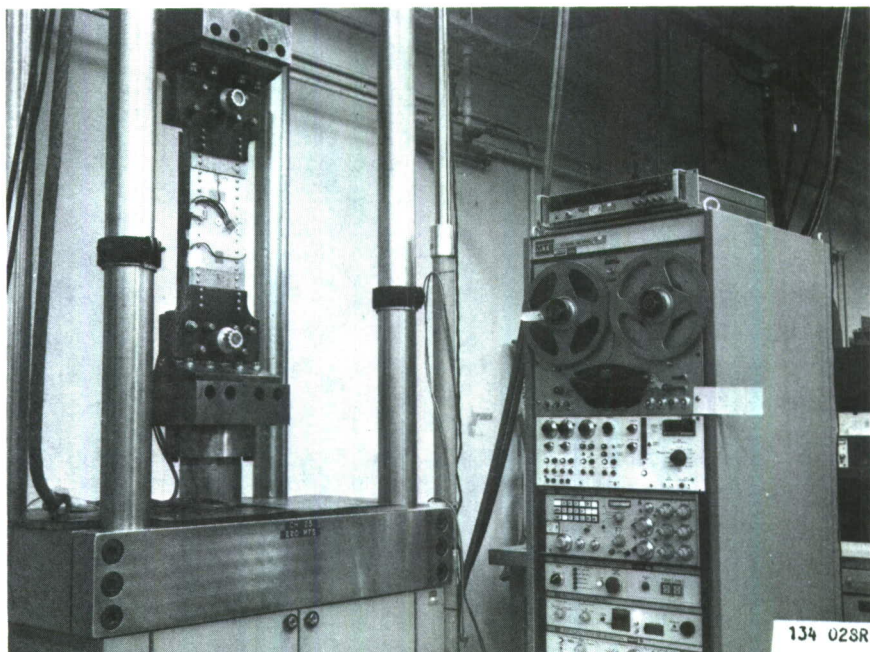


FIGURE 37. TEST SET-UP FOR BASELINE AND FLIGHT LOAD TESTS

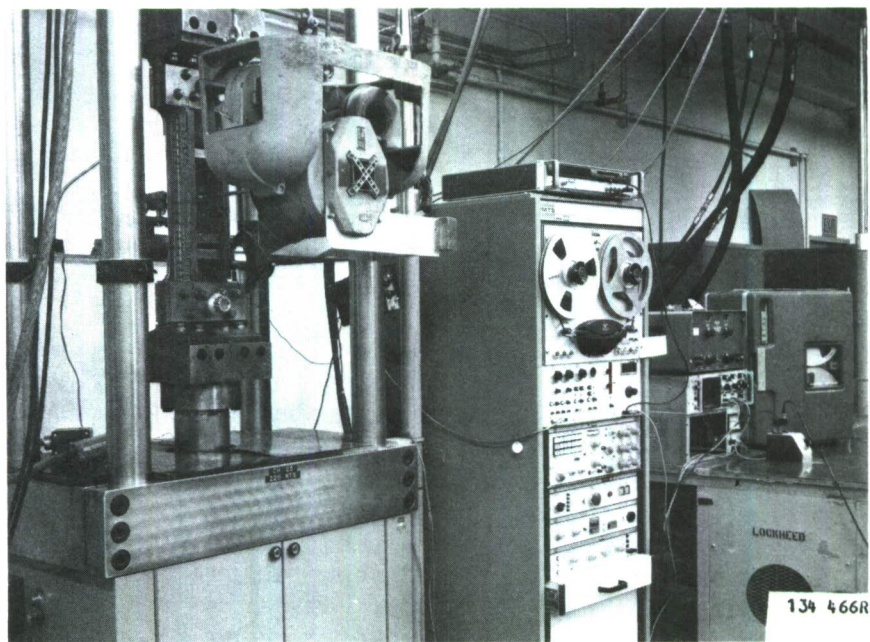


FIGURE 38. TEST SET-UP FOR COMBINED ACOUSTIC AND FLIGHT LOAD TESTS

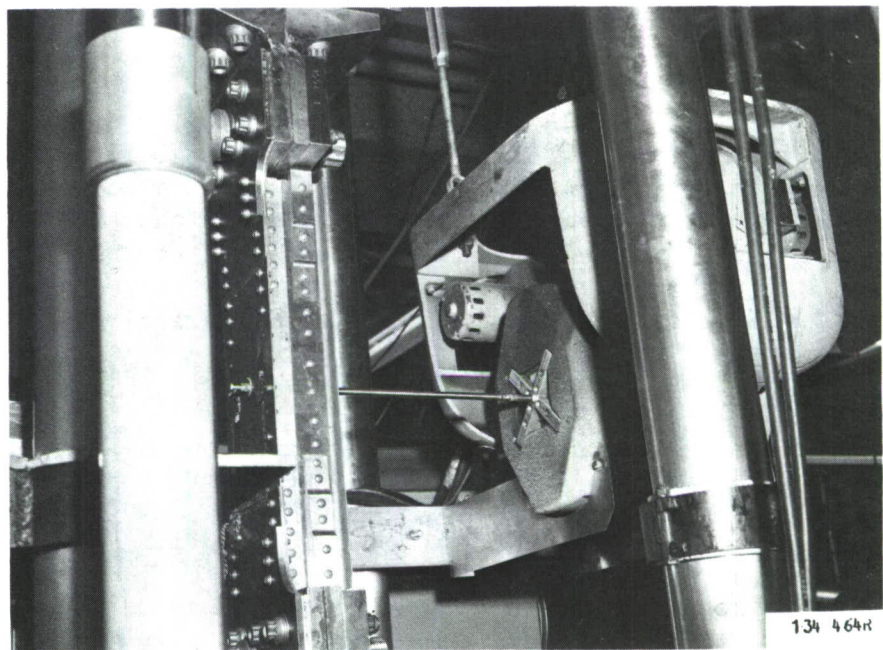


FIGURE 39. CLOSE-UP OF TEST SPECIMEN AND SHAKER DRIVE ARRANGEMENT

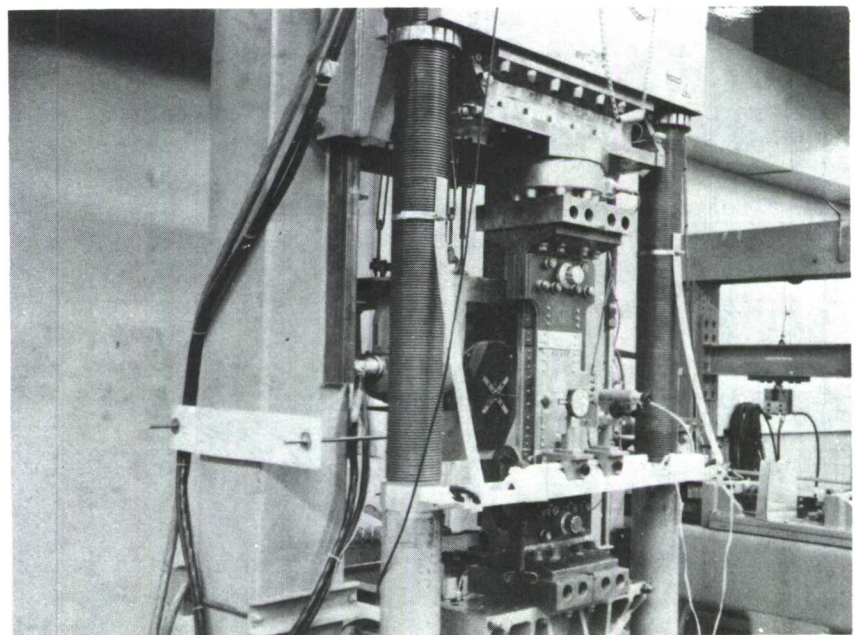


FIGURE 40. TYPICAL ARRANGEMENT FOR MEASURING CRACK GROWTH

load signal is fed from the Ampex tape recorder, through a Kronhite band-pass filter and the shaker mobile power amplifier to the shaker.

The crack growth is measured by means of a travelling microscope and displacement dial arrangement, as illustrated in Figure 40, attached to the 160,000-pound force fatigue machine. The test specimen and shaker arrangement are also shown in the same figure. The flight loads are measured by built in load cells and the shaker force is measured by the B&K force gage. The load cell, force gage, and strain gage signals are fed through the appropriate signal conditioning systems and amplifiers directly into the Central Data System Xerox 5 computer. The signals are monitored by oscilloscopes and by instant feedback on the CRT display.

The load levels are set by the calibration signals on the flight-by-flight load tape. The shaker force level is set by means of the TSI rms meter.

### 3.3 Test Procedure

Three basic test procedures are used. The first is concerned with the verification of the panel design objectives and the establishment of the baseline crack propagation characteristics. The second test procedure is used on all test panels involving flight-by-flight loads and the third procedure is used with panels loaded only with shaker simulated acoustic loads. The test specimen response histories are recorded in the Central Data System Xerox 5 computer. A sampling rate of 1500 samples a second is generally used. For the recording of strain, load cell and force gage histories, the sampling rate is, however, reduced to 750 samples per second. The flights are automatically counted from markers on the load tape.

At the conclusion of the test program, a number of test specimens are selected for fractographic examination of the crack surface.

#### 3.3.1 Baseline Tests - The test procedure used for the baseline test specimen CF3 is summarized as follows.

- (1) At zero inplane load, zero strain gages and measure precrack length.
- (2) Apply compression load slowly to a panel compression stress of approximately 7500 psi and back to zero again.
- (3) Monitor strain gage F5 and record all strain gages during loading and examine quick look data on CRT display.
- (4) Cycle panel at 5 Hz between tension and compression stress of 8900 and 7500 psi, respectively, and record strain data.
- (5) Examine behavior of test panel, modify test panel, as required, and repeat above procedure until a satisfactory modification is obtained.

- (6) Cycle panel at 5 Hz at the above stress levels until crack growth is detected, measure crack length and note load cycles.
- (7) Measure crack length initially after every 5000 cycles and thereafter with increasing frequency to correspond to a crack growth of approximately 0.03 inches between readings and note load cycles.
- (8) Zero strain gage and record load and strain data at every half inch of crack growth up to two inches and, thereafter, at every inch until the crack has propagated across the panel and photograph crack progress.
- (9) Examine crack surface after cutting test specimen.

3.3.2 Flight-by-Flight Loads and Combined Loads - The general test procedure for the combined acoustic and flight loads is summarized as follows.

- (1) Zero inplane load and all strain gages and measure precrack length.
- (2) With the power to the shaker switched off, obtain panel free decay at every 5000 pound inplane load increments between 20,000 and 10,000 pounds of tension and compression, respectively, by tapping the shaker coil and recording the response data.
- (3) At zero inplane load, excite test specimen with shaker using acoustic load tape and adjust shaker load level to obtain an rms strain reading of 350  $\mu$ in/in with a TSI rms meter for strain gage F3. Note force level.
- (4) Apply inplane load in increments of 5000 pounds from a compression load of 10,000 pounds to a tension load of 20,000 pounds, each time measuring both the rms strain and the force levels using a 30 second time average. After test, switch shaker off.
- (5) Cycle test panel at 5 Hz between tension and compression load levels of 12,760 and 10,750 pounds, respectively, to initiate crack. Record the panel strain response for all strain gages for a few cycles.
- (6) After crack initiation measure crack length. Calibrate fatigue machine with calibration signal on flight-by-flight load tape. For initial use of load tapes, record load cell history for comparison with signal on load tape.
- (7) Measure crack length and apply the shaker and flight-by-flight loads. Record strain gage, force gage and load cell signals and perform a peak and valley count at the beginning of the test for predefined three or four typical flights. Measure crack length after typically 100 to 200 flights, each time noting the total number of flights.
- (8) To rewind the flight-by-flight and the acoustic load tapes, the flight loads are switched off first and the shaker amplifier gain is then turned down.

(9) When a crack length of approximately 0.8 inches is reached, the strain, force gage and load cell histories are recorded and the test is stopped. The test specimen is photographed and a continually increasing static tension load is applied to fail the test panel and expose the crack surface.

When only flight-by-flight load tests are performed, without the shaker being attached to the test panel, steps (2), (3), (4) and (8) are deleted from the above test procedure. The references to the shaker load and the force gage are also to be deleted from step (7).

3.3.3 Shaker Loading - Two test panels are tested with shaker simulated acoustic loading. One of the test specimens is simultaneously subjected to a constant compression load. Since the two precracks in the panel are at right angles to each other (Figures 11 and 12), crack initiation by cycling is dispensed with. The crack growth tests with acoustic loading described in Reference 16 indicates that rapid crack initiation is obtained from a saw cut. The procedure used is summarized as follows.

- (1) Zero the load cell and all strain gages and measure the precrack lengths.
- (2) Perform free decay tests at zero inplane load on both panels. For the panel to be tested with a compression load, free decay tests at compression loads of 5000 and 10,000 pounds are also performed.
- (3) At zero inplane load, apply shaker loads from the acoustic tape to the test specimens and adjust the force level to obtain an rms strain of 350  $\mu$  in/in at gage F3. For the test panel to be used with the compression load, also apply compression loads of 5000 and 10,000 lbs. while measuring the rms strain and force.
- (4) At zero compression load for one test panel and at 10,750 pounds compression load for the other test panel, conduct crack growth tests. Record strain gage and force gage histories and obtain a peak and valley count at the beginning of the tests. Note the crack growth data after typically 30 to 90 minutes of test time. At the end of the test, photograph the test panel and cut the panel to examine the crack surface.

#### 3.4 Data Analysis

The crack growth data is noted during the test. The rms strain and force levels are measured with the TSI rms meter and also noted during the test. The majority of the data is of the quick look type and hard copies of this data are obtained during or after the test.

The Xerox 5 computer is used to analyze the stored test panel peak and valley count data and strain response data for the flight-by-flight and acoustic load tests. The analyzed data is presented as peak and valley

distribution and narrow band strain response spectra. The narrow band spectral analysis of the panel response, which uses the Fast Fourier Transform, is restricted to response data with a constant mean load.

### 3.5 Test Results

3.5.1 Baseline Test - Test specimen CF3 is used in the baseline test. The load strain curves for all strain gages obtained during the compression load test are illustrated in Figure 41. Typical load history and the corresponding load-strain curve (strain gage F3), recorded during the constant amplitude cycling at 5 Hz, are illustrated in Figures 42 and 43, respectively.

The peak tension and compression strains, obtained from the load and strain data sampled at typically  $\frac{1}{2}$ -inch crack growth intervals during the constant amplitude crack propagation test, are illustrated in Figure 44 for all axial strain gages on the test specimen face sheet. The ratio of minimum to maximum peak load ( $R$ ) varied between 0.854 to 0.862 during the constant amplitude crack propagation test, with an average at 0.857.

The crack growth data was obtained to a crack length of 3.229 inches after 143,900 load cycles. The test was stopped after the test panel broke from the precrack fastener hole to the panel edge at a total of 154,327 load cycles. A crack was observed in the stiffener adjacent to the panel crack at the end of the test. The crack propagation path is illustrated in Figure 45. The crack face in the panel is initially normal to the panel surface. However, at a distance of approximately one inch from the precrack tip, it takes on the appearance of a ridge (or valley) with the apex at the half panel thickness.

The crack propagation test data, in terms of the crack growth rate and the effectiveness stress intensity factor,  $K_{eff}$ , is presented in Figure 46. The effective stress intensity factor, represented by the expression in the parenthesis in equation 44a, is computed from the stress data using equation 63. Comparable crack propagation data from Reference 35 is included in Figure 46 for comparison.

3.5.2 Flight-by-Flight and Combined Loads - The flight-by-flight and combined load tests were performed using panel numbers CF5 through CF12. The upper wing surface loads were applied to panels with odd numbers using the 220,000 pound force MTS fatigue machine and the lower wing surface loads were applied to the panels with even numbers using the 160,000 pound force MTS fatigue machine.

The peak tension and compression stresses, based on the measured strains during the 5 Hz crack initiation cycling between tension and compression load levels of approximately 12,760 and 10,750 pounds, respectively, are illustrated in Figure 47. The crack initiation cycling data for test panel

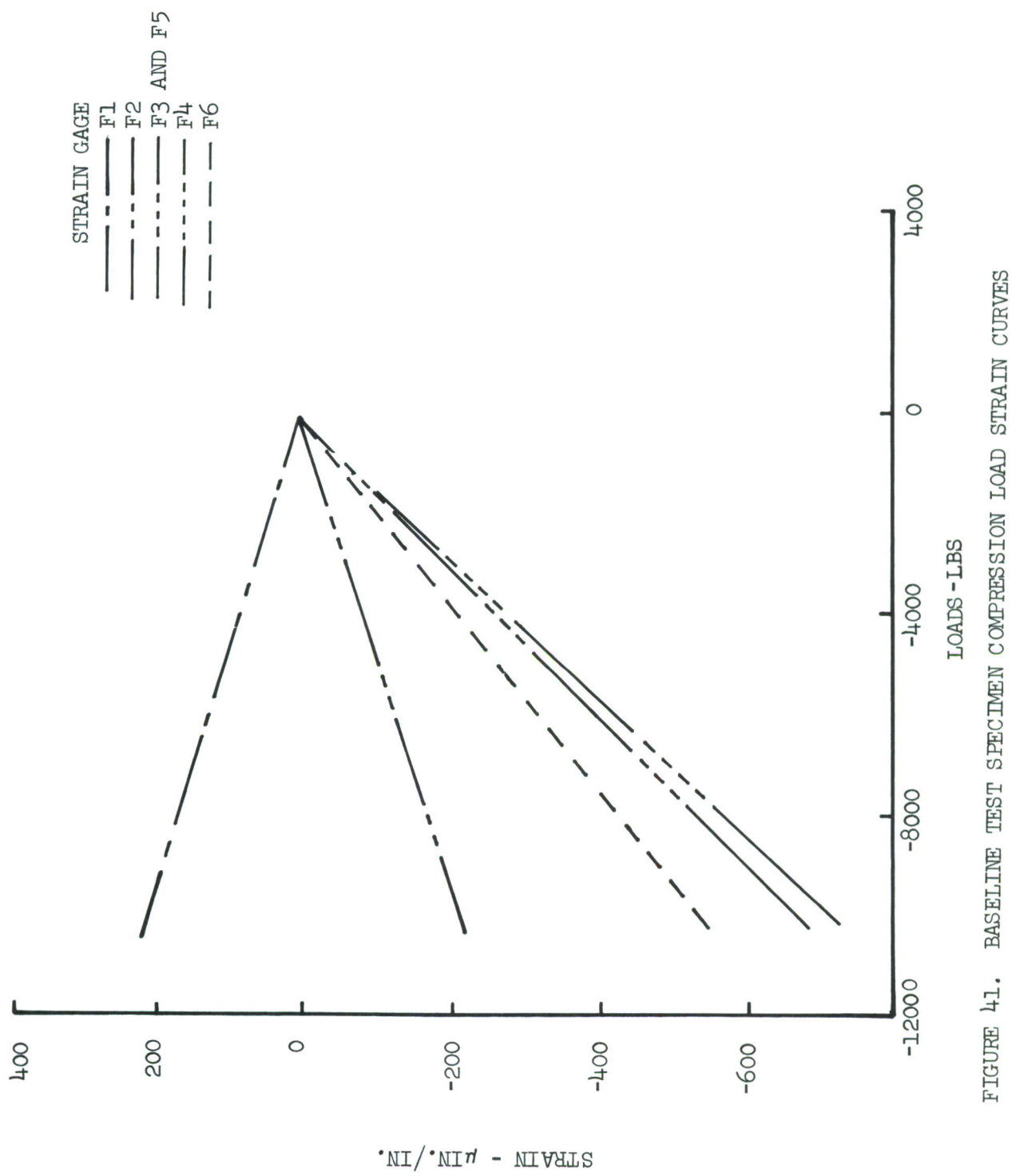


FIGURE 41. BASELINE TEST SPECIMEN COMPRESSION LOAD STRAIN CURVES

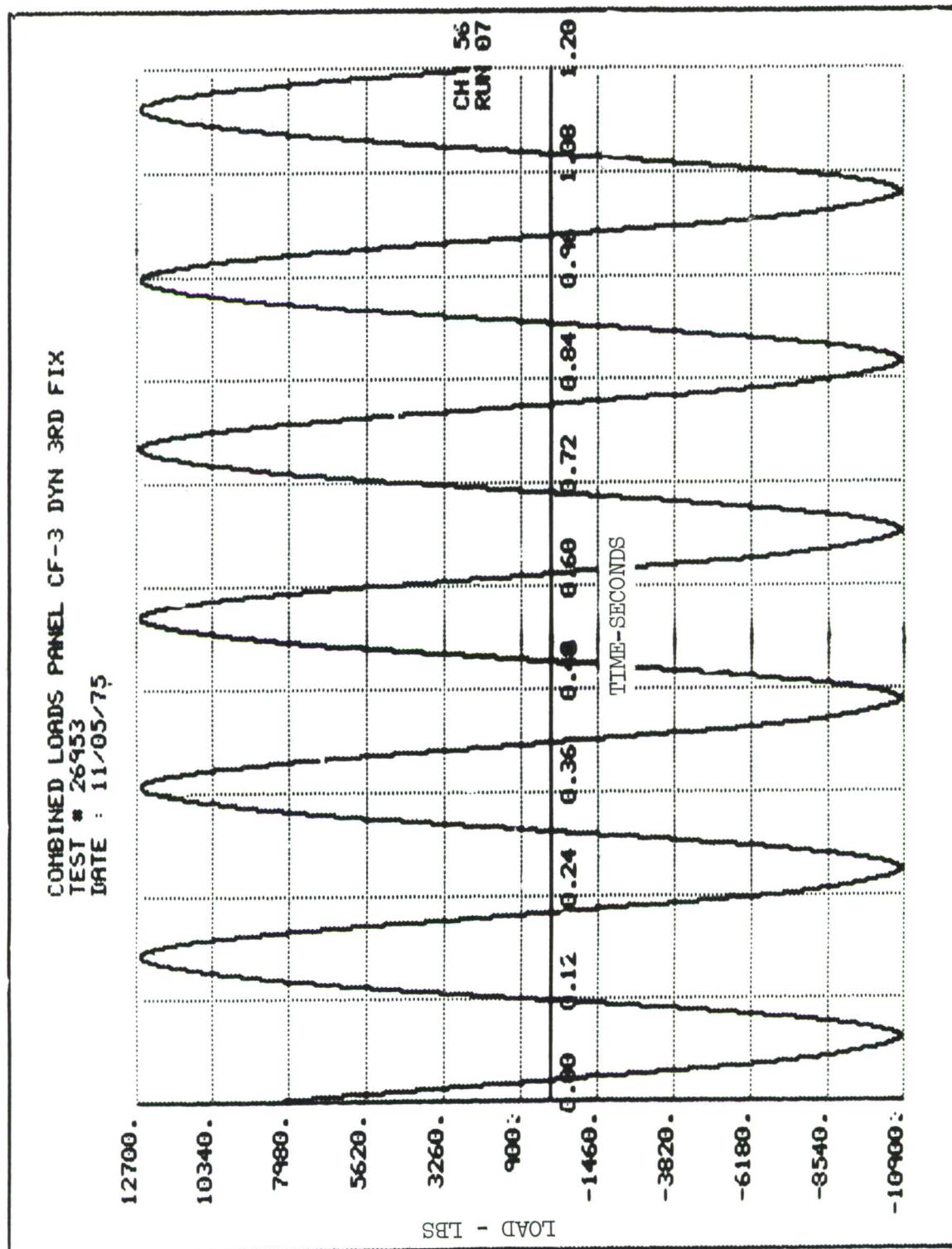


FIGURE 42. TYPICAL LOAD HISTORY DURING CYCLING

COMBINED LOADS PANEL CF-3 DYN 3RD FIX  
TEST # 26953  
DATE : 11/05/75

XMAX= 858.  
XMIN= -720.

YMAX= 12661.  
YMIN= -10833.

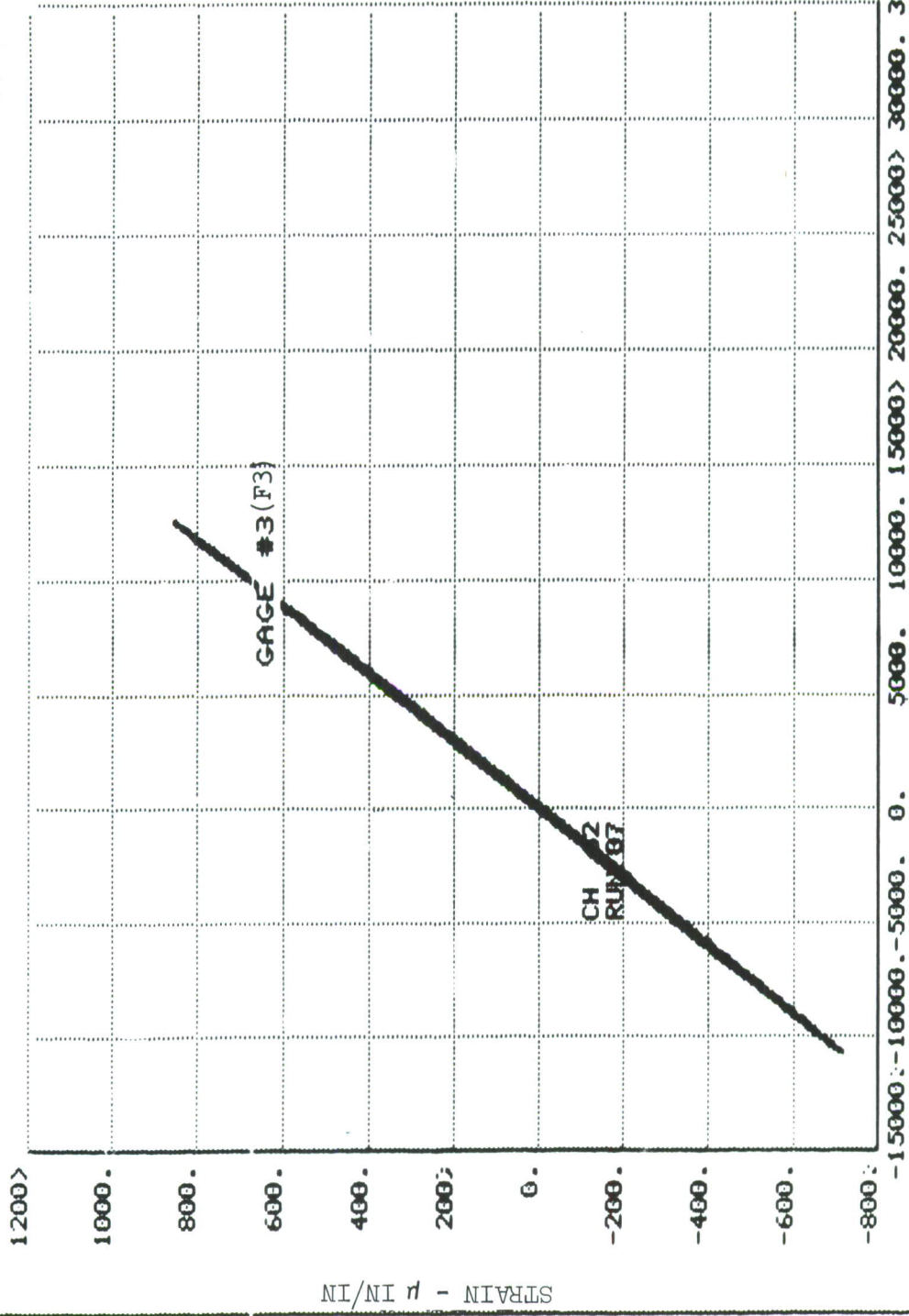


FIGURE 43. TYPICAL STRAIN LOAD PLOT DURING CYCLING

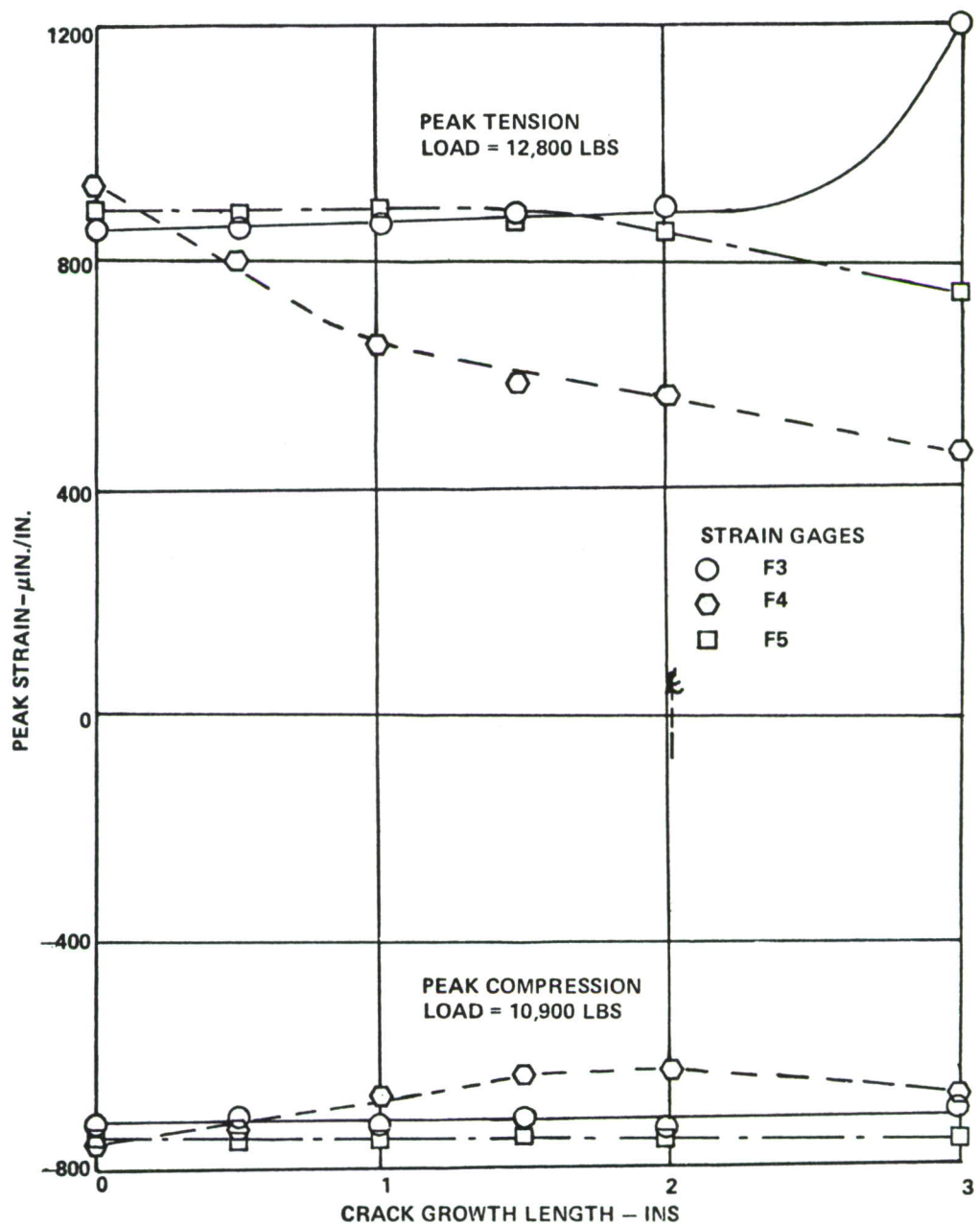


FIGURE 44. VARIATION OF PEAK AXIAL COMPRESSION AND TENSILE STRAIN WITH CRACK GROWTH LENGTH, PANEL CF3

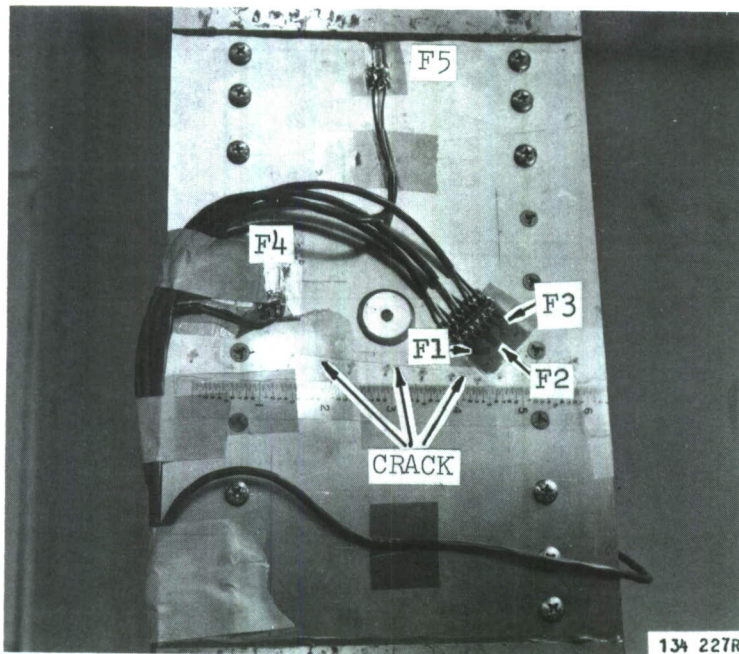


FIGURE 45. CRACK PROPAGATION IN TEST SPECIMEN CF3

CF3 is also included in Figure 47 to provide additional sampling for determining the degree of variability between test specimens resulting from inplane loads.

The variation of the panel frequency and damping with axial inplane load obtained from the free decay data is illustrated in Figures 48 and 49, respectively. Theoretically predicted panel frequency variation with in-plane load (equation 14), for two panel frequency parameter values of  $K = 1.48$  and  $1.35$ , is included in Figure 48. The variation of the panel edge rms strain with axial inplane load due to the shaker simulated acoustic loading is presented in Figure 50. All the panel edge strains are normalized to a panel edge strain (strain gage F1) of  $350 \mu \text{in/in}$  at zero inplane load corresponding to an rms force level typically around 35 to 38 pounds.

Typical panel strain histories due to the flight loads without acoustic excitation (Panel CF7) and with acoustic excitation (Panel CF9-2) are illustrated in Figures 51 and 52, respectively, for strain gage F1 for the same flight on the load tapes. The corresponding strain history for strain gage F3 on panel CF9-2, which is subjected to combined acoustic and flight loads, is shown in Figure 53. Typical narrow band spectral analyses of the combined acoustic and flight loads (no compression loads) strain histories are

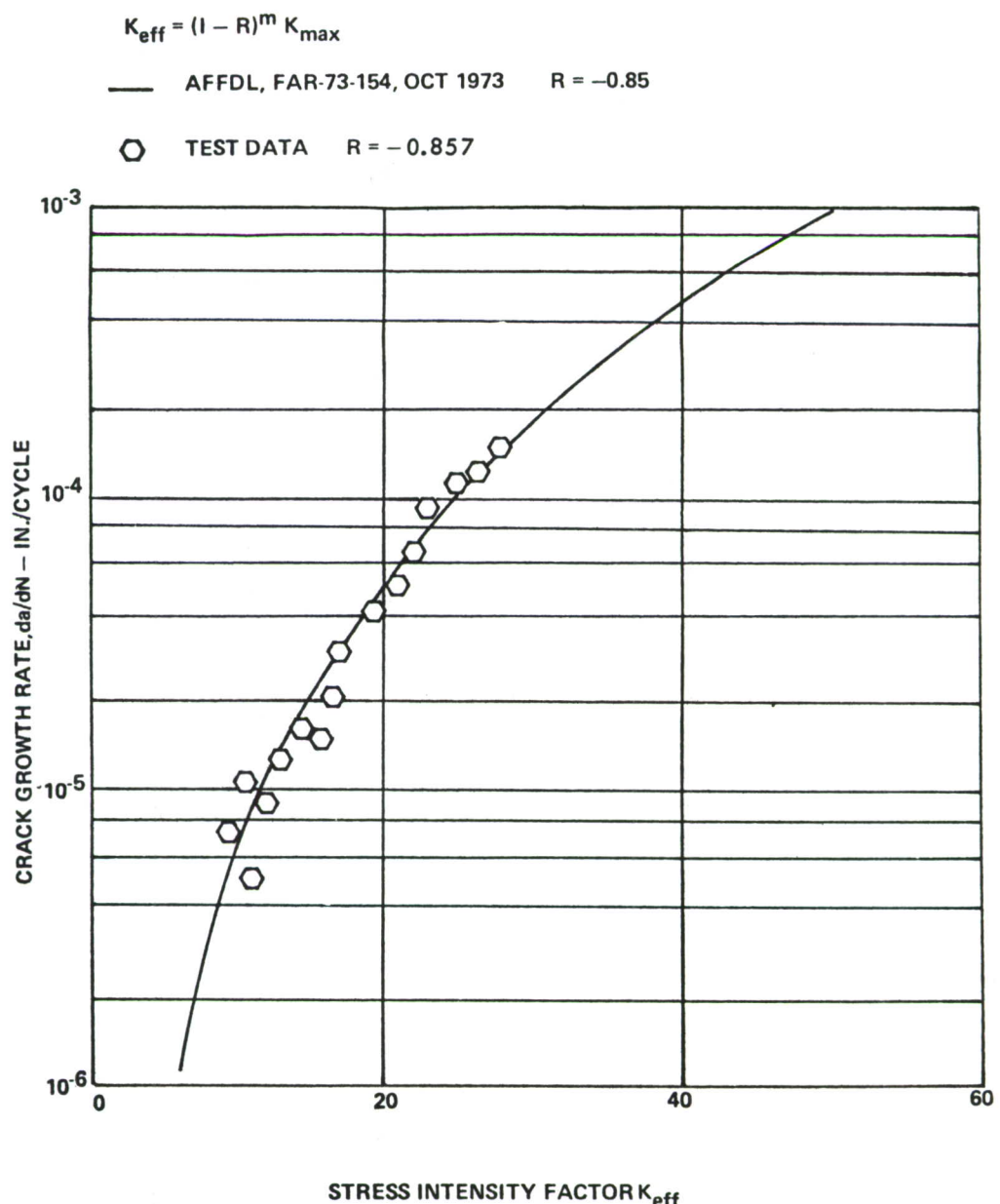


FIGURE 46. BASELINE CRACK GROWTH DATA, TEST SPECIMEN CF3

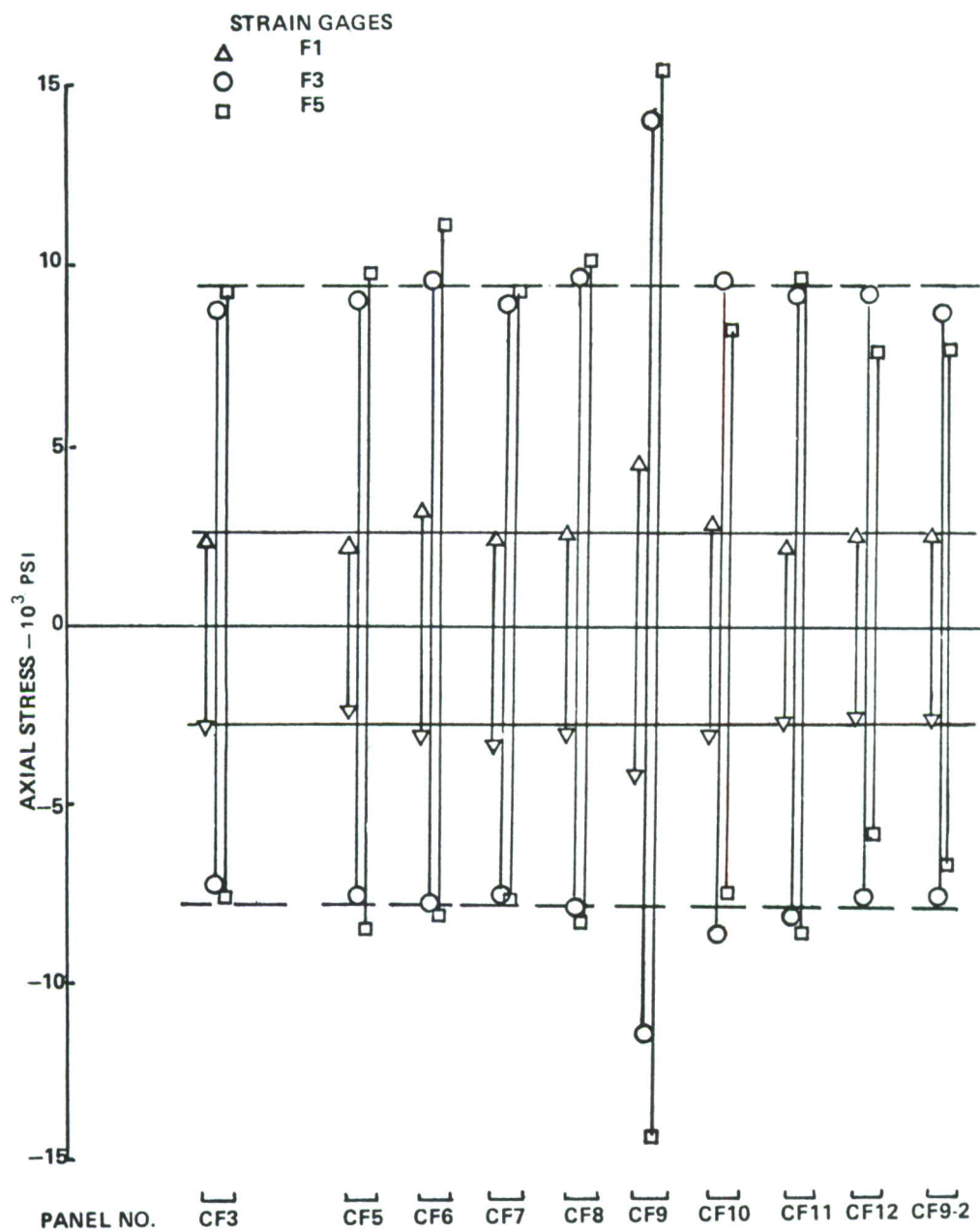


FIGURE 47. VARIATION IN PANEL PEAK STRESS BETWEEN TEST SPECIMENS DURING PRETEST CYCLING

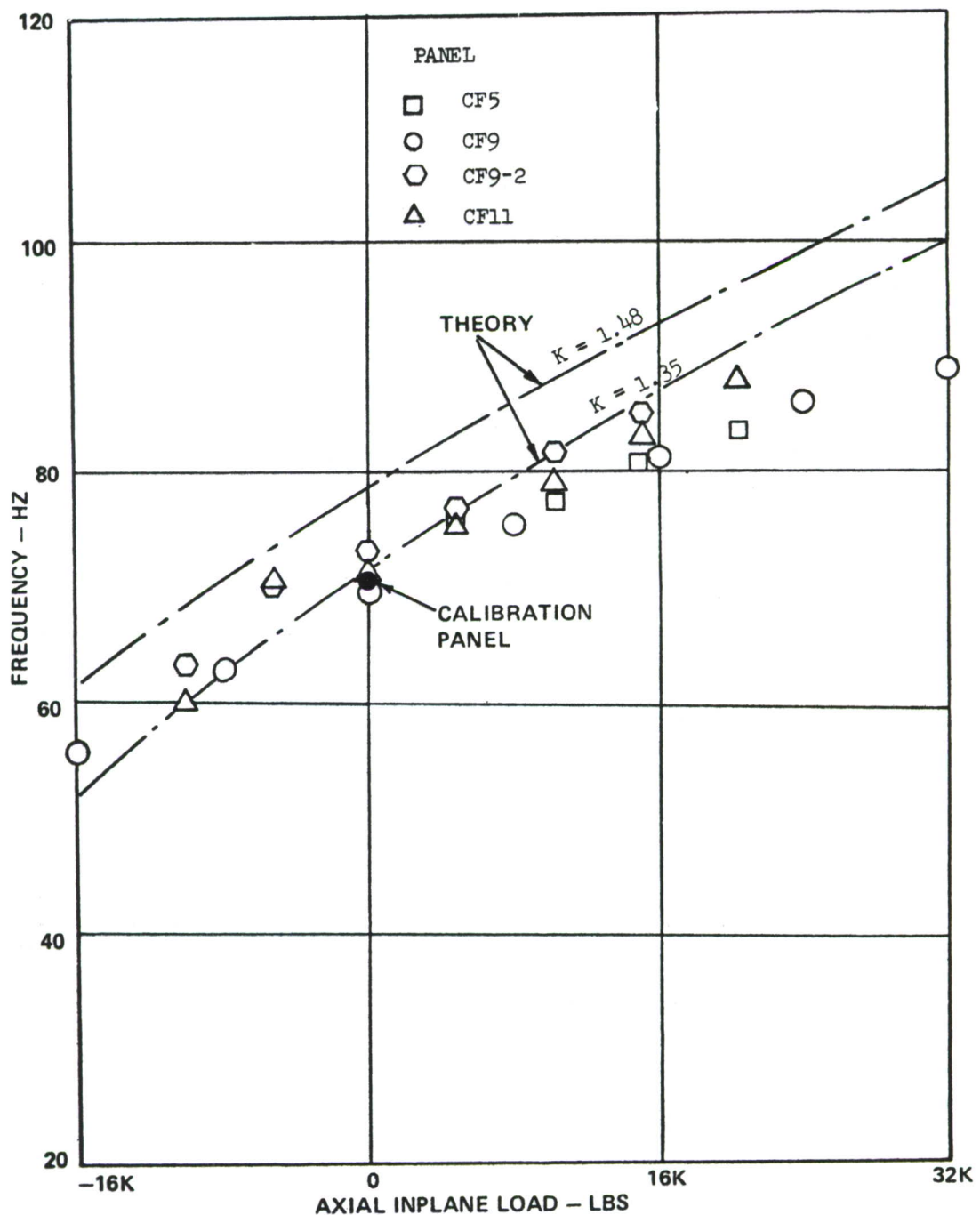


FIGURE 48. PANEL FUNDAMENTAL FREQUENCY AS A FUNCTION OF AXIAL INPLANE LOAD

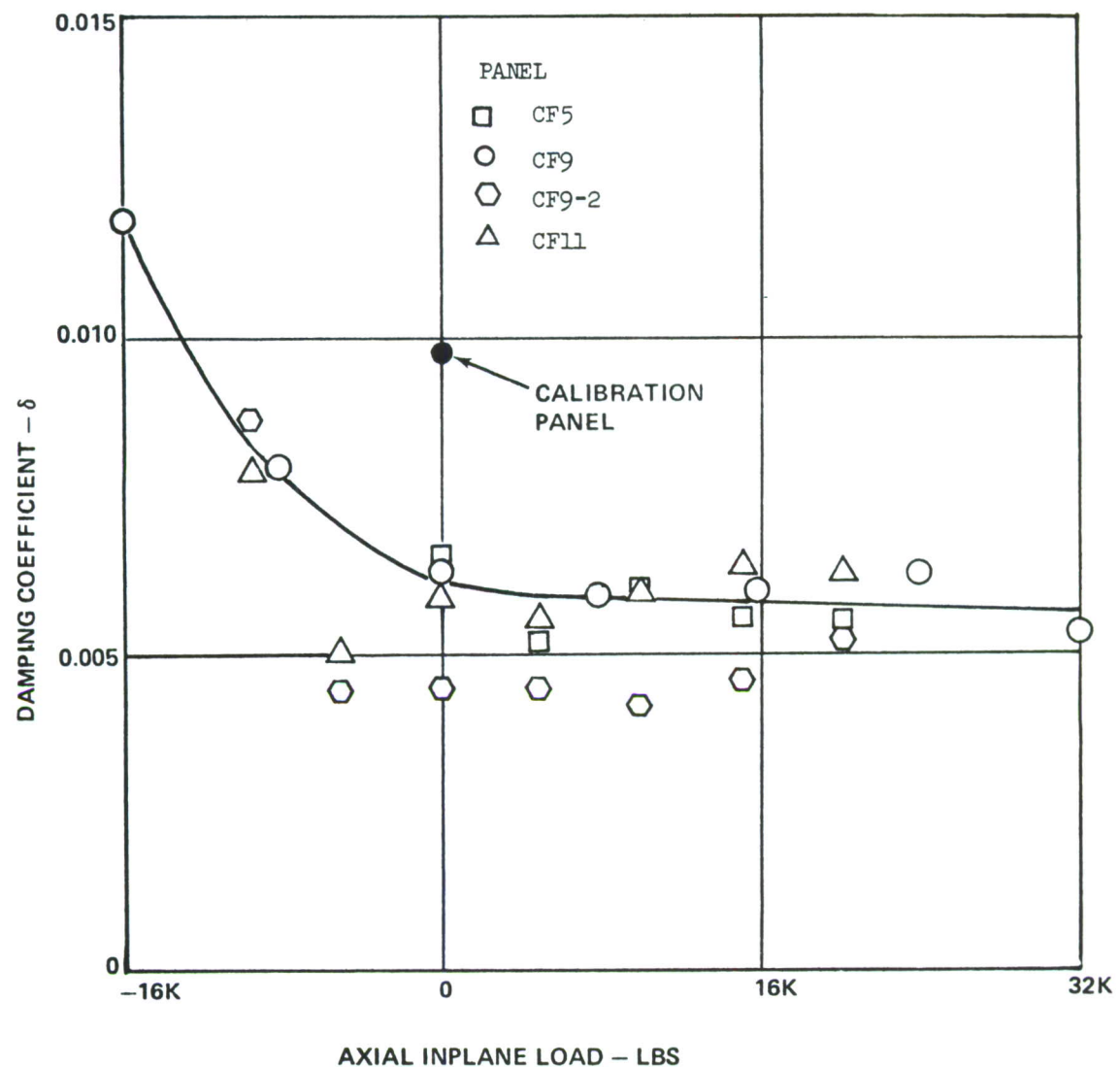


FIGURE 49. PANEL DAMPING COEFFICIENT AS A FUNCTION OF AXIAL INPLANE LOAD

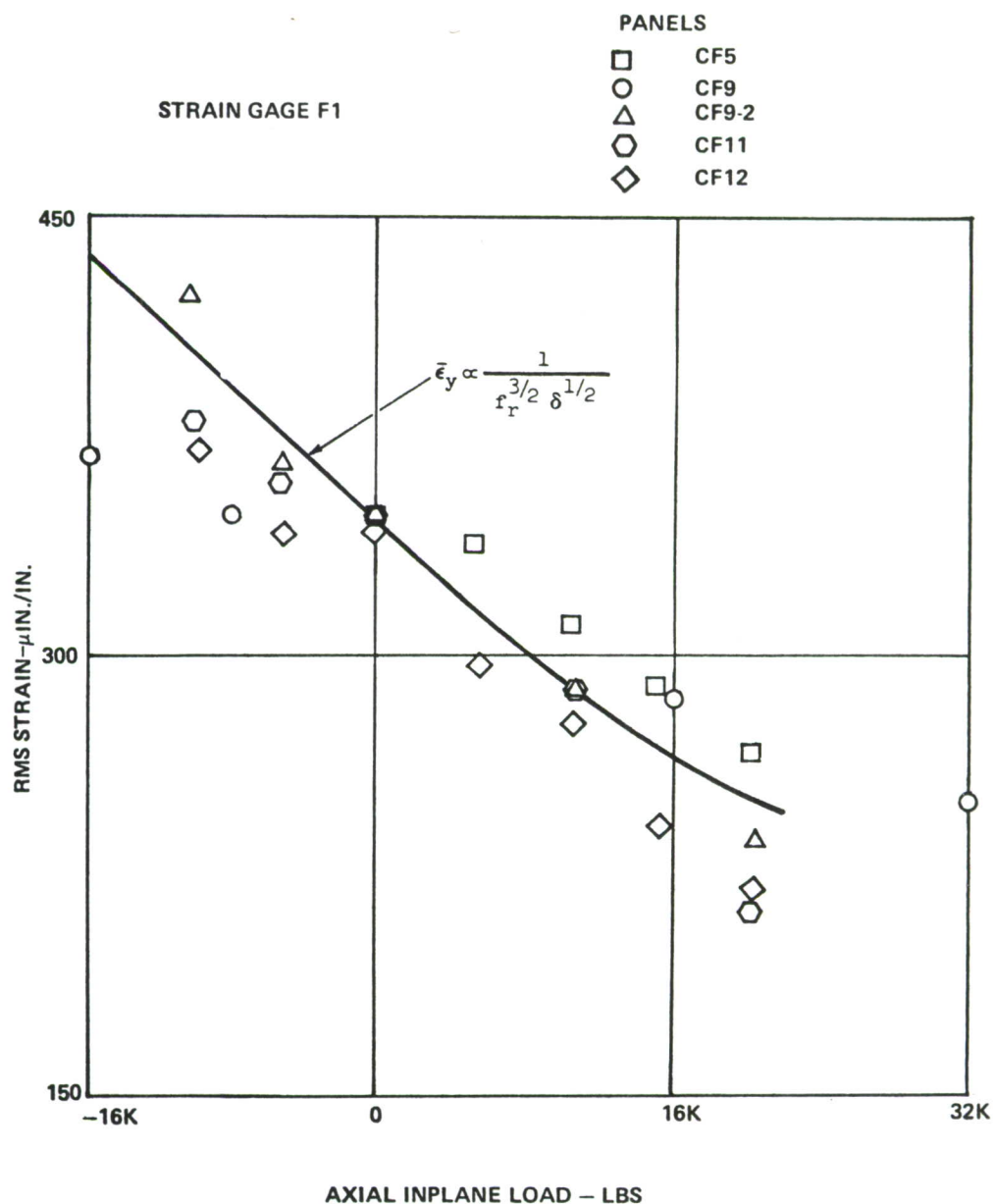


FIGURE 50. PANEL EDGE RMS STRAIN DUE TO SHAKER EXCITATION AS A FUNCTION OF AXIAL INPLANE LOAD

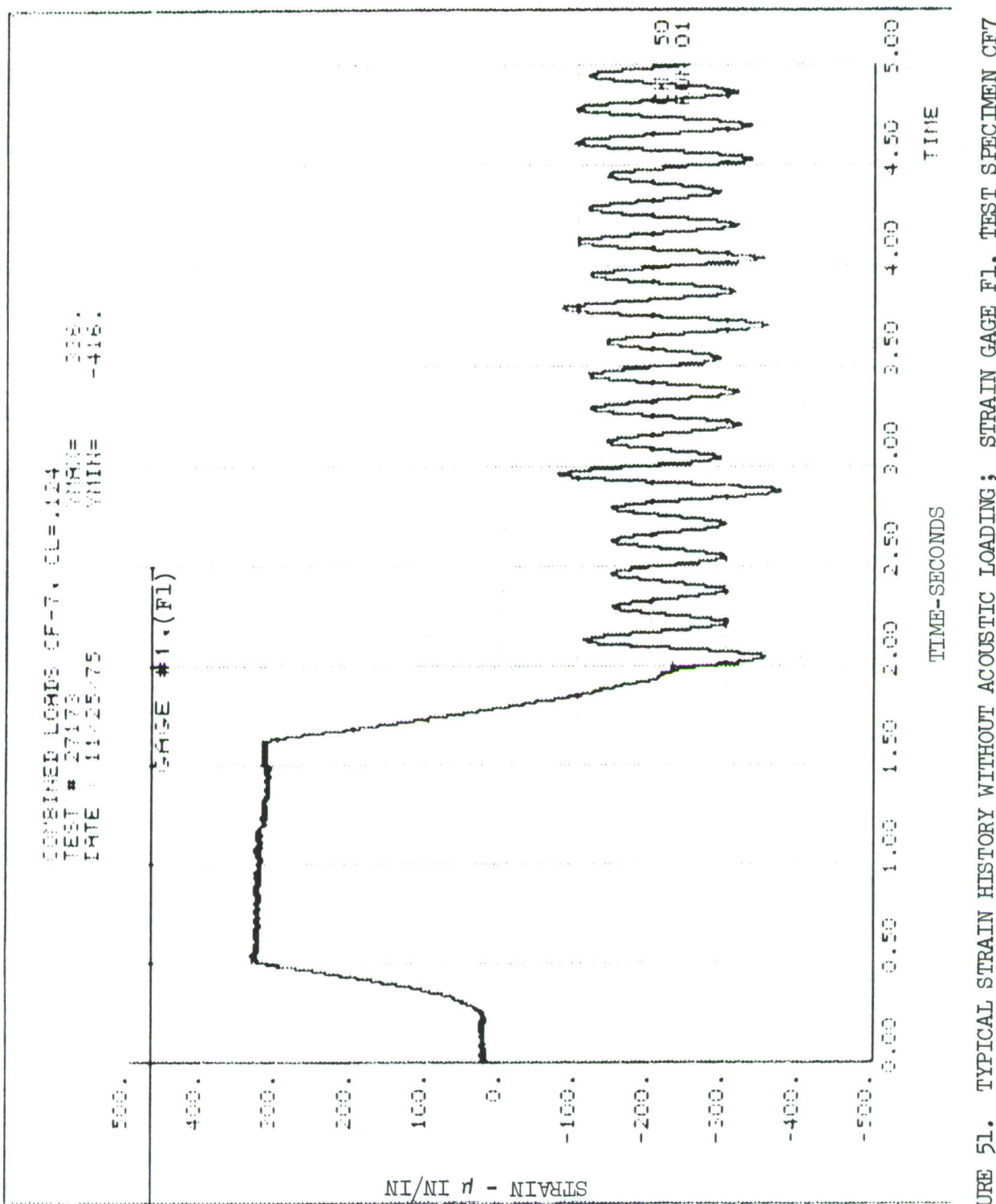
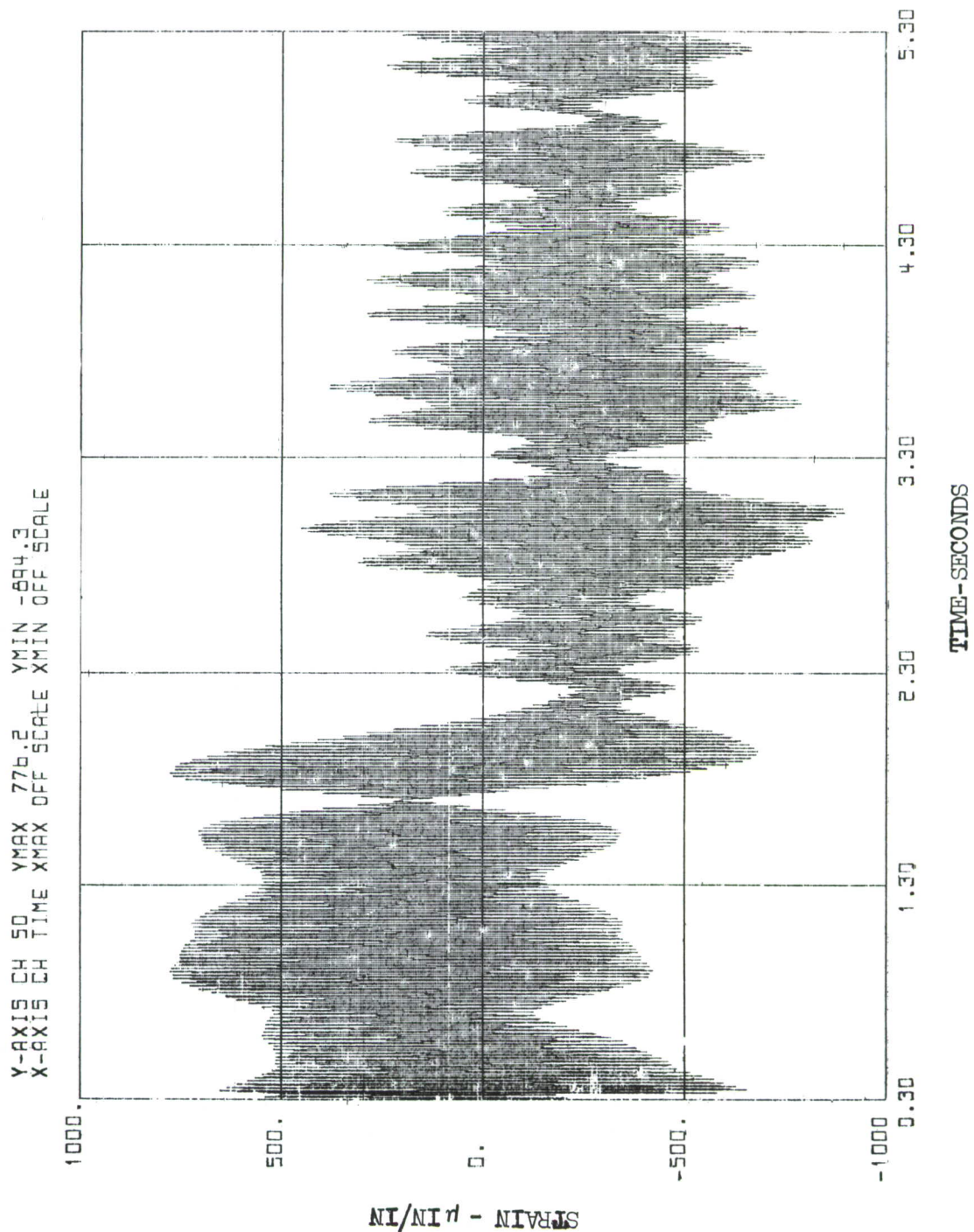


FIGURE 51. TYPICAL STRAIN HISTORY WITHOUT ACOUSTIC LOADING; STRAIN GAGE F1, TEST SPECIMEN CF7



CONB LOGS CF-9-2, TIME HIST FLT 23-25  
TEST # 27714  
DATE : 01/19/76

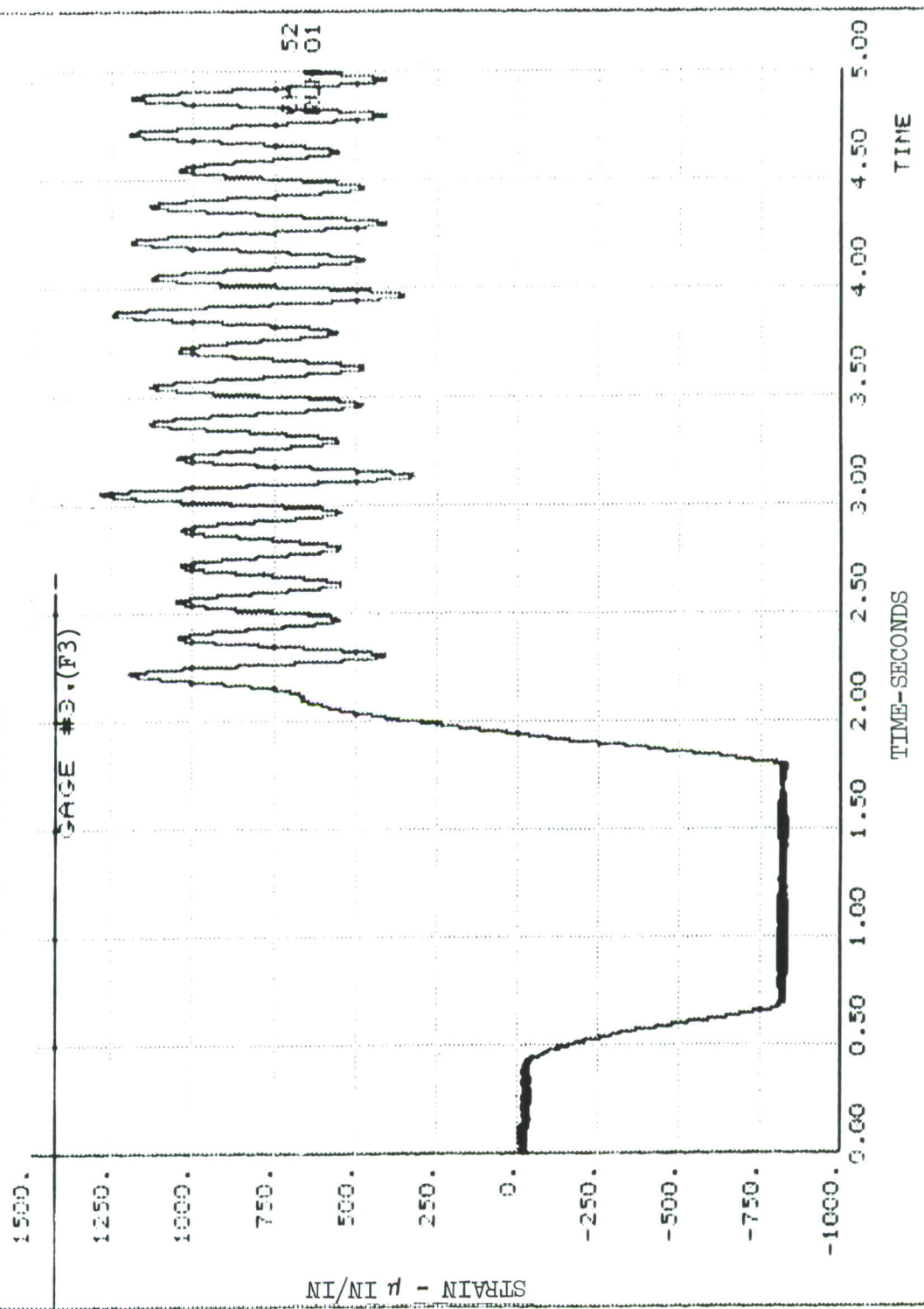


FIGURE 53. TYPICAL STRAIN HISTORY WITH ACOUSTIC LOADING; STRAIN GAGE F3, TEST SPECIMEN CF9-2

illustrated in Figures 54 through 56.

A summary of the crack propagation test results is presented in Table 14. The initial crack length is measured from the fastener edge to the crack tip after the crack initiation cycling and other tests are completed. Typical crack propagation patterns are illustrated in Figures 57 through 61. Figures 57 (Panel CF7) and 58 (Panel CF11) represent the crack patterns for the upper wing surface flight loads without and with the acoustic loading, respectively. Crack branching is observed on panel CF11. The combined acoustic and lower wing surface flight load induced crack is illustrated in Figure 59 for panel CF12. Figures 60 (Panel CF5) and 61 (Panel CF6) show the crack path for the combined acoustic, tension and upper and lower surface spectral loads (without compression load), respectively. Crack branching is again observed in panel CF5. On two test panels, CF9-2 and CF11, a crack was initiated at the shaker drive hole. The cracks propagated to the opposite side of the panels to the precrack as illustrated in Figure 62 for panel CF11.

As indicated in Table 14, all crack faces are essentially normal to the panel surface except for test panels CF8, CF10 and CF12 where crack face inclination is observed. The crack face inclination in panel CF10, relative to the normal to the panel surface, started immediately from the precrack tip. However, the crack inclination in panels CF8 and CF12, did not occur until the crack had propagated to the stiffener edge.

The crack growth data, in terms of the crack growth rate per flight as a function of crack length, is shown in Figure 63 for test panel CF5 and Figure 64 for test panels CF7, CF9-2, and CF11 for the upper wing surface loads. The corresponding crack growth data for the lower wing surface loads is given in Figure 65 for test panel CF6 and in Figure 66 for test panels CF8, CF10 and CF12. Test panel CF9 crack propagation data is also included in Figure 66 since the actual panel stresses are comparable to those encountered in the panels subjected to the lower wing surface loads.

Fatigue cracks occurred also in the frame flanges adjacent to the pre-cracks on all the test specimens. These frame cracks are summarized schematically in Figure 67.

**3.5.3 Simulated Acoustic Loads** - Two test specimens were used in the simulated acoustic crack growth tests and were mounted in the 220,000 pound MTS fatigue machine. Test specimen CF2 was subjected to only shaker simulated acoustic loading. Test specimen CF4 was subjected to combined compression and simulated acoustic loads.

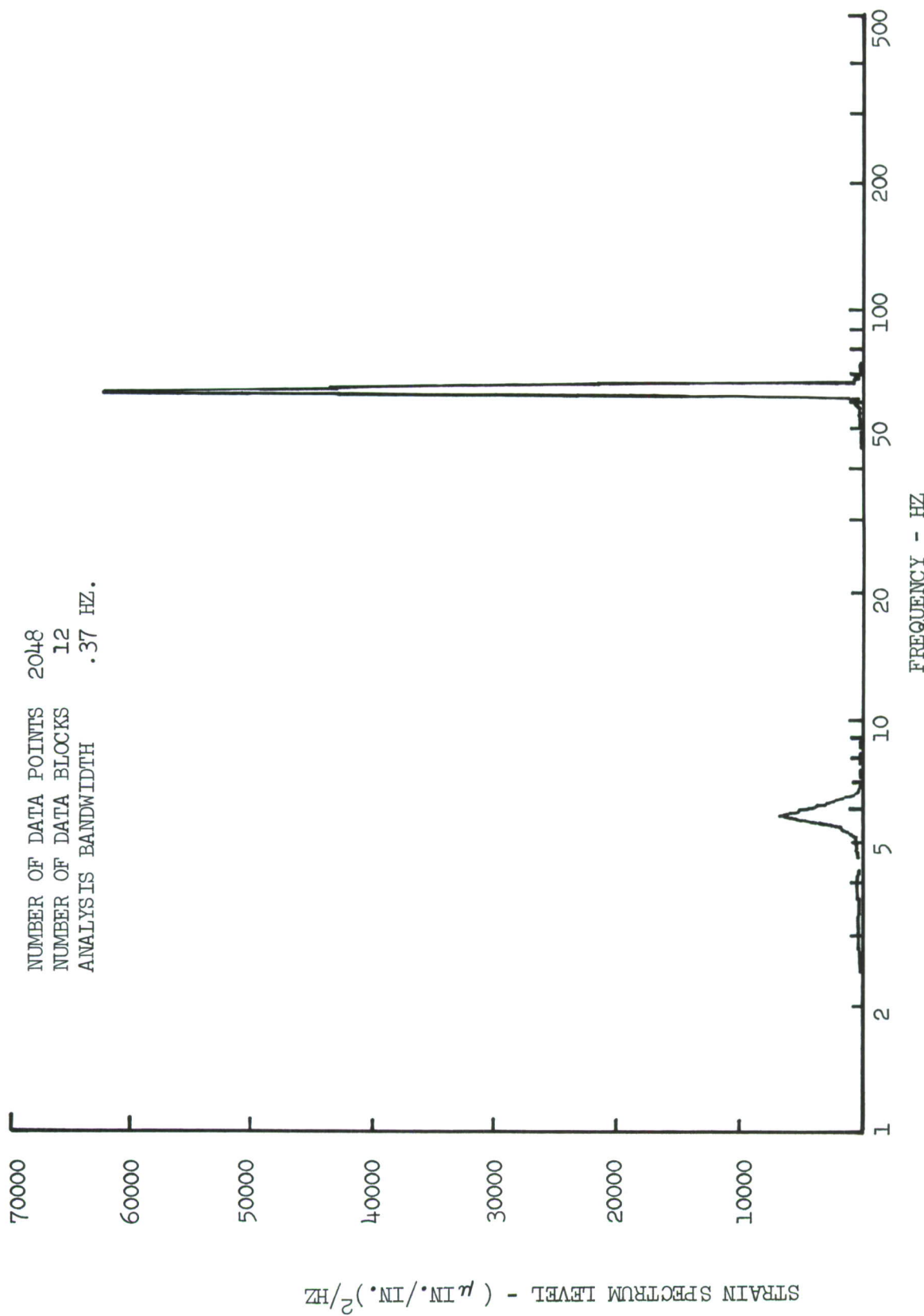


FIGURE 54. NARROW BAND SPECTRAL ANALYSIS OF STRAIN GAGE F1, TEST SPECIMEN CF5

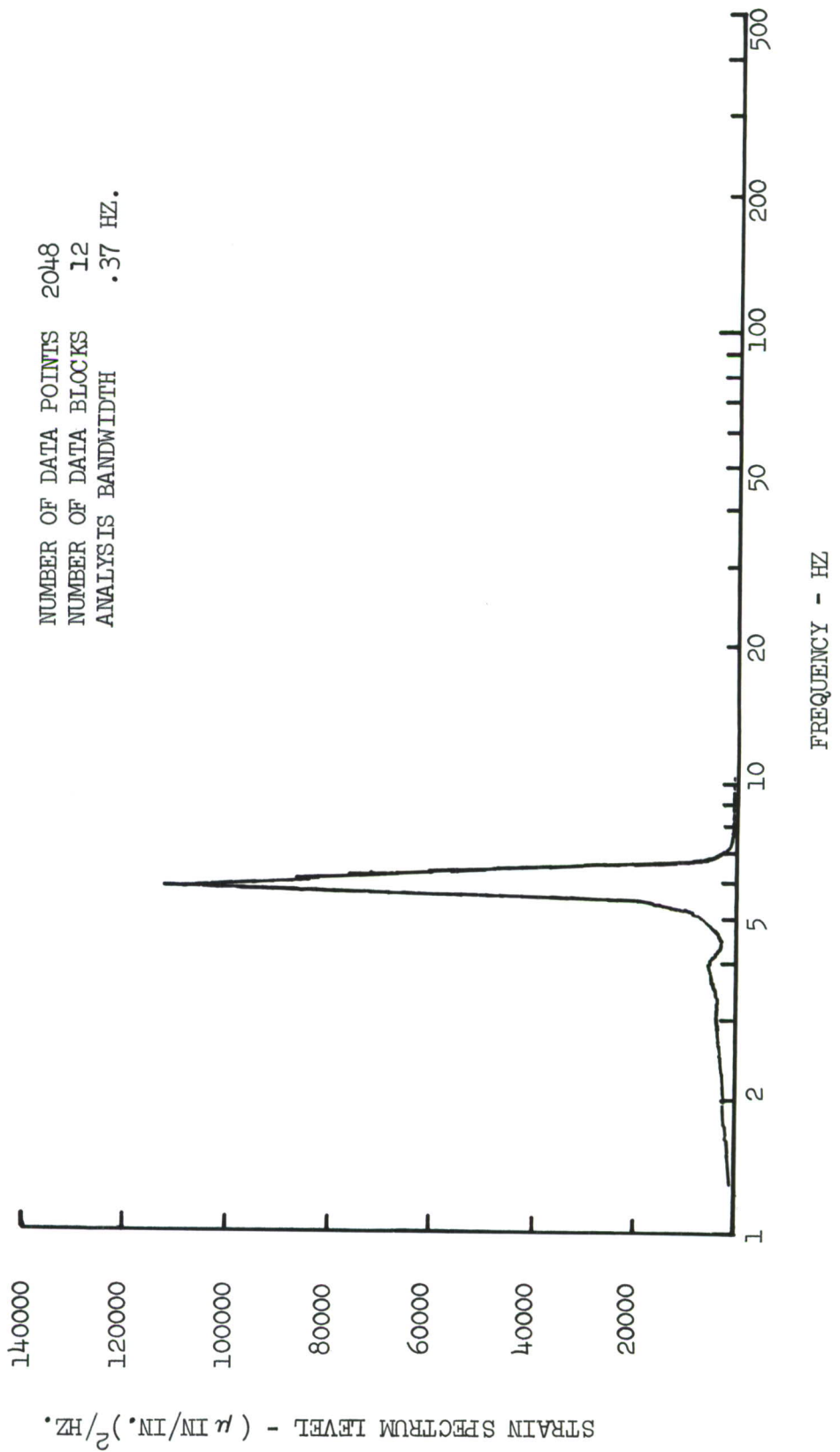


FIGURE 55. NARROW BAND SPECTRAL ANALYSIS OF STRAIN GAGE F3, TEST SPECIMEN CF5

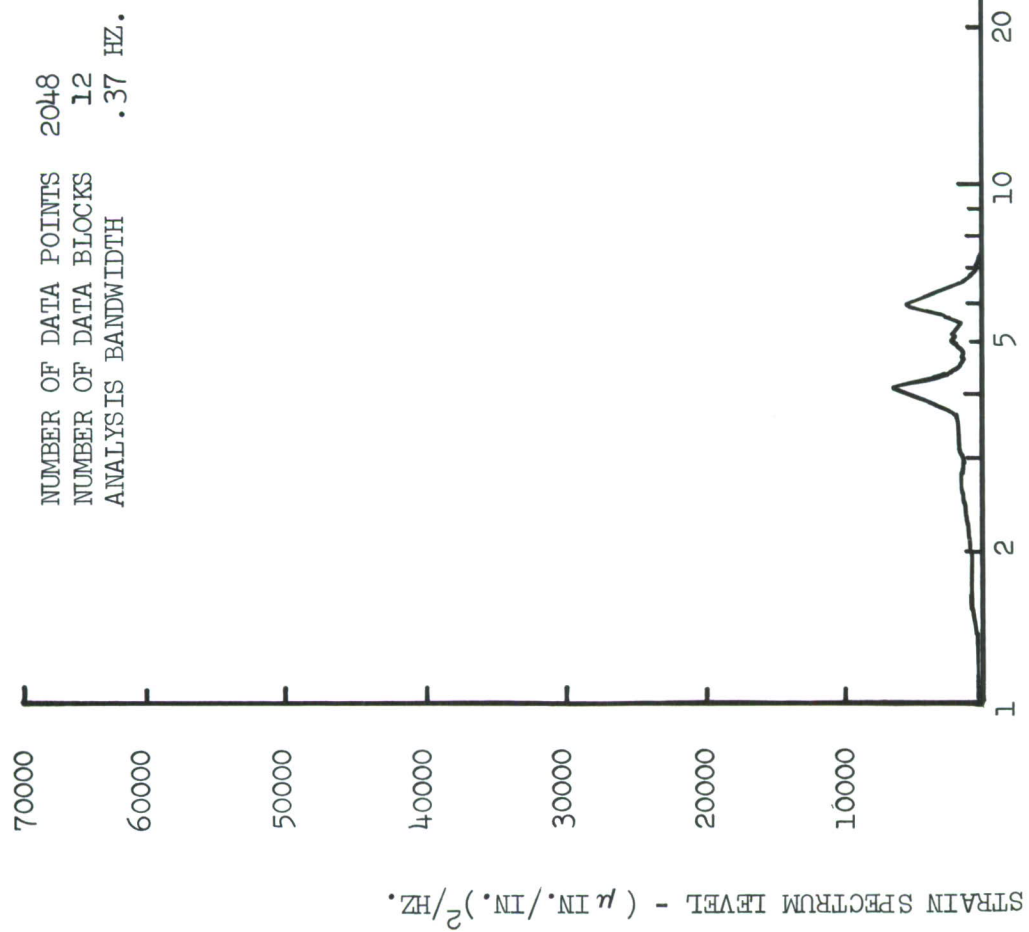


FIGURE 56. NARROW BAND SPECTRAL ANALYSIS OF STRAIN GAGE F1, TEST SPECIMEN CFG

TABLE 14. SUMMARY OF FLIGHT-BY-FLIGHT AND COMBINED LOADS CRACK PROPAGATION DATA

WING SURFACE	TEST PANEL	INITIAL CRACK LENGTH *	FINAL CRACK LENGTH *	NUMBER OF FLIGHTS	CRACK PATH
UPPER	CF5	0.104	0.832	4611	Two initial cracks with subsequent branching
	CF7	0.094	0.80	3853	Single Crack
	CF9-2	0.133	0.872	2516	Single crack on surface, branching underneath stiffener
	CF11	0.126	0.861	2377	Two initial cracks and crack branching
	CF9	0.116	0.805	1145	Single crack
LOWER	CF6	0.097	0.816	1293	Single crack
	CF8	0.106	0.863	1053	Single crack **
	CF10	0.10	0.840	1252	Single crack **
	CF12	0.107	0.912	1006	Single crack **

\* Inches

\*\* Crack face inclined relative to panel surface. The crack face on all other test panels is approximately normal to the panel surface.

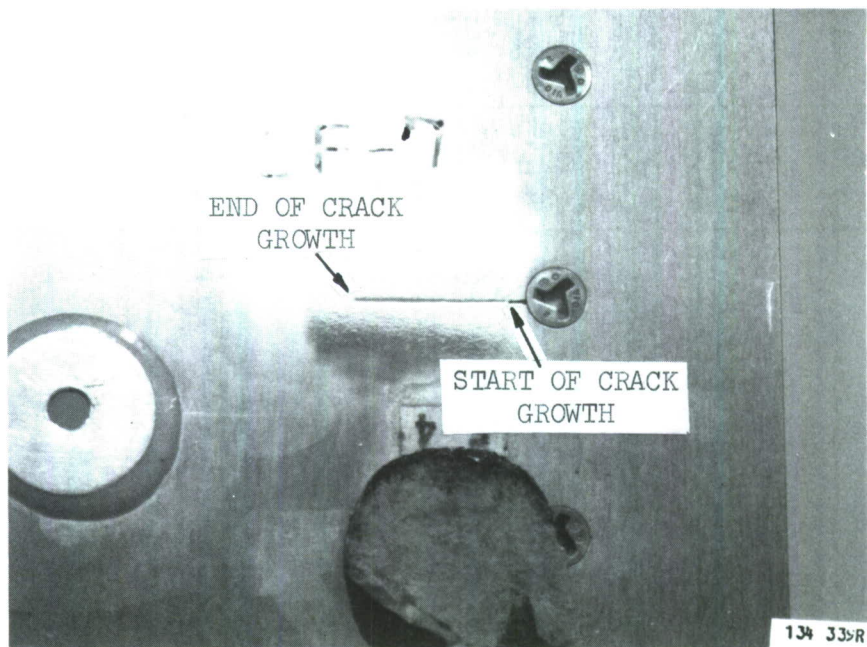


FIGURE 57. TYPICAL CRACK FROM UPPER WING SURFACE FLIGHT LOADS, TEST SPECIMEN CF 7

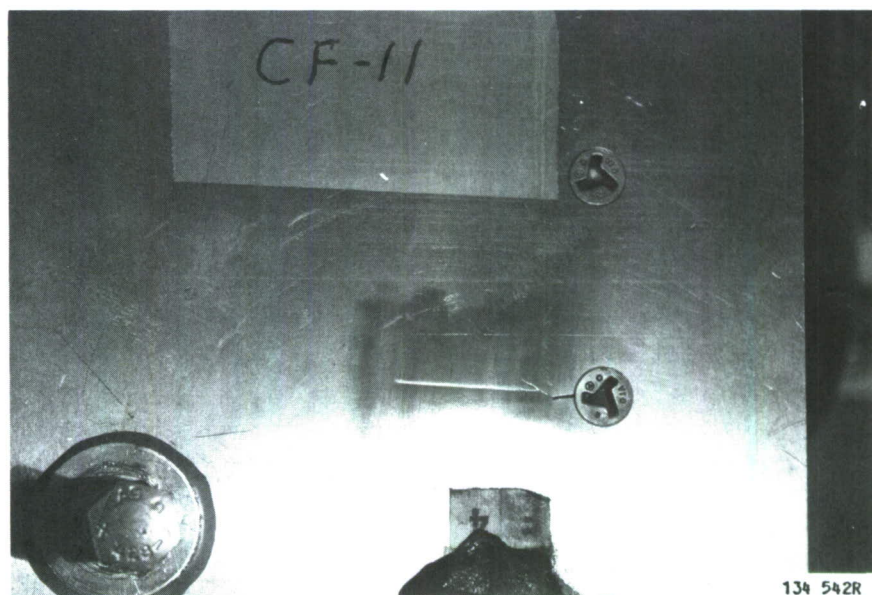


FIGURE 58. TYPICAL CRACK FROM COMBINED UPPER WING SURFACE FLIGHT LOADS AND SIMULATED ACOUSTIC LOADS, TEST SPECIMEN CF 11

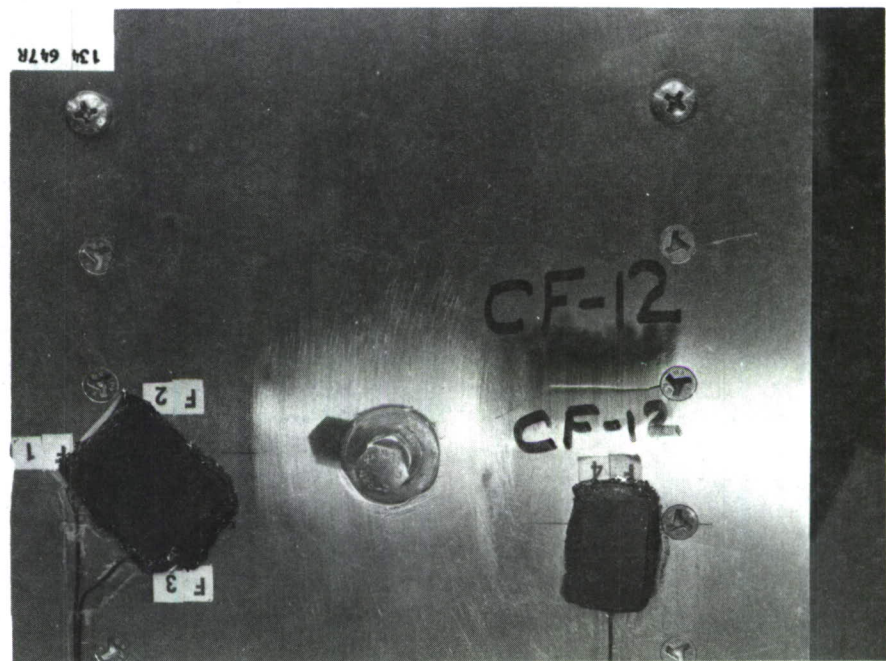


FIGURE 59. TYPICAL CRACK FROM COMBINED LOWER WING SURFACE FLIGHT LOADS AND SIMULATED ACOUSTIC LOADS, TEST SPECIMEN CF 12

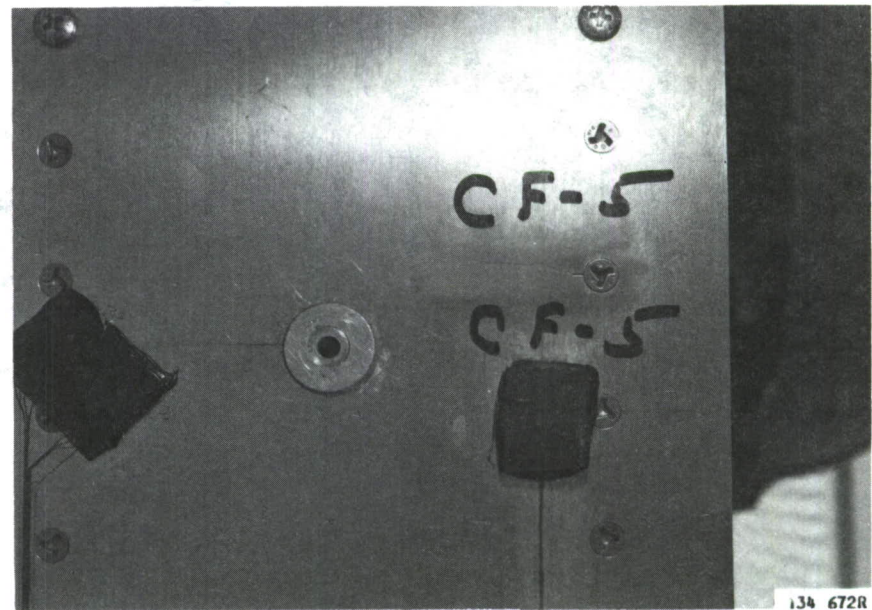


FIGURE 60. TYPICAL CRACK FROM COMBINED UPPER WING SPECTRAL, TENSION AND SIMULATED ACOUSTIC LOADS, TEST SPECIMEN CF 5

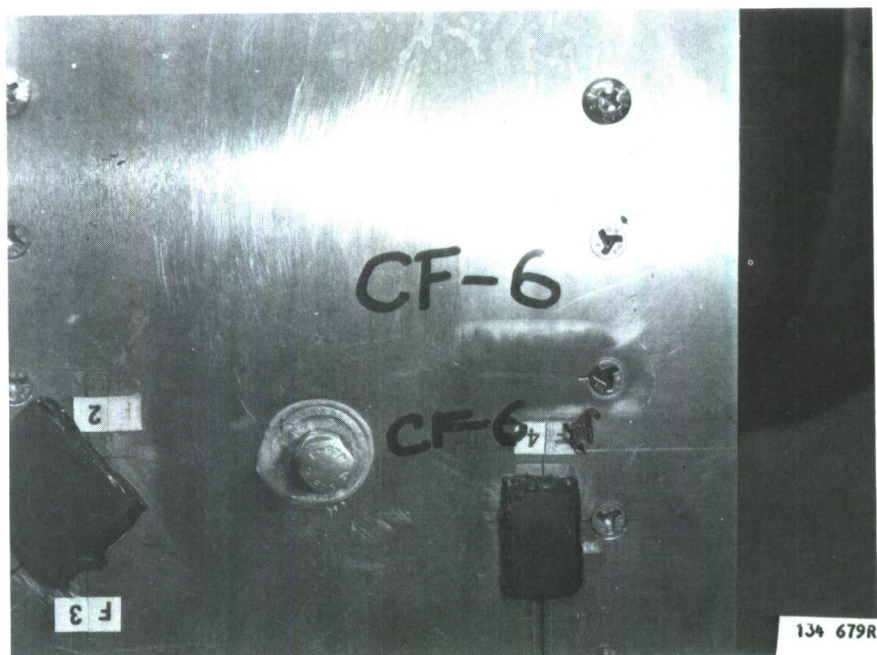


FIGURE 61. TYPICAL CRACK FROM COMBINED LOWER WING SPECTRAL, TENSION AND SIMULATED ACOUSTIC LOADS, TEST SPECIMEN CF6

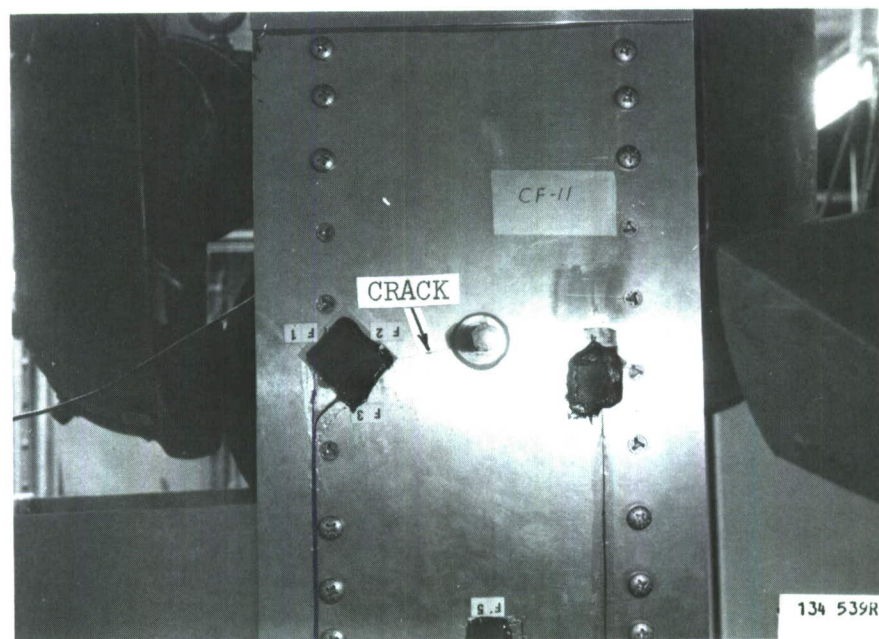


FIGURE 62. CRACK FROM SHAKER DRIVE ROD HOLE, TEST SPECIMEN CF11

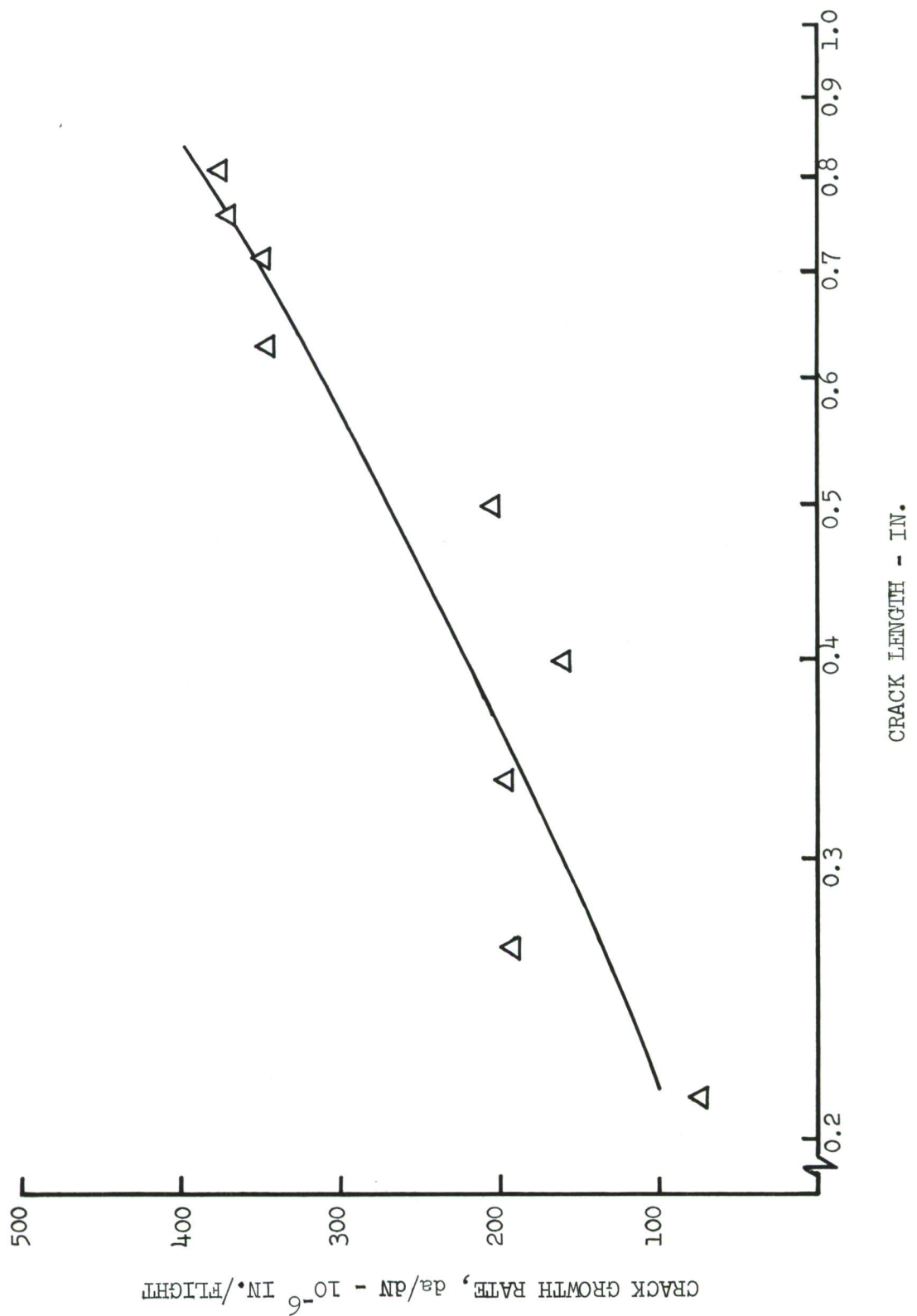


FIGURE 63. MEASURED CRACK GROWTH RATE DATA, TEST SPECIMEN CF5

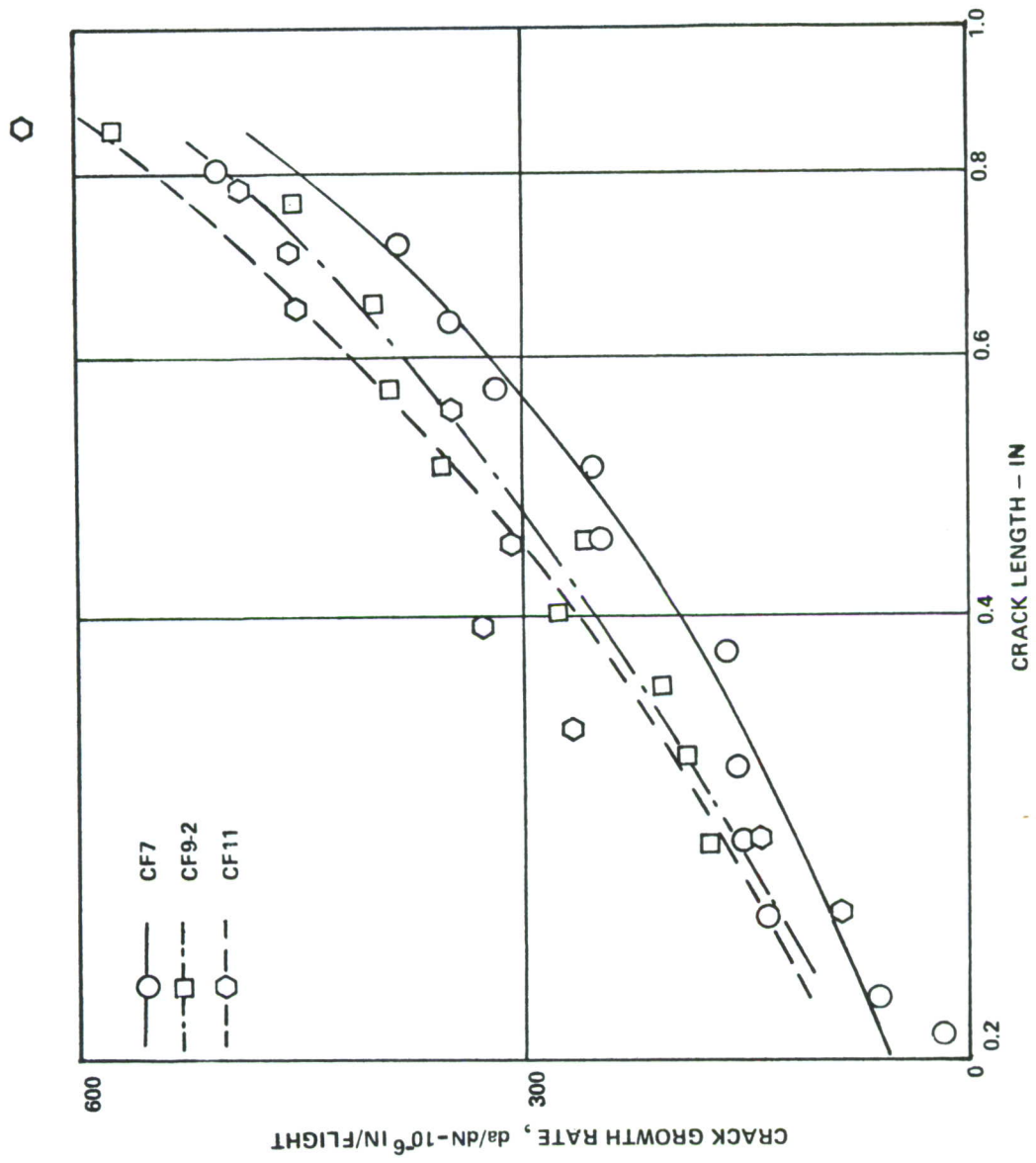


FIGURE 64. MEASURED CRACK GROWTH RATE DATA, UPPER WING SURFACE LOADS

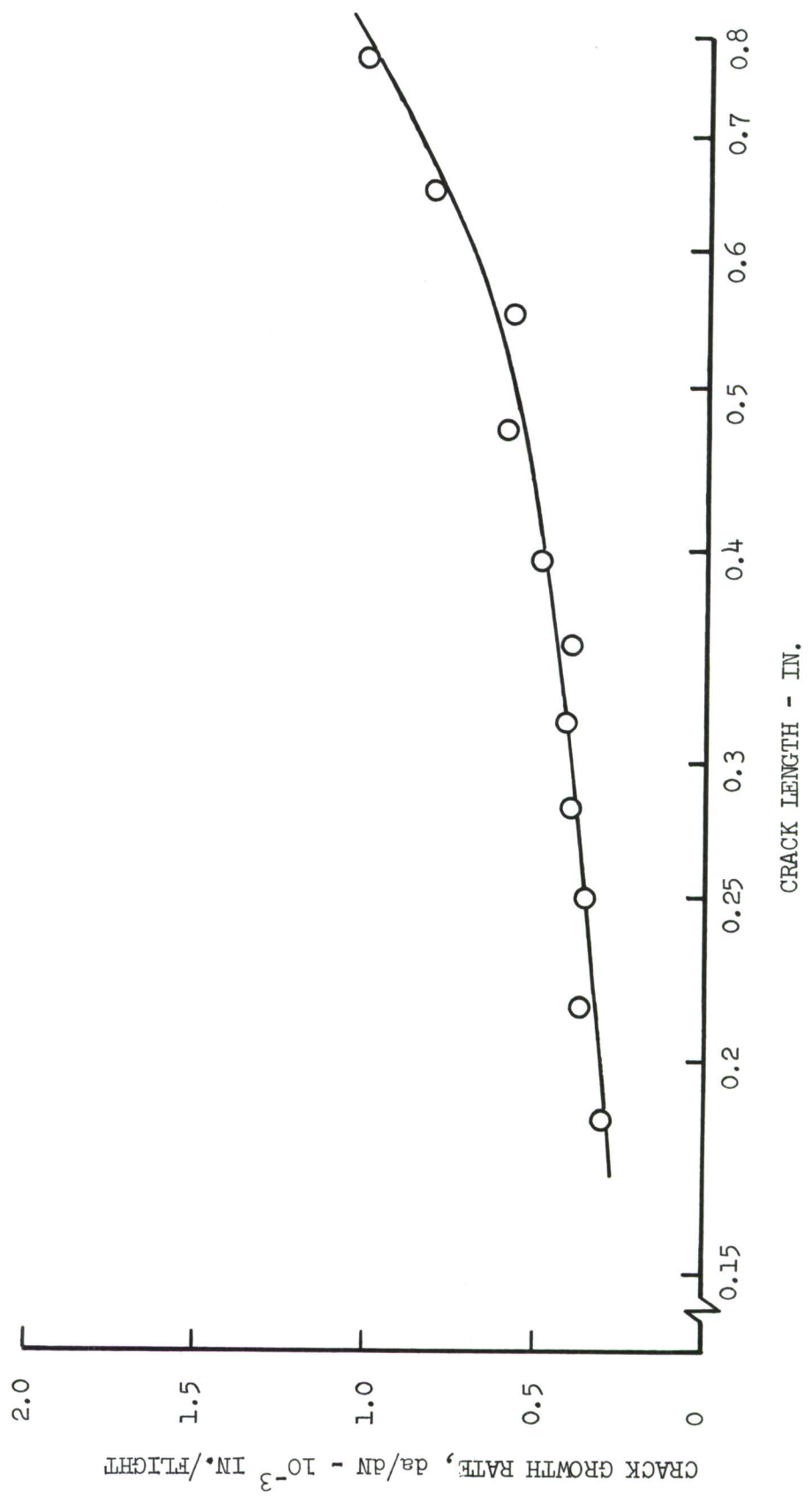


FIGURE 65. MEASURED CRACK GROWTH RATE DATA, TEST SPECIMEN CF6

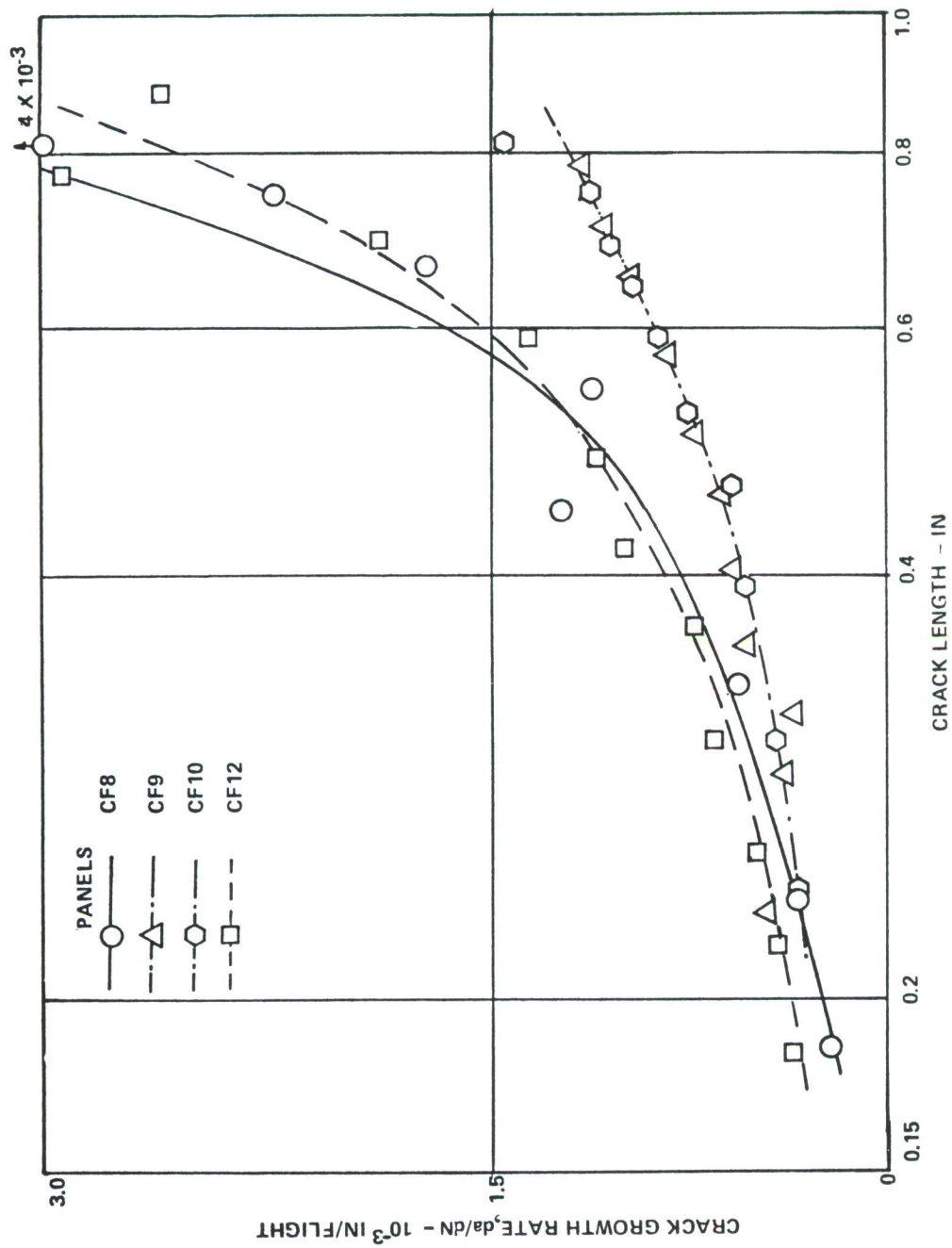


FIGURE 66. MEASURED CRACK GROWTH RATE DATA, LOWER WING SURFACE LOADS

TEST SPECIMEN



CF5



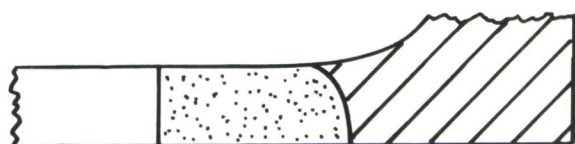
CF6



CF7



CF8



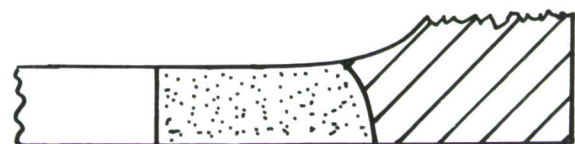
CF9



CF9-2



CF10



CF11



CF12

10.1"  
Scale

FIGURE 67. FRAME CRACKS ADJACENT TO PANEL PRECRACKS

The resonant frequency and damping coefficient measured from the free decay tests for test specimen CF2 are 71.4 Hz and 0.0069, respectively. Two shaker force levels, corresponding to panel rms edge strains of 350 and 450  $\mu$  in/in, were used in this crack propagation test. The acoustic type panel edge crack (Figure 68) propagated a total of 0.07 inches in  $7.5 \times 10^6$  cycles by the end of the test. The test was stopped after a panel center crack developed from the edge of the center circular doubler nearest to the panel side (Figure 69). The crack propagated approximately parallel to the panel edge in both directions. The panel center crack propagated much faster than the panel edge crack, both initiating and reaching a length of approximately two inches in the above number of cycles. No crack propagation was obtained from the flight load type crack normal to the rivet line. The rivet line acoustic crack propagation data is presented in Figure 70 in terms of the crack growth rate as a function of the rms stress intensity factor.

The resonant frequencies of 61.5 and 40.15 Hz and the corresponding damping coefficients 0.007 and 0.032 were measured from the free decays of panel CF4 at zero and 5000 pound compression load, respectively. The free decay at 10,750 pound compression load indicated very high damping. The panel edge rms strain (strain gage F1), initially set at 350  $\mu$  in/in at zero load, increased to 440 and 450  $\mu$  in/in at compression loads of 5000 and 9000 pounds, respectively. Unusually large panel amplitudes were obtained at a compression load of 10,750 pounds. As a consequence, the compression load was reduced until the large amplitudes abated. Crack growth tests at a compression load of 9000 pounds at a panel edge strain of 445  $\mu$  in/in resulted in a slow panel edge crack growth (Figure 70) from the acoustic crack. However, a very rapid panel center crack growth, in opposite directions along the longitudinal centerline of the panel from the edge of the circular panel center doublers was obtained. The panel edge crack grew 0.062 inches while the panel center crack both initiated and grew 2.9 inches in  $0.68 \times 10^6$  cycles, causing the panel to buckle. The crack growth test was stopped at this point. No crack propagation was obtained from the flight load crack.

### 3.6 Discussion of Test Results

**3.6.1 Baseline Tests** - The essentially linear compression load strain curves indicated that panel buckling would not be encountered within the test load range. In general, the load strain data from the 5 Hz cycling provided more consistent results than the static test.

The strain data obtained from the strain gage rosette (strain gages F1, F2 and F3) during the cycling indicated that a near plane stress state has been achieved within the test panel. The principal stress axis is inclined at approximately 1.5 degrees relative to the longitudinal centerline which could partially explain the downward slope of the crack propagation path

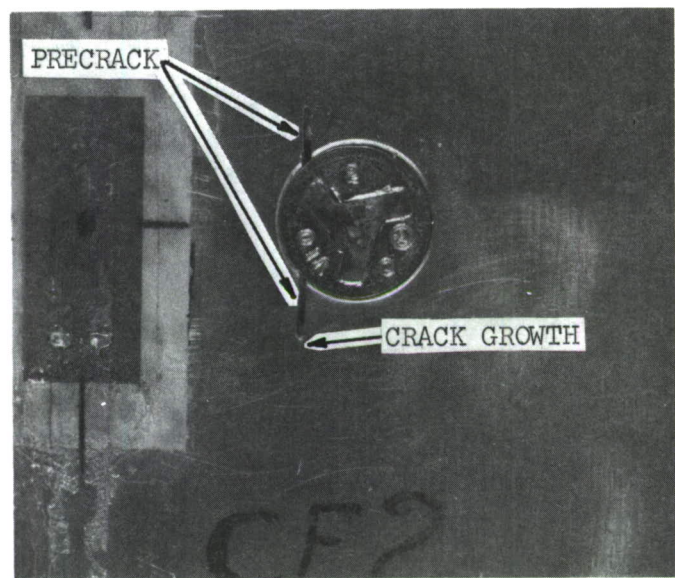


FIGURE 68. ACOUSTIC PANEL EDGE CRACK, TEST SPECIMEN CF2

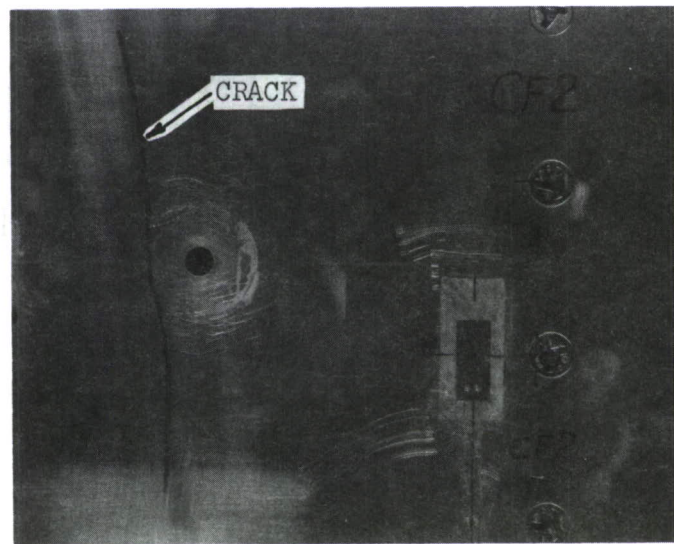


FIGURE 69. PANEL CENTER CRACK, TEST SPECIMEN CF2

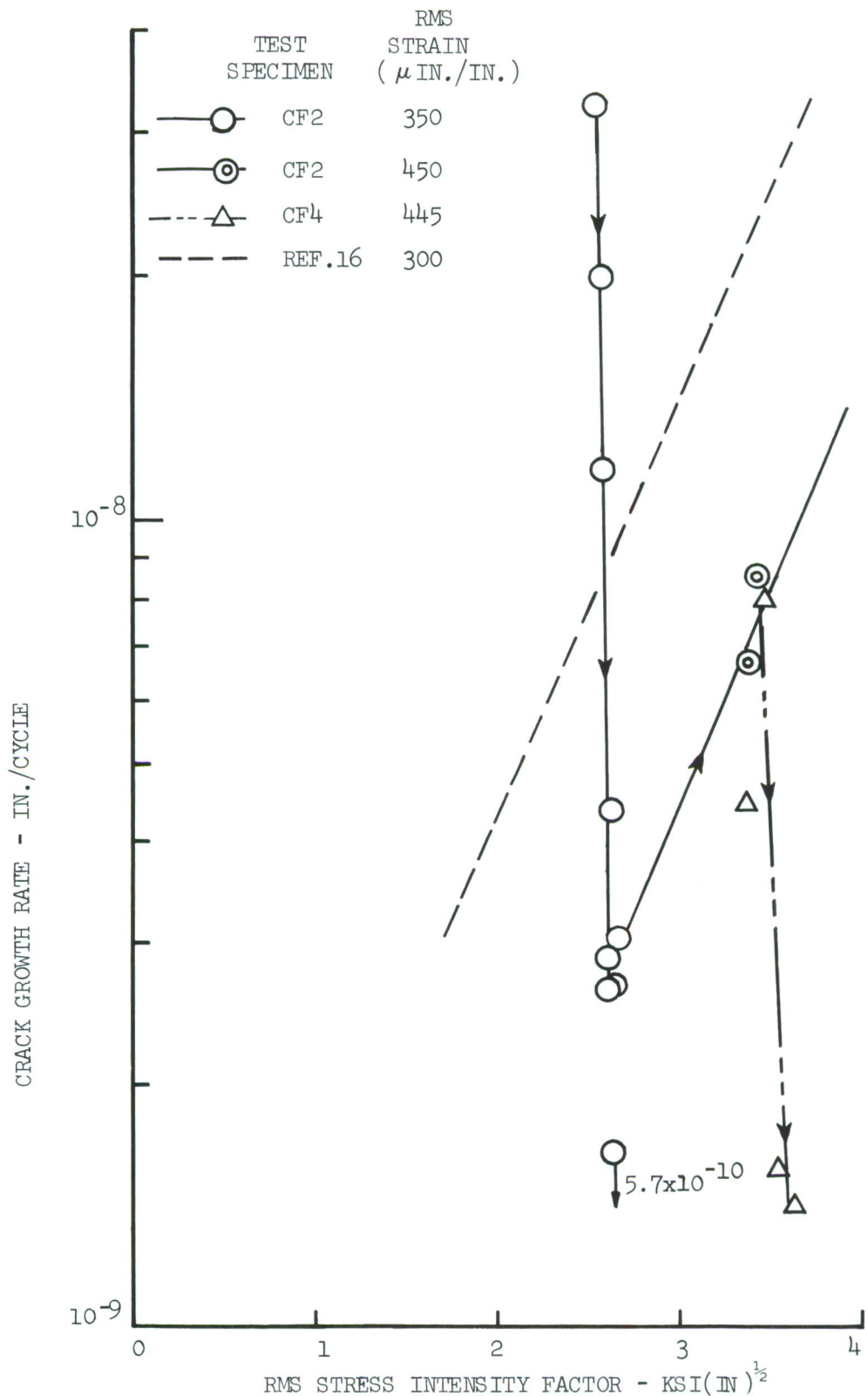


FIGURE 70. MEASURED CRACK GROWTH RATE, SIMULATED ACOUSTIC EXCITATION

relative to the lateral centerline of approximately four degrees (Figure 45). On assuming a plane stress state and a tension and compression Young's modulus of  $10.3 \times 10^6$  and  $10.5 \times 10^6$  psi, respectively, for the 7075-T6 material, a test specimen cross sectional area of 1.433 square inches is obtained from the cycling strain, tension load and compression load data. The cross sectional area from the panel geometry is 1.468 square inches.

Despite the adverse location of strain gages F4, just above the precrack, and F5, adjacent to the panel end doubler, in comparison to strain gage F3, only a small scatter in the data from the three strain gages is observed, as illustrated in Figure 44 at zero crack growth length. This result indicates that an even strain distribution has been achieved across the test panel. With the exception of the strain measurements from strain gage F4, which falls off with crack growth, the strain measurements (strain gages F3 and F5) remain fairly constant up to a crack length of approximately two inches.

The crack growth data shows good agreement with the corresponding data from Reference 35, represented by the solid curve in Figure 46. This curve is defined by equation 44(a) using the following values for the constants for the 7075-T6 sheet material

$$C_w = 3.44 \times 10^9$$

$$m = 0.227$$

$$n = 3.2$$

$$R = -0.85$$

The crack length used in the calculation extends from the edge of the fastener hole to the crack tip. A correction factor corresponding to the distance between the fastener hole edge and the countersunk fastener head edge is added to the experimental crack length which is measured from the countersunk fastener head edge.

**3.6.2 Flight-by-Flight and Combined Loads** - The response of the test specimens under combined simulated acoustic, inplane and flight loads is discussed first.

**3.6.2.1 Response of the Test Specimens** - The variation in the peak tension and compression stresses for all the test specimens except for CF9 is quite small indicating that good consistency has been obtained in the fabrication and installation of the test specimens. The high stress in panel CF9 is attributed to some inadequately tightened fasteners joining the frame web to the fingers on the end grip attachments, resulting in elongated frame web fastener holes. The elongated frame web fastener holes caused the test specimen face sheet to be subjected to a greater portion of the in-plane load, thereby increasing the panel stress by approximately 45 percent. A nonlinear hysteritic type load/strain curve is obtained during the cycling.

The free decay response from panels mounted only in the 220,000-pound force MTS fatigue machine provided useful panel frequency and damping data. The free decay data from the 160,000-pound force MTS fatigue machine exhibited a beating effect which prevented accurate analysis. The free decay data obtained under compression load indicates a nonlinear panel response.

The panel fundamental frequency declined by as much as 6 Hz during the free decay of the panel response. The panel frequencies, under compression load given in Figure 48, represent averaged frequencies over typically 0.3 seconds of the decay record, and therefore, overestimate the small amplitude panel frequency by a small amount. No nonlinear effects are observed when the panel is under a tension load.

The zero inplane load panel frequencies are similar to that measured on the calibration panel, and confirm that the empirical frequency correction factor  $K$  is approximately 1.33. A comparison of the measured and theoretically predicted variation ( $K = 1.35$ ) in the edge stiffened panel fundamental frequency indicates that a reasonable estimate of the panel fundamental frequency can be obtained using equation 14 with the correct frequency correction factor.

The relatively low panel damping coefficient of 0.0063, for zero and tension inplane loads (Figure 49), in comparison to the damping coefficient of 0.0095, measured for the calibration panel in the progressive wave tunnel, may be due to differences in acoustic radiation effects between the two test set-ups. Similar trends were obtained in damping tests on honeycomb panels in Reference 39, where considerable reductions in panel damping was obtained by the removal of large baffles (simulating large cross section acoustic progressive wave tunnels) from around the test panels. The small change in the panel damping coefficient will not, however, affect the shaker excited panel response in view of the simulation used.

The use of strain gage F1 rms level for establishing the shaker force levels for subsequent simulated acoustic, inplane load, and flight-by-flight load tests is selected to ensure a consistent rms strain level around  $350 \mu\text{in/in}$  for all the test specimens at zero inplane loads. This procedure is further justified by the small scatter between the panel edge gages A1 and A4 on the calibration test panel. The resulting panel rms force level is, on the average, higher than that measured on the calibration panel. The three force gages failed during the testing from unknown causes. Free decay and shaker excited strain peaks indicated force levels well within the capability of the force gage.

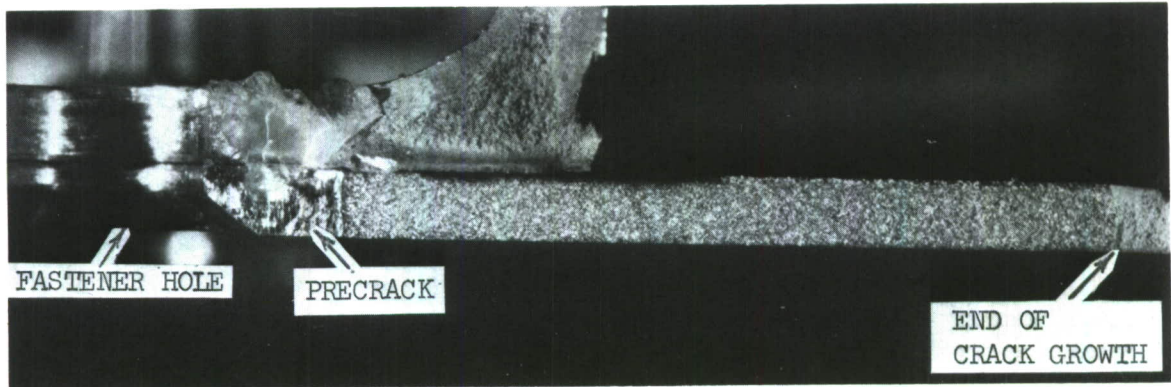
The variation in the panel rms strain with inplane load, as illustrated in Figure 50, is similar to that predicted by linear theory for acoustic excitation. Equation 19 is used together with the averaged frequency data (Figure 48) and the damping data (Figure 49), to which an increment of 0.0032 has been added to represent the panel damping in the progressive wave tunnel, to predict the variation in panel rms stress with inplane load as illustrated in Figure 50. The predicted variation is normalized at an rms strain of 350

$\mu$  in/in at zero inplane load. It is observed from Figure 50 that during the application of the shaker simulated acoustic and the ground and flight spectral loads, the panel edge rms strain from the shaker excitation varies approximately between 240 and 380  $\mu$  in/in and between 200 and 380  $\mu$  in/in for the upper and lower wing surface spectral loads, respectively.

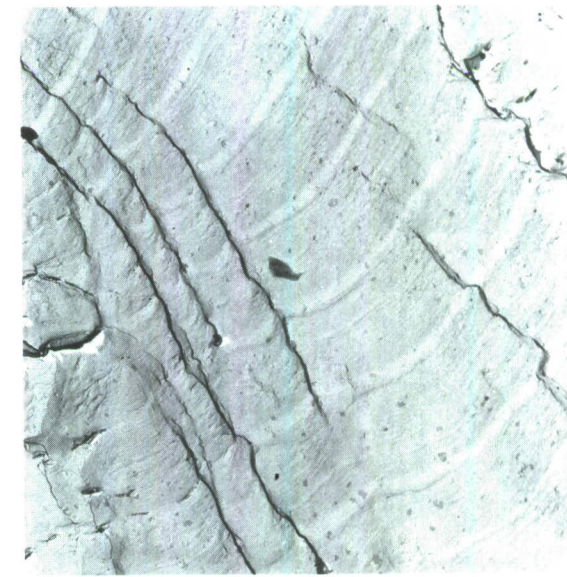
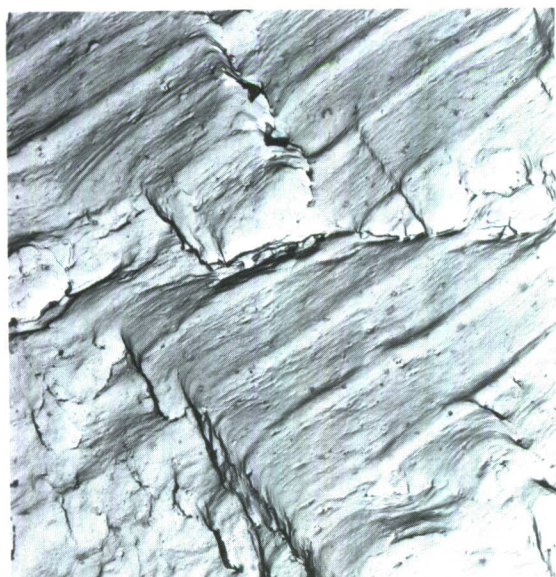
The typical axial strain history (strain gage F3) under combined acoustic and flight loading indicates that the panel edge axial strain is not affected by acoustic loading as predicted by equation 15. Comparison of the lateral strain history (strain gage F1) without and with the simulated acoustic loading in Figures 51 and 52, respectively, indicates the effect of the acoustic loading on the lateral panel edge strain. A similar comparison can be made from the corresponding narrow band strain response spectra illustrated in Figures 54 through 56. Although nearly 25,000 samples are used in the analysis, the samples represent only three flights and thus provide only a limited representation of the flight loads. The strain data from panels CF5 and CF6 are used in the spectral analysis to avoid changes in the mean strain level present in the response of the remaining test panels.

3.6.2.2 . Upper Wing Surface Flight Load Produced Crack Details - The crack propagation path for panel CF7, which is subjected only to flight loads is very straight as illustrated in Figure 57. An inplane tension load was applied to the panel to open the crack for the photograph. The crack face is normal to the panel surface. No fatigue markings are visible on the photograph of the crack face (Figure 71) with a 5 times magnification. Examination of the crack surface by means of an electron microscope with a magnification of 6500 times reveals distinct markings corresponding to the mean load changes between each flight as illustrated in the fractographs in Figure 71. The fractographs are taken from two locations halfway between the precrack tip and the frame edge. The crack growth rate of approximately  $80 \times 10^{-6}$  inches per flight, measured from the fractographs, corresponds well with the crack growth rate of  $100 \times 10^{-6}$  inches per flight obtained from Figure 64 at a crack length of 0.25 inches.

The surface crack propagation path for test panel CF9-2, which is subjected to simultaneous flight and simulated acoustic loading during the take-off segment of each flight, is straight but inclined slightly downward similar to the initial crack growth path on panel CF3. Examination of the crack surface revealed that the crack branched on the panel surface below the stiffener. The crack branching location is visible in the magnified photograph of the crack surface in Figure 72. The branching crack extends down to almost the half thickness of the face sheet. The fractographs of the crack surface indicate similar markings to those observed on panel CF7. The crack which developed on the opposite panel side to the precrack at the panel center drive rod bolt hole was stop drilled at a length of one inch and twice after that but continued to grow. It did not reach the strain gage rosette by the end of the test. In view of the relatively constant strain distribution up to a crack length of 2 inches, measured on panel CF3 (Figure 44), the panel center crack most likely did not influence the crack propagation from the precrack.



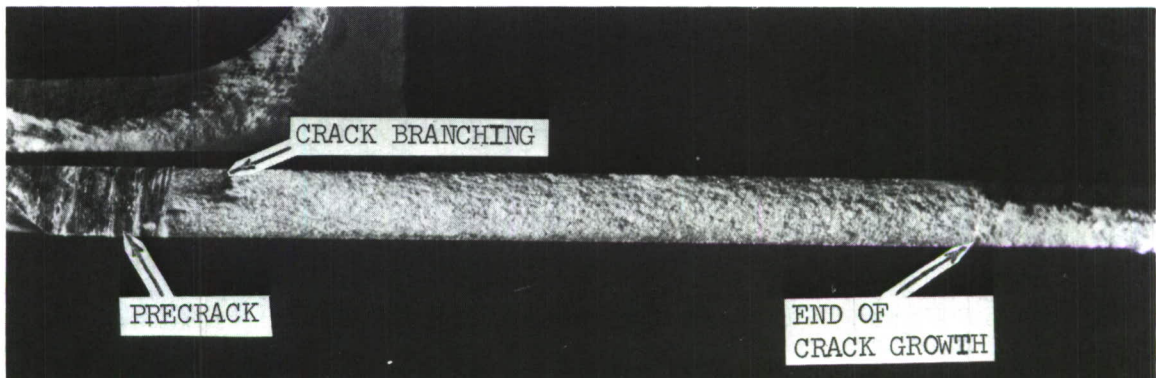
CRACK SURFACE MAGNIFIED 5X



$1\mu$

TYPICAL FRACTOGRAPHS OF CRACK SURFACE MAGNIFIED 6500X

FIGURE 71. CRACK SURFACE AND FRACTOGRAPHIC DETAIL, TEST SPECIMEN CF7



CRACK SURFACE MAGNIFIED 5X



[  
1 $\mu$

TYPICAL FRACTOGRAPHS OF CRACK SURFACE MAGNIFIED 6500X

FIGURE 72. CRACK SURFACE AND FRACTOGRAPHIC DETAIL, TEST SPECIMEN CF9-2

Two cracks initiated from the corners of the precrack in panel CF11. One of these cracks continued to propagate at a large angle to the panel lateral centerline until branching occurred (Figure 58) after which a straight crack propagation, with a small incline, developed. This test panel was subjected to simultaneous acoustic and flight loading encompassing both the flight and ground segments in each flight. A second crack (Figure 62), similar to the one in panel CF 9-2, developed from the panel center shaker drive rod bolt hole. This crack, with a length of approximately 1.4 inches, most likely did not influence the precrack propagation for the reasons previously discussed. After the discovery of the second crack, the circular doublers were removed from the remaining test panels, the center hole was reamed and deburred, and the doublers were rebonded after cleaning the surfaces.

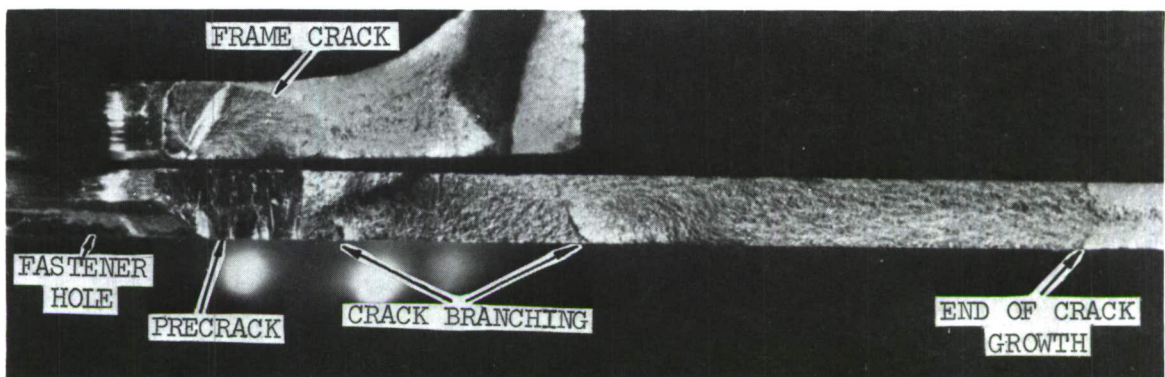
Test panel CF5 was subjected to the same simulated acoustic and spectral loads as panels CF9-2 and CF-11 except for the compression load, which was deleted. Double crack branching was obtained (Figure 60) before the crack assumed a reasonably straight but slightly inclined crack growth. The two crack branch locations are visible in the magnified crack face photograph in Figure 73. The markings on the fractographs are generally uniform over the surface and correspond to the high flight load spectral peaks.

Test panel CF9 encountered flight load induced stresses which are approximately 45 percent greater than the flight load stresses in the test panels previously discussed and, therefore, are at a comparable level with the lower wing surface flight load induced stresses. A straight but slightly inclined crack growth path was obtained. The crack face is only slightly inclined to the normal to the panel surface.

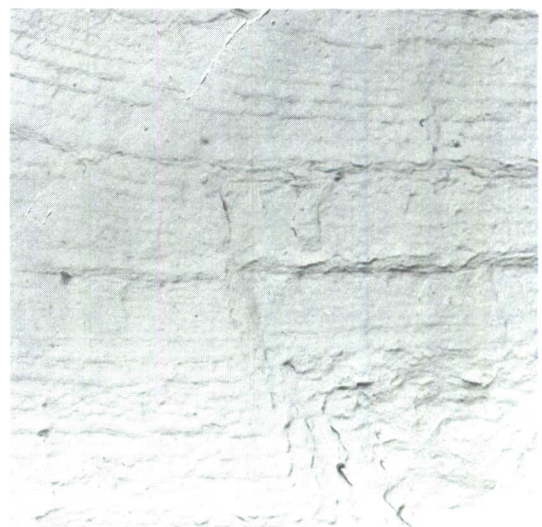
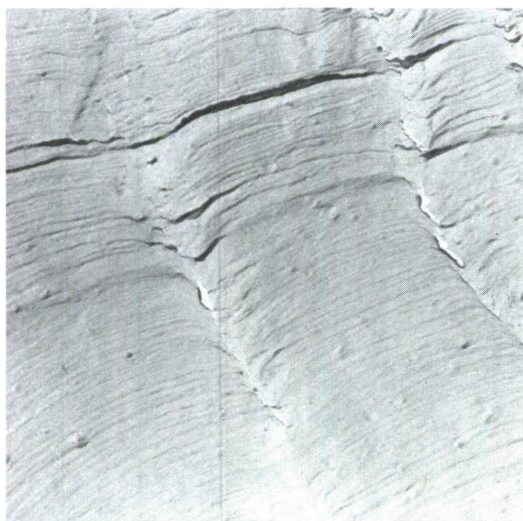
3.6.2.3 Lower Wing Surface Flight Load Produced Crack Details - The crack propagation path for panel CF8 without simulated acoustic loading is similar to panel CF12 (Figure 59) which is subjected to simulated acoustic loading for both the flight and ground segment in each flight. The crack face in both panels is initially normal to the panel surface but rotated to an angle of 45 degrees near the frame edge. The point of rotation is indicated in Figure 59 by the change in crack growth direction. It is also visible in the magnified photograph of the crack face in Figure 74. The fractographs in Figure 74 also show crack growth marks. The markings which differentiate the individual flights are difficult to identify due to the high crack growth rate associated with the panel.

The crack path for panel CF10 is a shallow curve associated with the initiation of the crack face rotation to a 45 degree angle relative to the panel surface directly from the precrack. The crack direction is essentially normal to the rivet line.

The crack path for panel CF6, illustrated in Figure 61, is essentially straight with a slight incline in the same direction as all the test panels including panel CF3. The crack face is normal to the panel surface.



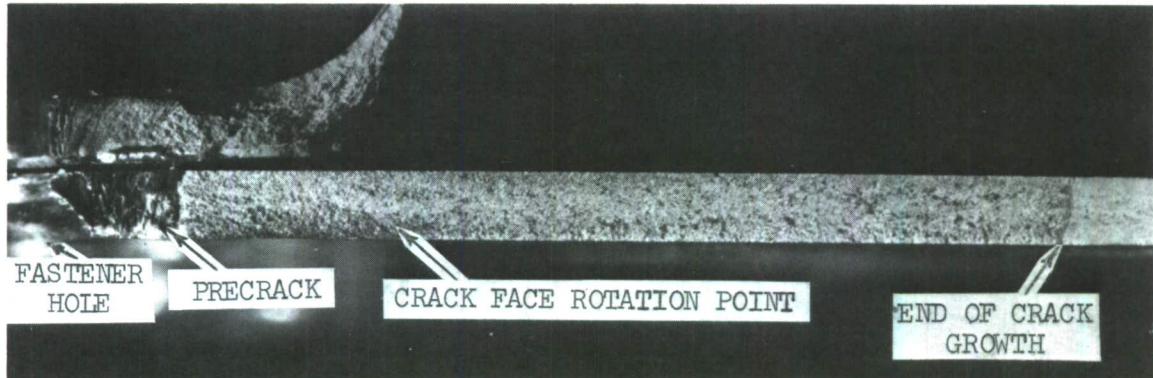
CRACK SURFACE MAGNIFIED 5X



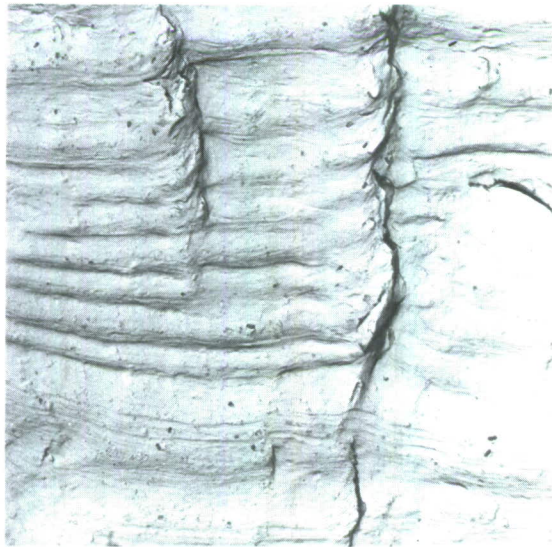
$1\mu$

TYPICAL FRACTOGRAPHS OF CRACK SURFACE MAGNIFIED 6500X

FIGURE 73. CRACK SURFACE AND FRACTOGRAPHIC DETAIL, TEST SPECIMEN CF5



CRACK SURFACE MAGNIFIED 5X



$1\mu$

TYPICAL FRACTOGRAPHS OF CRACK SURFACE MAGNIFIED 6500X

FIGURE 74. CRACK SURFACE AND FRACTOGRAPHIC DETAIL, TEST SPECIMEN CFL2

3.6.2.4 Measured Crack Propagation Rates - The crack propagation rate data is calculated from measured crack propagation data at typically every third measured data point to smooth the crack growth curves and is presented as a function of the crack length from the fastener hole. A least squares curve fit is used to establish a curve through the calculated crack growth rate data points.

The crack growth rate data for the upper wing surface test panels CF7, CF9-2 and CF11, combined in Figure 64, indicate a slight increase in crack growth rate for panels CF9-2 and CF11, which were subjected to simultaneous flight and simulated acoustic loading. The increase in crack growth rate, however, is very small and within the expected data scatter band. Consequently, no significant effect on the crack growth rate can be attributed to the combined acoustic and flight loads. The crack growth rate data from panel CF5 (Figure 63), without the compression load cycle, is also comparable to the above panels up to a crack length of 0.6 inches, after which the crack growth rate increases at a slower rate.

The crack growth rate for the upper wing surface flight loads for test panels CF8, CF10 and CF12 together with test panel CF9 are summarized in Figure 66. Two distinct crack propagation rates are obtained. The two test panels CF8 and CF12, in which the crack rotated to a 45 degree angle on passing the frame edge are comparable and exhibit an accelerated crack growth rate relative to the cracks in panels CF9 and CF10. The crack growth rates for test panels CF9, CF10 and CF6, Figure 65, are also comparable. The crack growth data indicates that the combined simulated acoustic and flight loads have no effect on the crack growth in these test panels.

3.6.2.5 Crack Branching - Crack branching is present only in the panels which are subjected to the combined acoustic and upper wing surface flight loads. No crack branching is observed on panel CF7 which is subjected only to the upper wing surface flight loads. Consequently, it is deduced that the crack branching is caused by the acoustic loading in combination with the flight loading. Additional supporting evidence is obtained by considering the variation of the stress field, produced by the combined loading, through the thickness of the panel. The acoustic loading produces a stress field at the panel edge, in the region of the precrack, which is a maximum at the surfaces of the panel (either tension or compression) and zero near the half thickness of the panel. Thus, the combined acoustic and flight loads produce a biaxial stress field at the surface of the panel (equations 29 and 30) and a uniaxial stress field at the half thickness of the panel. Any acoustic load effects on the crack growth are, therefore, expected to decrease progressively through the thickness of the panel and stop near the panel half thickness. The crack branching penetration depth in Figures 72 and 73 appears to corroborate the above reasoning. Crack branching also produces a greater scatter in the crack growth data as evident in Figure 63.

No crack branching is observed on the panels subjected to the combined acoustic and the much greater (see Tables 11 and 12) lower wing surface tension flight loads. Consequently, the ratio of the tension flight stress levels

to the acoustic stress levels is a significant parameter in determining the onset of crack branching.

3.6.2.6 Frame Fretting Crack Details - Fretting initiated fatigue cracks in the panel frames are drawn in Figure 67, magnified approximately five times. These fretting cracks were all initiated at the fastener hole in the frame adjacent to the precrack root. A typical fretting initiated crack is visible in the magnified crack face photograph in Figure 73. No frame crack initiation and crack growth data could be obtained since the crack occurred in an inaccessible location.

3.6.3 Simulated Acoustic Loads - The frequency and damping coefficient measured on test specimen CF2 at zero inplane loads are of comparable level to those measured on the other test specimens. The resonant frequency of 61.5 Hz at an indicated zero inplane load measured on panel CF4 is, however, too low. The behavior of the test specimen CF4 under compression load, both during the free decay and the shaker excitation tests, indicated the presence of panel buckling.

Examination of the test specimen CF4 free decay response at supposedly zero inplane load, after the completion of the test program, revealed the presence of a nonlinear panel response, associated with compression load, indicating that incorrect load readings were obtained from the load cell circuit. The frequency of 61.5 Hz and a damping coefficient of 0.007 are consistent with a compression load of approximately 10,000 pounds based on the test data in Figures 48 and 49.

The crack growth data from test specimen CF2, at a panel edge rms strain level of  $350 \mu \text{ in/in}$  from only the shaker simulated acoustic loading (Figure 70), indicated a rapid fall off in the crack growth rate until the crack appeared almost to have stopped growing after a total of  $6 \times 10^6$  random load cycles. This period of crack growth is associated with the change in the crack front from the vertical precrack to a bending type crack involving high surface crack growth and low growth at panel half thickness. Increasing the panel edge rms strain level to  $450 \mu \text{ in/in}$  produced the desired increase in crack growth rate. The test was stopped after a total of  $7.7 \times 10^6$  random load cycles when a vertical crack was discovered at the edge of the panel center circular doubler. The resulting crack growth rate in terms of the panel edge stress intensity factor (equation 66) is a factor of three less than that obtained from a panel edge crack along a fixed panel edge (Reference 16).

The slow crack growth relative to that reported in Reference 16 is more surprising as the L71 alloy used in that study is comparable to 2024-T4 alloy, which has a slower crack growth rate than the 7075-T6 material. The fatigue life of the shaker attachment was estimated at  $2 \times 10^7$  cycles at a stress level of 4500 psi based on the random SN data in Reference 19. The unexpected slow crack growth rate enabled the load cycles to approach the design life of the shaker attachment.

The crack front in test specimen CF4, at an indicated compression load level of 9000 pounds and a rms strain level of  $445 \mu \text{ in/in}$ , did not complete the transition to a bending crack front (Figure 70) when a vertical crack developed from one lateral edge of the round panel center doublers after a total of  $0.7 \times 10^6$  load cycles. The crack grew to a length of 2.9 inches in the last half hour of testing, causing the panel to buckle.

## VI. CORRELATION AND EVALUATION

### 1. Introduction

The complex problem of theoretically predicting the stiffened panel response to shaker simulated acoustic excitation and simultaneously applied axial inplane loads resulted in the use of a semi-empirical method, based on empirical data from stiffened panels, in the design of the test specimens. The accuracy of the semi-empirical method is evaluated against test data.

In addition, this section covers the most significant objective of comparing the existing crack growth analysis methods with the measured crack growth data. Flight-by-flight load crack growth analysis, as described in Section IV 2.4, has been performed on all panels subjected to flight loads and combined loads, both without crack retardation and using the Willenborg crack retardation model. The crack growth due to simulated acoustic loading is evaluated on the basis of available test data for other aluminum alloys because of the lack of baseline crack growth data at comparable loading frequency for the 7075-T6 material.

### 2. Panel Response

As indicated in the discussion of the test results in the previous section, equation 14 provides a reasonable estimate of the variation of panel fundamental frequency with inplane load (Figure 48) when using the correct value for the panel edge frequency parameter,  $K$ . The relatively low value of 1.33 for the frequency parameter, as opposed to the more typical value for stiffened airplane type panels of 1.48, indicates an increased panel edge flexibility probably associated with frame web bending.

The electromagnetic shaker simulation used in this program did not reproduce the variation of panel resonant frequency with inplane load that would have occurred with acoustic excitation. This variation in the panel frequency, apart from any modal curvature changes which would affect the stress distribution in the panel, is responsible together with the panel damping, for the variation in the panel rms stress with inplane load. In spite of this limitation, good correlation in the shape of the measured panel edge rms stress variation with inplane load, when compared with the theoretically predicted variation (Figure 50), has been obtained. Thus, the most critical parameter affecting crack propagation, namely the stress level, has been adequately simulated over the range of inplane load used in this program.

The correlation between the measured panel edge stress and the predicted panel edge stress, using equations 27 and the skin-stringer design nomograph in Reference 19, due to acoustic loading, is complicated by the presence of at least four peaks in the panel response (Figure 34) around

69 Hz. On assuming a single mode response normally obtained, equation 27 in conjunction with the design nomographs over-estimate the rms panel edge stress by 41 percent for a damping coefficient of 0.0095. This difference of 41 percent is within the accuracy of current sonic fatigue analysis methods.

The correlation curve between the shaker force and the acoustic spectrum level in Figure 33 is obtained on the basis of equal panel edge rms strain. The mean square panel edge stress due to the shaker force and also the acoustic force are given theoretically by equation 25 when the generalized force term,  $GF_M$ , is replaced by the corresponding shaker and acoustic generalized force terms given by equations 37 and 35, respectively, and the corresponding frequencies and damping coefficients are used. Since a 2 Hz bandwidth shaker excitation is used, the expression for the mean square panel edge stress (equation 25), due to shaker excitation, must be multiplied by a bandwidth correction factor obtained from Figure 4. These expressions for the mean square panel edge stress can be rearranged on the basis of equal mean square panel edge stress to produce the ratio of shaker force level to acoustic spectrum level for comparison with the calibration curve in Figure 33. With shaker power on and power off damping coefficients of 0.4 and 0.0095, respectively, the above procedure over-estimates the ratio of the electromagnetic shaker force level to the acoustic spectrum level by approximately 37 percent.

The degree of correlation is reasonable in view of the uncertainty as to the actual value of the damping coefficient measured with the shaker power switched on.

### 3. Crack Growth Prediction

The expression for the stress intensity factor, given by equation 63, is used together with the baseline crack growth data to obtain the crack growth rate in terms of the effective stress intensity factor. Good correlation has been obtained between the baseline crack growth rate data and comparable published data (Reference 35), as illustrated in Figure 46.

For the flight-by-flight loads and the combined loads, the results of the crack growth analysis procedure discussed in Section IV 2.4 are presented graphically in terms of the total number of flights and the total crack length. The results of the analyses are illustrated in Figures 75 and 76 for the upper wing surface loads and in Figures 77 and 78 for the lower wing surface loads together with the corresponding crack growth data.

The agreement between the measured and predicted crack growth without retardation for test specimen CF5, subjected to simulated acoustic loads, and the upper wing surface spectral loads, without the compression loads, is reasonable since crack retardation effects are generally not significant for this type spectral loading. In general, good agreement between the measured and predicted crack growth has been obtained for the test specimens CF5, CF7, CF9-2 and CF11 which are subjected to the upper wing surface

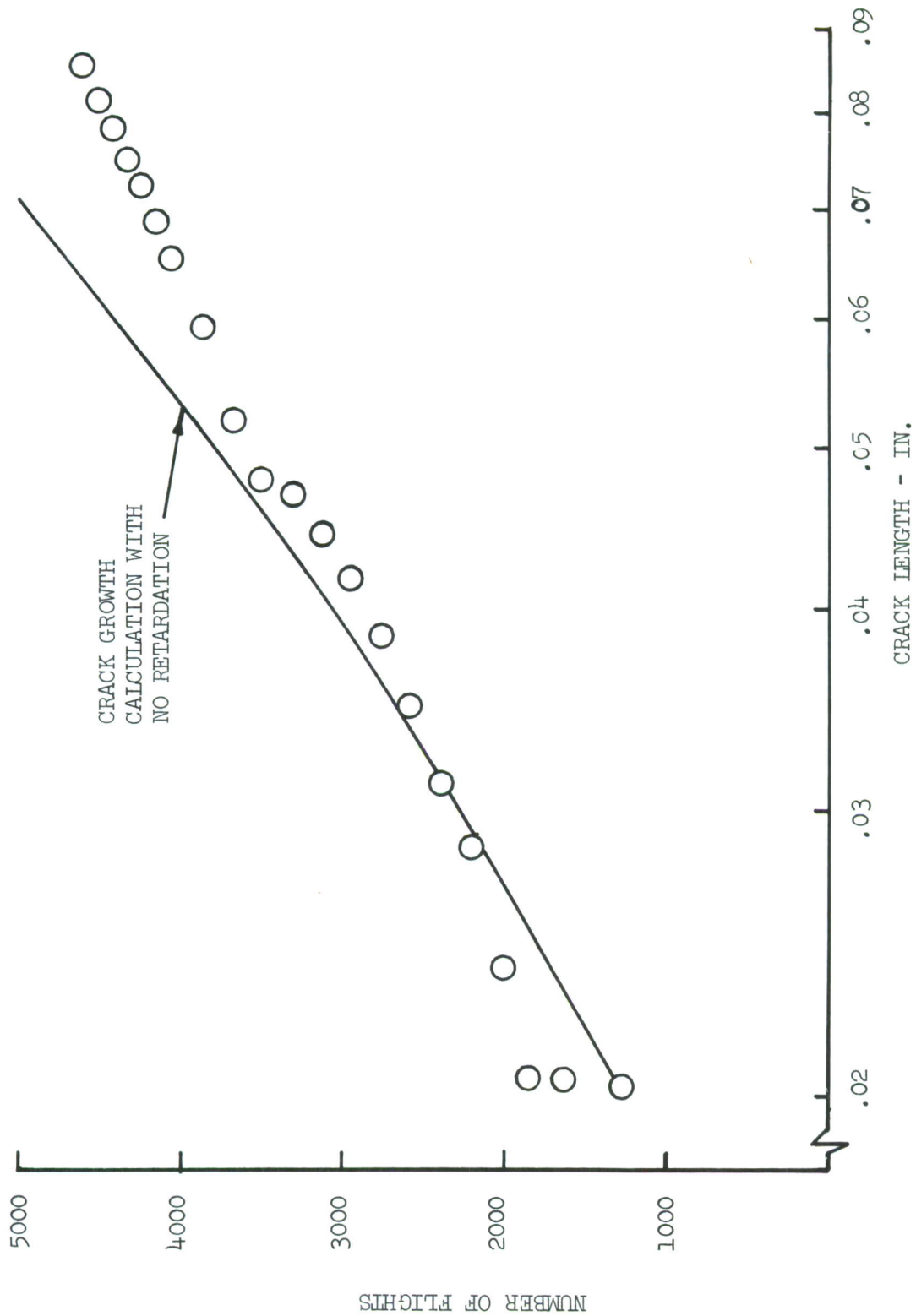


FIGURE 75. COMPARISON OF MEASURED AND CALCULATED CRACK GROWTH, TEST SPECIMEN CF5

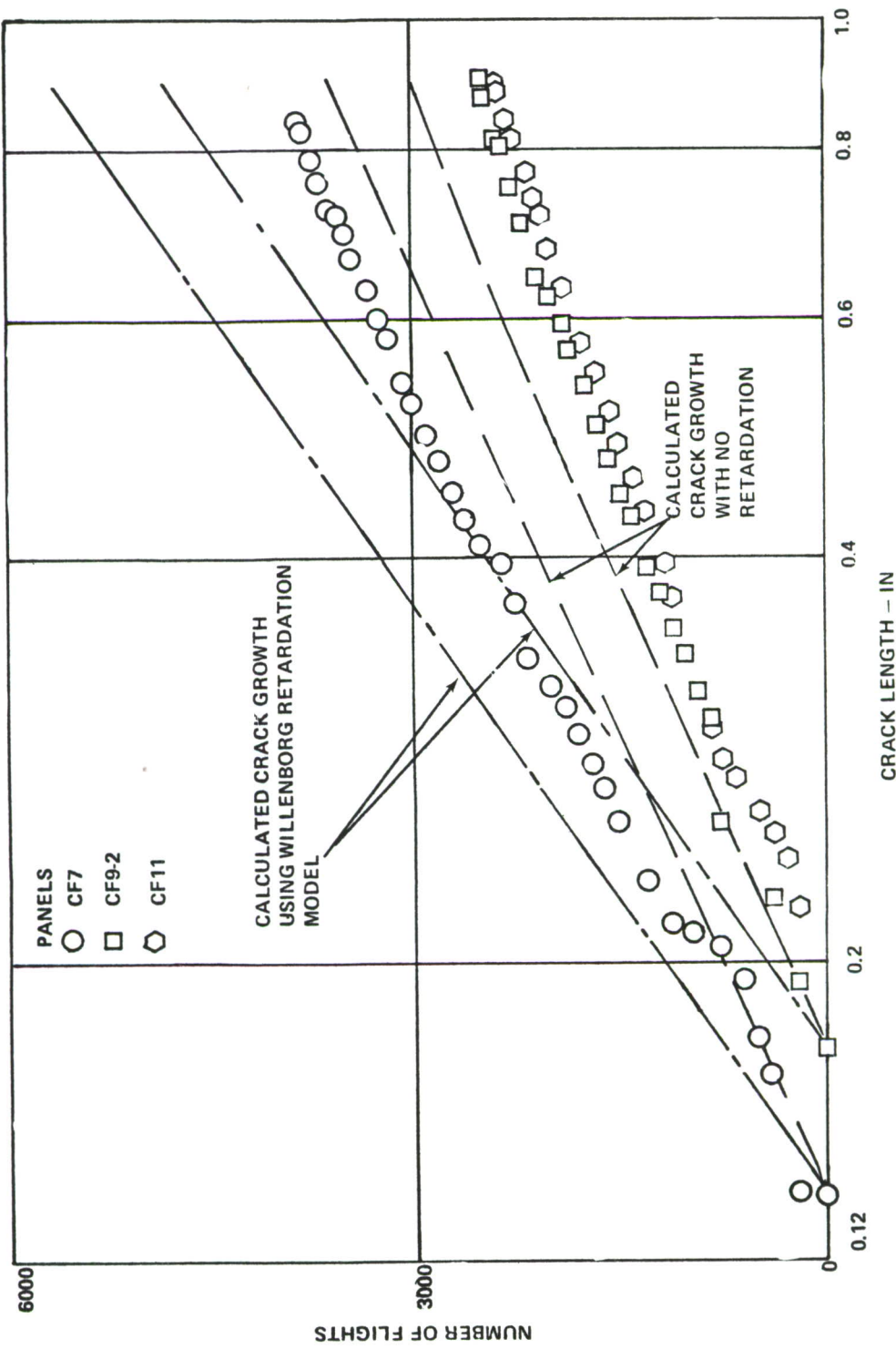


FIGURE 76. COMPARISON OF MEASURED AND CALCULATED CRACK GROWTH, UPPER WING SURFACE LOADS

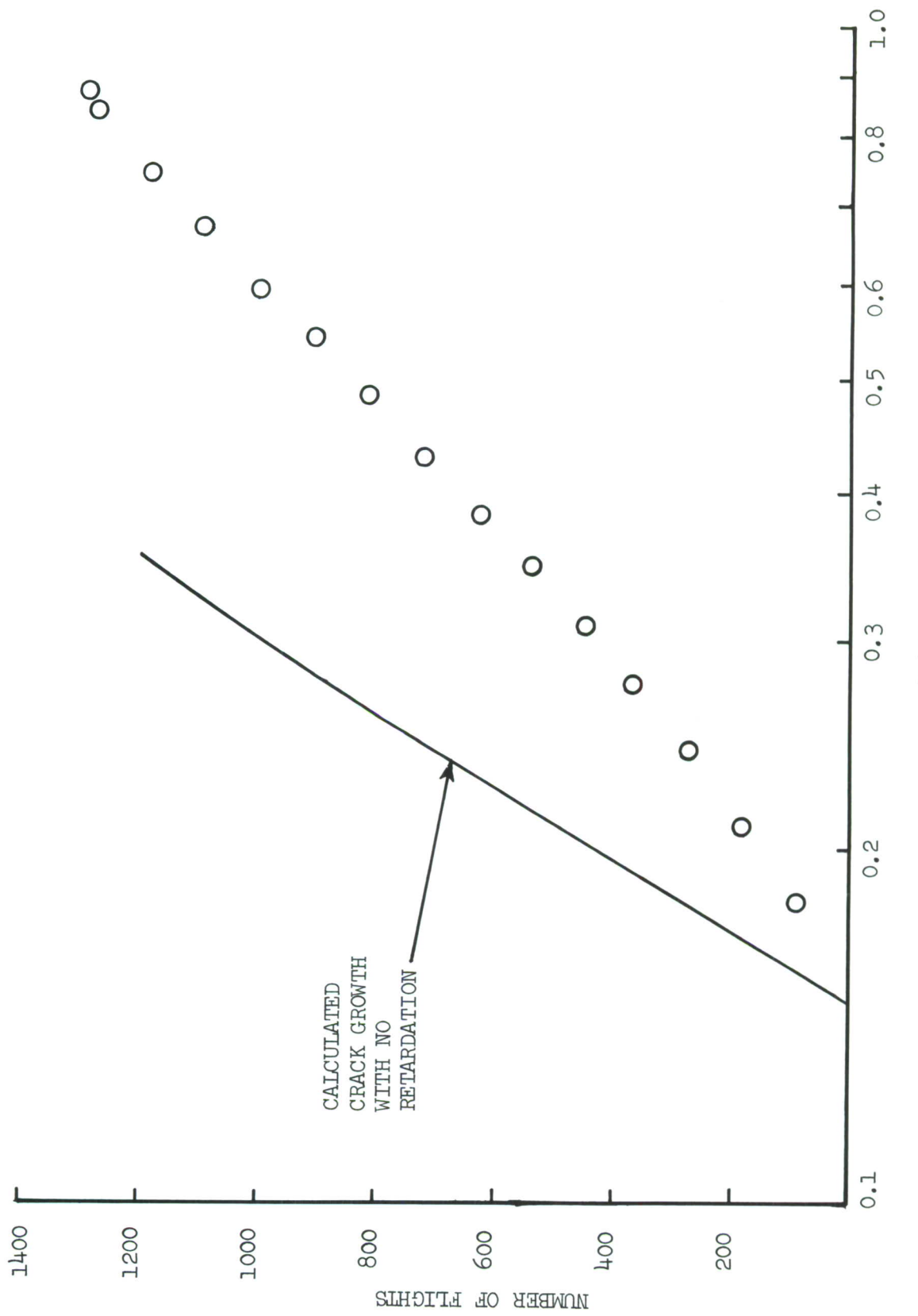


FIGURE 77. COMPARISON OF MEASURED AND CALCULATED CRACK GROWTH, TEST SPECIMEN CF6

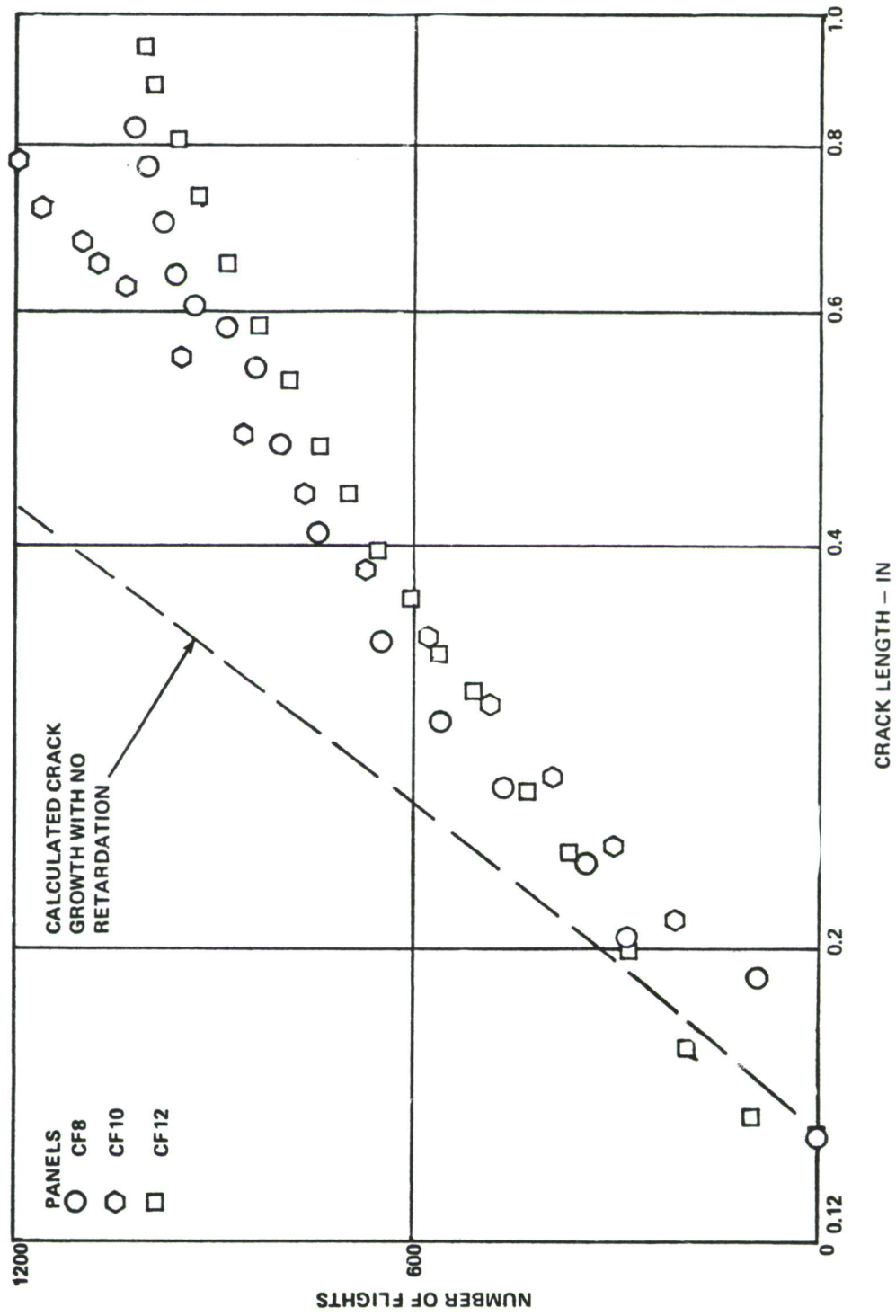


FIGURE 78. COMPARISON OF MEASURED AND CALCULATED CRACK GROWTH, LOWER WING SURFACE LOADS

flight-by-flight loads. The measured crack growth data for test specimen CF7, which is subjected only to flight loads, falls between the crack growth predicted by the Willenborg retardation model and the crack growth predicted without crack retardation. For test panels CF5, CF9-2 and CF11, which are subjected to the combined acoustic and upper wing surface loads, good agreement between the measured and predicted crack growth without crack retardation is obtained. Only the axial flight load induced stresses are included in these calculations. The generally good agreement between the measured and predicted crack growth data for all the test specimens subjected to the upper wing surface flight loads, indicates that no significant effects on crack growth can be attributed to the combined acoustic and flight loads. The crack branching, however, is attributed to the simulated acoustic loading on comparing the straight crack in test specimen CF7 (Figures 57 and 71) with the cracks in test specimens CF5, CF9-2, and CF11 (Figures 58, 60, 72 and 73). Crack branching also occurred in test specimens subjected only to acoustic loading, as discussed in Reference 16.

The crack growth in all the test specimens subjected to the lower wing surface loading exceeded the calculated crack growth without retardation, as illustrated in Figure 77 for test specimen CF6 and in Figure 78 for test specimens CF8, CF10 and CF12. Crack surface rotation to 45 degrees relative to the panel surface is characteristic for these test specimens, except for CF6, associated with the relatively high flight-by-flight loads as summarized in Table 11. The accelerated crack growth and the rotation of the crack face are directly associated with the high panel stresses (See Table 11) produced by the high lower wing surface flight loads. The rotation of the crack face indicates a change over from a plane stress/plane strain condition to a plane stress condition through the thickness of the panel ahead of the crack tip (Reference 40). Also, no crack branching was observed leading to the conclusion that the relative magnitude of the acoustic load stress to the tension flight load stress is a significant parameter in crack branching.

The limited crack growth data from the simulated acoustic loading did indicate a considerably lower than expected crack growth rate as discussed in Section V 3.6.3 and illustrated in Figure 70. The reduced crack growth could indicate that the expression for the Mode I stress intensity factor (equation 66), for a crack along a fixed boundary, may not be applicable to riveted panels where the peak bending moment occurs alternately at the rivet line and the frame edge in each stress cycle.

## VII. CONCLUSIONS

- A. The electromagnetic shaker arrangement used in this program provides in general, a good simulation of the acoustic loading for the fundamental mode of a stiffened panel.
- B. The test specimen design objectives with regard to critical panel buckling stress, uniform stress distribution across the panel, plane stress state and small variability between test specimens have been accomplished.
- C. Good agreement between the measured baseline constant amplitude crack growth data and comparable published data for the same load conditions has been obtained.
- D. The axially applied flight loads produced a plane stress field in the test specimen which is parallel to the panel edge and normal to the rivet hole precrack. The acoustic loading produced a reverse bending type stress distribution in the panel edge in the vicinity of the pre-crack, with the peak surface stress path normal to the panel edge and the flight load stress field.
- E. For the structural model, crack orientation and combination of acoustic and flight loads used in this program, the measured crack growth data did not indicate any significant effects on crack growth by the inclusion of the acoustic loading. In other structures in which the peak acoustic load stress is acting in the same direction as the flight load induced stress and the precrack is oriented normal to both stress paths, significant effects on crack growth may occur.
- F. Surface crack branching is, however, caused by acoustic loading and is a function of the relative acoustic and flight tension load induced stress levels.
- G. The measured crack growth rate data on panels subjected to the upper wing surface flight loads are in good agreement with the predicted crack growth rate.
- H. The higher level lower wing surface loads produce crack face rotation relative to the panel surface associated with a plane stress condition ahead of the crack tip. The measured crack growth rate exceeded the predicted crack growth rate without retardation.
- I. The limited acoustic crack growth data, from the acoustic fatigue type rivet hole precrack parallel to the panel edge, indicated a lower than expected crack growth rate. Further evaluation is prevented by the lack of random acoustic crack growth data for U.S. airplane alloys and for riveted airplane structures, in general.

## REFERENCES

1. "Airplane Damage Tolerance Design Requirements", MIL-A-83444 (USAF), Military Specification, United States Air Force, May 1974.
2. Paris, P., and Erdogan, F., "A Critical Analysis of Crack Propagation Laws", Transactions of the ASME. J. of Basic Engineering, Dec. 1963, pp. 528-534.
3. Schijve, J., "The Prediction of Fatigue Crack Propagation Under Service Load-Time Histories", National Aerospace Laboratory (NLR), the Netherlands, Report No. NLR-MP-73016U, May 1973.
4. Wood, H.A., and Haglage, T.L., "Crack Propagation Test Results for Variable Amplitude Spectrum Loading in Surface Flawed D6ac Steel", Air Force Flight Dynamics Laboratory, AFFDL-TM-FBR-71-2, February 1971.
5. Elber, W., "Fatigue Crack Propagation Under Random Loading: An Analysis Considering Crack Closure", Presented at the Eleventh Conference of the I.C.A.F., May 1969.
6. Brussat, T.R., "An Approach to Predicting the Growth of Failure of Fatigue Cracks Subjected to Arbitrary Uniaxial Cyclic Loading", Damage Tolerance in Aircraft Structures, ASTM STP 486, 1971, pp 122-143.
7. Wheeler, O.E., "Spectrum Loading and Crack Growth", Transactions of the ASME J. of Basic Engineering, Vol. 94, Series D, No. 1, March 1972, p. 181.
8. Willenborg, J.D., Engle, R.M., Jr., and Wood, H.A., "A Crack Growth Retardation Model Using an Effective Stress Concept", AFFDL-TM-FBR-71-1, Air Force Flight Dynamics Laboratory, Jan. 1971.
9. Gallagher, J.P., "A Generalized Development of Yield Zone Models", AFFDL-TM-FBR-74-28, Air Force Flight Dynamics Laboratory, Jan. 1974.
10. Hall, L.R., Shah, R.C., and Engstrum, W.L., "Fracture and Fatigue Crack Growth Behavior of Surface Flaws and Flaws Originating at Fastener Holes; Vol. I - Results & Discussions", AFFDL-TR-74-47, Vol. 1, May 1974.
11. Brussat, T.R., Chiu, S.T., "Flaw Growth in Complex Structures; Third Interim Report", Contract F33615-75-C-3093, Lockheed Report LR 27431, Dec. 1975.
12. Clarkson, B.L., "The Propagation of Fatigue Cracks in Tensioned Plate Subjected to Acoustic Loads," Acoustical Fatigue in Aerospace Structures, Syracuse University Press, 1965.

REFERENCES (Cont'd)

13. Jost, G.S., "Fatigue Crack Growth Under Random Combined Stress Conditions", Ph.D. Thesis, University of Southampton, 1969.
14. Mills, D., "Acoustically Propagated Cracks in Biaxially Tensioned Plates", Ph.D. Thesis, University of Southampton, 1970.
15. Kirkby, W.T., "Some Predictions of Crack Propagation Under Combined Cabin Pressurization and Acoustic Loading", R.A.E. Report CP 1286.
16. Byrnes, K.P., "Fatigue Crack Propagation at the Boundaries of Acoustically Excited Panels", Ph.D. Thesis, University of Southampton, October 1973.
17. Belcher, P.M., Eshleman, A.L., and Von Dyke, J.D., "Development of Aircraft Structures to Withstand Acoustic Loads", Aero/Space Engineering, Vol. 18, No. 6, 1969.
18. Clarkson, B.L., "Stresses in Skin Panels Subjected to Random Acoustic Loading", ISVR Report, 1967.
19. Ballentine, J.R., et al, "Refinement of Sonic Fatigue Design Criteria", AFFDL-TR-67-156, January 1968.
20. Timoshenko, S., and Woinowsky-Krieger, S., "Theory of Plates and Shells", McGraw-Hill.
21. Leissa, A.W., "Vibration of Plates", NASA SP-160, 1969.
22. "NASA Tech Note 3781", 1957.
23. Bayerdorfer, G., "Experimental Investigation to Establish Acoustic Fatigue Design Charts", J. Sound Vib. 17 (1), 1971.
24. Sandow, F., and Maurer, O., "Random Vibration Fatigue Tests of Weld-bonded and Bonded Joints", Shock and Vib. Bulletin, 1975.
25. Powell, A., "On the Fatigue Failure Structures Due to Vibrations Excited by Random Pressure Fields", J.A.S. 30(2), 1958.
26. Crandall, S.H., "Random Vibration", Technology Press, 1958.
27. Rudder, F.F., and Plumlee, H.E., "Sonic Fatigue Design Guide for Military Aircraft", AFFDL-TR-74-112, 1975.
28. Pulgrano, L.J., and Ablowitz, M.A., "The Response of Mechanical Systems to a Band of Random Excitation", Shock and Vib. Bul. 39(3), 1969.

REFERENCES (Cont'd)

29. Adkisson, R.E., et al, "Analytical Investigation of Medium STOL Transport Structural Concepts, Vol. 1 Study Results", AFFDL-TR-74-109, Air Force Flight Dynamics Laboratory, August 1974.
30. Thrall, E.W., Private Communications, Cl-253-PABST-26, Douglas Aircraft Co., 30 July, 1975.
31. Pelloux, R.M., "Review of Theories and Laws of Fatigue Crack Growth Propagation," Proceedings of the Air Force Conference on Fatigue and Fracture of Aircraft Structures and Materials, AFFDL-TR-70-144, Air Force Flight Dynamics Laboratory, 1969.
32. Erdogan, F., "Crack Propagation Theories," Volume 2 of "Fracture" edited by Liebowitz, H., Academic Press., New York, 1968.
33. Gray, T.D., "Fatigue Crack Retardation Following a Single Overload", AFFDL-TM-73-137-FBR, Air Force Flight Dynamics Laboratory, October 1973.
34. Tada, T., et al, "The Stress Analysis of Cracks Handbook", Del Research Corporation, 1975.
35. Meyle, R.H., "A Critical Study of Several Crack Growth Equations which Model the Effect of Load Ratio, "AFFDL-TM-FBR-73-154, Air Force Flight Dynamics Laboratory, October 1973.
36. Brussat, T.R., "Rapid Calculation of Fatigue Crack Growth by Integration", Fracture Toughness and Slow Stable Cracking", pp. 298, ASTM STB59, August 1974.
37. Roberts, R. and Erdogan, F., "The Effect of Mean Stress on Fatigue Crack Propagation in Plates Under Extension and Bending", Journal of Basic Engineering, Trans. ASME, Vol. 89, 1967.
38. Elber, W., "The Significance of Fatigue Crack Closure", ASTM Conference, Toronto, Canada, June 1970.
39. Soovere, J., "Dynamic Properties of Graphite Fiber Honeycomb Panels", AIAA Dynamics Specialists Conference, Williamsburg, March 19-20, 1973.
40. Broek, D. and Vlieger, H., "The Thickness Effect in Plane Stress Fracture Toughness" NLR TR 74032U, October 1973.